

National Technical University of Athens
SCHOOL OF CHEMICAL ENGINEERING



Naoum Vaenas
Physicist

**Development of One-Dimensional
Titania Nanomaterials**

Thesis submitted for the degree of Doctor of Philosophy

ATHENS 2014

National Technical University of Athens

School of Chemical Engineering

Department I – Chemical Sciences

Advisory Committee

E. Pavlatou Associate Professor NTUA (Supervisor)

K. J. Haralampous Associate Professor NTUA

P. Falaras Researcher A' NSCR Demokritos

Examination Committee

E. Pavlatou Associate Professor NTUA (Supervisor)

K. J. Haralampous Professor NTUA

P. Falaras Researcher A' NSCR Demokritos

I. Mora Seró Associate Professor Jaume I

A. Moutsatsou Professor NTUA

A. Karantonis Lecturer NTUA

Y. Raptis Associate Professor NTUA

This work was realized in the Laboratory of "Photo-redox Conversion and Storage of Solar Energy", at the Department of Physical Chemistry, of the Institute for Advanced Materials, Physicochemical Processes, Nanotechnology & Microsystems, National Center for Scientific Research "Demokritos", under the supervision of Dr. P. Falaras (Research Director).

.....
Approval of the thesis from the School of Chemical Engineering NTUA
does not imply acceptance of the opinions of the author (Law
5343/1932, Article 202)

Abstract

The scope of this thesis is the development of one-dimensional titania (TiO_2) nanostructures (nanotubes NTs) and in parallel their application-evaluation in Dye Sensitized Solar Cells (DSCs). The motivation for this study was to understand the basic mechanism of the TNTs growth and the influence of the materials properties on the operation and behavior of the DSCs and through them to contribute to literature of photovoltaics. Nanotubular structures have been established in the literature as an advanced nanostructure. They belong to the same family of 1D materials (together with nanowires and nanorods), due to their lengthwise growth. Titania nanotubes (TNTs) are ideal candidates for the objectives of the research in the field of solar energy conversion to electricity as: a) can be easily prepared by anodic oxidation on a titanium foil (flexible and conductive substrate), b) their morphology can be controlled through electrochemical engineering at the nanoscale, c) they present unique electronic properties, including vectorial electron transport.

In the first part of this thesis, some preliminary experiments were realized in order to improve the morphology of the titanium (Ti) substrate and the nanotubular TiO_2 films. Specifically, the TNTs were prepared under mild oxidation conditions in NH_4F /ethylene glycol electrolytes. The effects of polishing the Ti foils (before anodization) and the removal of the nanograss (structural disorder created on the NTs top surface due to their prolonged exposure to a F^- rich environment) on the nanotubular films properties were investigated. After optimization of the anodization conditions, homogeneous anodic films consisting of smooth and long NTs were obtained and incorporated as photoelectrodes in high efficient dye-sensitized solar cells (backside illuminated).

In the second part of the thesis, the structural properties of the self-assembled TNTs are examined, in order to provide pathways for

uninhibited electron transport. The effect of annealing post-treatment on their structural properties was systematically explored with respect to their electrical characteristics and photoelectrochemical performance in DSCs. A variety of parameters was controlled and optimized including the annealing temperature, the heating rate and duration of the thermal treatment. The obtained results confirmed the existence of a correlation between the crystalline/structural properties of the TiO₂ nanotubes and their electrical characteristics, thus revealing the close interplay of crystal size, grain boundaries and crystallite interconnectivity with the electron dynamics (transport/recombination) governing the DSC operation and efficiency.

In the third section, advanced tubular nano-architectures were constructed by complex anodization modes. Slow and rapid potentiostatic anodization processes were accordingly compared to the galvanostatic one, while a two step potentiostatic - galvanostatic technique was applied for the first time for the growth of TiO₂ NT arrays, as a step forward in relation to the existing potentiostatic – potentiostatic (P-P) technique. The novel approach of galvanostatic tube growth on a potentiostatically patterned Ti foil provided the most uniform TiO₂ nanotubular films with clean top surface exempt of nanograss or cracks over extended areas. Evaluation of the TiO₂ NTs performance as photoelectrodes in DSC devices showed distinct differences of their electrical parameters that reflected finely the underlying structure/morphology variations of the different anodic oxidation conditions.

The last part of this thesis exclusively coped with the enhancement of the DSCs' power conversion efficiency, through the use of new state of the art redox couples and organic dyes. The cobalt redox shuttle was employed in combination with titania nanotube arrays as a highly porous photoelectrode to facilitate electrolyte diffusion and a surface-blocking triphenylamine-based dye (D35) au lieu of standard ruthenium complex such as the Z907 dye. Therefore, exploiting the actual potential of the cobalt-based redox couple an

open-circuit potential higher than 0.8 V was attained using the D35 dye (while Z907-based solar cells delivered V_{oc} values of about 0.6 V).

For this work advanced morphological and structural characterization of the TNTs was performed using Atomic Force Microscopy (AFM), Scanning Electron Microscopy (SEM), Transmission Electron Microscopy (TEM), Ultraviolet-Visible (UV-Vis) and Raman spectroscopy. DSCs were developed and investigated with the use of the TNTs as photo-anodes. The in-situ evaluation of the DSCs was implemented taking advantage of state of the art methods such as Electrochemical Impedance Spectroscopy (EIS), Intensity Modulated Photovoltage/ Photocurrent Spectroscopy (IMVS/IMPS) and J-V characteristics.

Acknowledgments

First, I would like to thank the NCSR “Demokritos” for the attribution of a four years fellowship that permitted me to work in an excellent environment for the cultivation of knowledge and innovation. During my PhD thesis, Demokritos was my second home.

I express my deepest gratitude to Dr. P. Falaras for his undivided supervision, support and encouragement throughout my study. I appreciate the opportunity that he has given me to join his group and not only to enter to the scientific community, but also to develop my personality.

Sincerely thanks to my academic supervisor Prof. E. Pavlatou for her assistance, kindness, and critical analysis of my work during this degree. I also want to express my deep acknowledgment to Prof. A. Haralambous, member of my advisory committee and to Profs. I. Mora Seró, A. Moutsatsou, A. Karantonis, Y. Raptis that accepted to participate in the jury of my thesis.

My sincere gratefulness belongs to Drs. A. Kontos, V. Likodimos and T. Stergiopoulos, they are teachers and friends for me.

I have been fortunate to work with many great collaborators over the course of this thesis, Dr. N. Boukos, Dr. F. Katsaros, Dr. G. Vougioukalakis, Dr. M. Konstantakou, Dr. S. Spanou, Dr. G. Konti, D. Tsoukleris, M. Bidikoudi, N. Moustakas, D. Perganti, M. Arfanis, E. Darviri, E. Latifi, K. Gkini, H. Georgiou I am extremely thankful to all.

Finally, I acknowledge partial financial support from the SANS project (FP7-NMP-2009 SMALL-3) and NANOMESO “Thalis” project (Mis: 377064).

List of Publications

Journal Publications

1. N. Vaenas, T. Stergiopoulos, A.G. Kontos, V. Likodimos, P. Falaras, “Influence of controlled-charge anodization processes on the morphology of TiO₂ nanotubes and their efficiency in dye-sensitized solar cells”, *Electrochimica Acta* 113 (2013) 490–496.
2. N. Vaenas, M. Bidikoudi, T. Stergiopoulos, V. Likodimos, A. G. Kontos, P. Falaras “Annealing effects on self-assembled TiO₂ nanotubes and their behaviour as photoelectrodes in dye-sensitized solar cells”, *Chemical Engineering Journal*, 224 (2013) 121-127.
3. S. Spanou, A.I. Kontos, A. Siokou, A.G. Kontos, N. Vaenas, P. Falaras, E.A. Pavlatou “Self cleaning behaviour of Ni/nano-TiO₂ metal matrix composites” *Electrochimica Acta* 105 (2013) 324–332.
4. N. Vaenas, T. Stergiopoulos, A.G. Kontos, V. Likodimos, N. Boukos, P. Falaras, “Sensitizer activated solar cells based on self-organized TiO₂ nanotubes”, *Microelectronic Engineering* 90 (2012) 62–65.
5. A.G. Kontos, M. Pelaez, V. Likodimos, N. Vaenas, D.D. Dionysiou, P. Falaras, “Visible light induced wetting of nanostructured N–F co-doped titania films”, *Photochemical & Photobiological Sciences* 10 (2011) 350-354.
6. N. Vaenas, T. Stergiopoulos, A.G. Kontos, V. Likodimos, E. Pavlatou, P. Falaras, “TiO₂ nanotubes-based dye solar cells employing a Co²⁺/Co³⁺ electrolyte: understanding charge recombination and interfacial energetic”, to be submitted to JPC.
7. M. Konstantakou, K. Gkini, N. Vaenas, T. Stergiopoulos, P. Falaras “Optimization of anodic titania nanotubes for dye solar cells using Cobalt (ii)/(iii) electrolytes”, to be submitted.

Conference Presentations

1. P. Falaras, A. G. Kontos, T. Stergiopoulos, N. Vaenas, D. Perganti, A. Speliotis “Development of flexible dye sensitized solar cells using TiO₂ nanotube active photoelectrodes and platinized ITO-PET cathodes” International Congress on Materials and Renewable Energy, MRE 2013, 1-3 July 2013, Athens, Greece.
2. M. Konstantakou, K. Gkini, N. Vaenas, T. Stergiopoulos, P. Falaras, “Optimization of Anodic Titania Nanotubes for Dye Solar Cells Using Cobalt (II)/(III) Electrolytes”, 4th International Conference from Nanoparticles and Nanomaterials to Nanodevices and Nanosystems (IC4N) June 16-20, 2013 Corfu Island, Greece.
3. M. Konstantakou, N. Vaenas, N. Moustakas, V. Likodimos, A. G. Kontos, T. Stergiopoulos, A. Tserepi, P. Falaras “Tailoring the surface properties of TiO₂ films with plasma treatment for efficient Dye-Sensitized Solar Cells based on the Co(II)/Co(III) redox shuttle”, European Materials Research Society E-MRS 2013 Spring Meeting, May 27-31, 2013 Strasbourg, France.
4. N. Vaenas, K. Gini, T. Stergiopoulos, E. Pavlatou, K. J. Haralampous, A. G. Kontos, P. Falaras “Electrochemical development and application of titania nanotubes in the Dye Solar Cell” 9th National Conference Chemical Engineering 23 - 25 May 2013 Athens Greece.
5. N. Vaenas, M. Bidikoudi, T. Stergiopoulos, V. Likodimos, A. G. Kontos, P. Falaras, “Dye-sensitized solar cells combining anodic titania nanotubes, D35 organic chromophore and Co²⁺/ Co³⁺ redox couple”, XI International Conference on Nanostructured Materials, August 26 – 31 2012, Rhodes, Greece.
6. A.G. Kontos, N. Vaenas, T. Stergiopoulos, V. Likodimos, P. Falaras, “Self-assembled TiO₂ nanotubes: important parameters affecting their morphology and performance in dye-sensitized solar cells”, 7th

European Meeting on Solar Chemistry and Photocatalysis: Environmental Applications - SPEA7, June 17-20 2012, Oporto, Portugal.

7. N. Vaenas, T. Stergiopoulos, A.G. Kontos, V. Likodimos, P. Falaras, "Self-organized anodic TiO₂ nanotubes: structure optimization for efficient dye-sensitized solar cells", SANS Workshop Sensitizer activated nanostructured solar cells Les Diablerets (Switzerland) 12-15 March 2012.

8. N. Vaenas, A.G. Kontos, F. Katsaros, T. Stergiopoulos, V. Likodimos, D.D. Dionysiou, P. Falaras, "Synthesis, characterization and photocatalytic activity of hydrothermally grown nanotubular titanates" 2nd European Symposium on Photocatalysis JEP 2011 September 25-30 2011 Bordeaux Cite Mondiale France.

9. N. Vaenas, M. Bidikoudi, N. Stergiopoulos, T. Kontos, A. G. Likodimos, P. Falaras. "Self-ordered TiO₂ nanotubes growth in NH₄F/ethylene glycol electrolytes: parameters variation in anodic oxidation and application in dye-sensitized solar cells", 8th International Conference on Nanosciences & Nanotechnologies - NN11 12-15 July 2011, Thessaloniki, Greece.

10. N. Vaenas, T. Stergiopoulos, A. G. Kontos, V. Likodimos, P. Falaras, "TiO₂ nanotubes for dye sensitized solar cells", 3rd IC4N – 2011, 3rd International Conference from Nanoparticles & Nanomaterials to Nanodevices & Nanosystems and Cretan Workshop on: Global Challenges and Opportunities for Nanotechnology, June 26-30 2011, Crete, Greece.

11. N. Vaenas, A. G. Kontos, T. Stergiopoulos, V. Likomidos, N. Boukos, P. Falaras, "Self-assembled and vertically aligned anodized titania nanotubes employed in dye sensitized solar cells", Final Workshop of the FP7 REGPOT - Project DEMATEN, Processing of Nanostructured Ceramics and Nanocomposites, March 3-5, 2011, Brno, Czech Republic (Oral presentation by N. Vaenas).

12. N. Vaenas, T. Stergiopoulos, A. G. Kontos, V. Likodimos, N. Boukos, P. Falaras, “Electrochemical synthesis of self-aligned titania nanotubes: application in sensitizer activated solar cells”, 4th International Conference on Micro-Nanoelectronics, Nanotechnologies & MEMs (Micro & Nano 2010), NCSR Demokritos, 12–15 December 2010, Athens, Greece.

Table of Contents

Committees	i
Abstract	ii
Acknowledgments	v
List of Publications	vi
List of Figures	xiii
List of Tables	xviii
List of Abbreviations	xix
Chapter 1. Introduction	1
1.1. Global energy issues.....	1
1.2. General considerations about the photovoltaics	3
1.3. Objectives and motivations	6
1.4. References.....	7
Chapter 2. Literature Survey	8
2.1. Electrochemical synthesis of the TiO ₂ nanotubes	8
2.1.1. Titanium dioxide (TiO ₂)	8
2.1.2. Brief history on the electrochemical synthesis of the TiO ₂ nanotubes	9
2.1.3. Anodic oxidation of titanium	11
2.2. Dye solar cell (DSC)	18
2.2.1 Front side illuminated DSCs	18
2.2.2 Back side illuminated DSCs.....	23
2.3. Experimental part	27
2.4. References.....	29
Chapter 3. Sensitizer activated solar cells based on self-organized TiO₂ nanotubes	40
3.1. Introduction	40
3.2. Experimental.....	41
3.2.1 Pre-treatment of Ti foils	41
3.2.2. Anodization conditions and post-treatment for the anodic films	41
3.2.3. Cell assembly and measurements	42
3.3. Results and discussion.....	42
3.3.1 Pre-treatment effects.....	42

3.3.2 Anodization	43
3.3.3. Post-treatment effects	44
3.3.4. Incorporation into solar cells.....	46
3.4. Conclusions	47
3.5. References.....	48
Chapter 4. Annealing effects on self-assembled TiO₂ nanotubes and their behaviour as photoelectrodes in dye-sensitized solar cells.....	51
4.1. Introduction	51
4.2. Experimental.....	53
4.2.1. TNTs preparation	53
4.2.2. TNTs and DSCs characterization.....	53
4.3. Results.....	54
4.3.1. Morphology-structure of the as-grown TiO ₂ nanotubes.....	54
4.3.2. Structural properties	56
4.3.3. Performance-characterization of dye-sensitized solar cells using TiO ₂ NT photoelectrodes	59
4.4. Conclusions	68
4.5. References.....	69
Chapter 5. Influence of controlled-charge anodization processes on the morphology of TiO₂ nanotubes and their efficiency in dye-sensitized solar cells.....	74
5.1. Introduction	75
5.2. Experimental.....	76
5.2.1. TiO ₂ nanotubes preparation	76
5.2.2. Surface modification and cell assembly	77
5.2.3. Characterization	78
5.3. Results and Discussion	78
5.3.1. TiO ₂ NT characteristics	78
5.3.2. DSC's performance	89
5.4. Conclusion	94
5.5. References.....	95
Chapter 6. TiO₂ nanotubes-based dye solar cells employing a Co²⁺/Co³⁺ electrolyte: understanding charge recombination and interfacial energetics	103
6.1. Introduction	104
6.2. Experimental.....	107

6.2.1. Materials	107
6.2.2. TiO ₂ nanotubes development	107
6.2.3. Solar cell assembly	108
6.2.4. Instrumentation.....	108
6.3. Results and Discussion	109
6.3.1. Morphology-structure and sensitization of the TiO ₂ nanotubes	109
6.3.2. J-V characterization of NT-based DSCs under 1 sun AM1.5G illumination	113
6.3.3. Photovoltaic performance of NT-based DSCs under different levels of light illumination.....	116
6.3.4. Non-linear recombination in NT-based DSCs	119
6.3.5. Electrical features of the solar cells	123
6.4. Conclusions	129
6.5. References.....	130
Chapter 7. Conclusions.....	139
7.1. Evaluation and contribution.....	139
7.2. Perspectives for future work	140
7.3. References.....	141
Appendix. Electrochemical nano-engineering.....	143
Morphology manipulation.....	143
References.....	151

List of Figures

Figure 1-1. World energy consumption data [1]. Organization for Economic Co-operation and Development (OECD) i.e. developed countries, non-OECD i.e. emerging markets. 1 quadrillion Btu = 2.93×10^{11} KWh.	2
Figure 1-2. Solar radiation spectrum [2].	3
Figure 1-3. Road map for the best research cell efficiencies (NREL) [6].	4
Figure 1-4. Number of publications per year obtained from a literature search using the keywords “dye sensitized” and “solar cell” (ISI Web of Knowledge) [7].	5
Figure 2-1. Planar Ti_3O building-block representation (left) and TiO_6 octahedral (right) for the TiO_2 anatase phase (Ti-white, O-red) [3].	9
Figure 2-2. Representation of the vectorial electron transport at the nanotubes. ...	11
Figure 2-3. Electrochemical cell (left) and shaped TiO_2 nanotubes (right).	12
Figure 2-5. The potentiostatic anodization’s evolution in three stages and the corresponding current-time (j-t) graph.	14
Figure 2-6. Mechanistic model for the nanotubes development (a), flow mechanism for the upwards oxide’s expansion (b) [47].	16
Figure 2-7. Photos of an anodize Ti foil (circular part) (a), detached TNT film (membrane) (b).	16
Figure 2-8. SEM (scanning electron microscopy) images of the TiO_2 nanotubes. Top surface of NTs (a)-(c), cross section of the NTs (d)-(f), bottom of the NTs (g),(h), patterned Ti foil after the detach of TiO_2 nanotubular film-membrane (i).	17
Figure 2-9. Schematic overview of the DSC multilayer structure. [54].	19
Figure 2.10. Principle of operation and energy level scheme of the dye-sensitized nanocrystalline solar cell [61].	20
Figure 2-11. Kinetics of a Ru-based sensitized TiO_2 solar cell with I^-/I_3^- redox mediator. Typical time constants for the forward reactions (green arrow) and the loss-recombination reactions (red arrow) [65].	21
Figure 2-12. Characteristic I-V curve of a PV and the corresponding electrical parameters.	22
Figure 2.13. Scheme of a flexible back illuminated DSC, based on TiO_2 nanotubes (a) and the corresponding functional cell with total thickness lower than 1 mm (b).	24
Figure 2-14. Electron transport in a nanoparticulate (a) and a nanotubular (d) TiO_2 layer. Images of a nanoparticulate front side illuminated photoelectrode (b) and the corresponding sealed DSC (c). Accordingly the nanotubular photoelectrode (e) and the back illuminated DSC.	25
Figure 2-15. Image of the electrochemical setup for Ti anodization.	28
Figure 2-16. Equipment (solar simulators, potentiostats, etc) for the characterization of the Dye Solar Cells.	29
Figure 3-1. SEM and AFM images of Ti foils before (a, c) and after polishing (b, d), respectively.	43

Figure 3-2. SEM top images of the grassy surface of the NTs (a) along with cross section images of the tubes after anodization of polished samples (b). Note that similar images were obtained for the unpolished samples.44

Figure 3-3. SEM top images of NTs after removal of nanograss (a) and under higher magnification (b). Top images of the lower part of the tubes, revealing the greater NT diameter present at the bottom of the NTs (c) and the presence of the barrier layer (d).45

Figure 3-4. Current-voltage (I-V) characteristics of the DSCs based on NTs electrodes (cell 1-3), obtained under 1 sun (AM 1.5G) illumination; Cell 1 is constructed with raw NTs, cell 2 contains anodic films prepared on a polished substrate and cell 3 refers to a DSC with NTs grown on a polished foil and after removal of “nanograss”.47

Figure 4-1. (a) clean top surface area (nanotubes with wall thickness of 15 nm), (b) cross section of the nanotubular film with thickness of about 15 μm and in the inset a magnified area of the oriented nanotubes array, (c) the bottom of the nanotubes and in the inset, an area where the caps of the tubes have got off revealing that the wall thickness at the bottom is three times greater (45 nm) than at the top. (d) compact layer with 200 nm thickness, below the nanotubes after the annealing of the as anodized sample at 600 $^{\circ}\text{C}$56

Figure 4-2. (a) Raman spectra of TiO_2 nanotubes under different annealing treatment; inset: variation of the shift (ω) and full width at half maximum (FWHM) of the main anatase mode $E_{g(1)}$ as a function of the annealing temperature. (b) Crystal size (estimated by micro-Raman spectroscopy) variation under different annealing conditions (set 1: annealing temperature, set 2: heating rate at 400 $^{\circ}\text{C}$, set 3: annealing duration at 400 $^{\circ}\text{C}$).57

Figure 4-3. Raman spectrum with the Rutile traces which presented at the bottom of the NTs.59

Figure 4-4. Current density-voltage (J-V) characteristics obtained under 1 sun illumination (AM 1.5G) and dark of DSCs using photoelectrodes annealed under (a) different temperatures 400-600 $^{\circ}\text{C}$, SET 1, (b) using photoelectrodes annealed under heating rate 1-10 $^{\circ}\text{C}/\text{min}$, SET 2 and (c) using photoelectrodes annealed under different durations 1-6 h, SET 3.60

Figure 4-5. EIS spectra under 1 sun illumination (at V_{oc}) for the 3 different experimental SETs. (a) and (b) constant heating rate 5 $^{\circ}\text{C}/\text{min}$ and annealing duration at 1 h, varied target temperature from 400 to 600 $^{\circ}\text{C}$, set 1. (c) Constant annealing duration 1 h and target temperature 400 $^{\circ}\text{C}$, varied heating rate 1, 2, 5 and 10 $^{\circ}\text{C}/\text{min}$, set 2. (d) Constant heating rate 5 $^{\circ}\text{C}/\text{min}$ and target temperature 400 $^{\circ}\text{C}$, varied annealing duration 1, 2, 3 and 6 h, set 3.62

Figure 4-6. Characteristic IMPS Nyquist plot for a DSC based on TiO_2 NTs annealed at 500 $^{\circ}\text{C}$ for 1 h with rate 5 $^{\circ}\text{C}/\text{min}$64

Figure 4-7. (left column) Variation of transport times τ_{trans} (derived from IMPS) and recombination times τ_{rec} (derived from EIS) and (right column) resistances of the Ti- TiO_2 and Pt-electrolyte interfaces R_{Pt+Co} (derived also from EIS), with the annealing conditions (3 different sets of thermal treatment were employed).65

Figure 5-1. Characteristic curves for the different anodization processes: P30, P60 and P-P samples (constant voltage at 30 and 60 V in raw and 60 V in pattern Ti foil). G and P-G samples (constant current at 3.15 mA cm^{-2} in raw and pattern Ti foil). .80

Figure 5-2. SEM images of the various TiO_2 NTs samples: the first column summarizes the characteristic top view SEM images of the different NTs films (P 30, P 60, G, P-G, P-P), the second column shows the high magnification images taken

from 'clear' areas and the third one the corresponding cross section SEM images. For the P-G film, a zoomed area of interest is added (inset).82

Figure 5-3. TEM images (I, II) of P30 sample before annealing (amorphous) and after thermal treatment when the material is transformed into polycrystalline (III, IV, V and VI). As shown in the (I) and (II) the amorphous NTs of the P 30 sample have a thick barrier layer of about 45 nm; additionally the voids, which exist between the tubes, are well defined. The (III-IV) shows the polycrystalline structure of the nanotubes, after annealing. More specifically, (III and V-dark field) points out a wide distribution of the crystallites size. In (IV) the lattice fringes of the TiO₂ nanocrystals allow the identification of lattice spacings of ~3.5 °Å, reflecting the d-spacing of (1 0 1) crystallographic plane in anatase, which corresponds to the most thermodynamically stable {101} facets. The existence of Debye-Scherrer rings in selected area electron diffraction pattern (SAED) further evidences the formation of anatase crystallites (VI).....84

Figure 5-4. Characteristic SEM images of the TiO₂ NT membrane derived from the first step of the P-G anodization including the cross section, the bottom of the membrane (barrier layer) and the resulting pattern on the Ti foil after peeling off. ..85

Figure 5-5. Raman spectra of P30, P60, G, P-G and P-P samples after annealing and N719 dye sensitization. TiO₂ modes are marked by stars in order to distinguish them from the N719 dye Raman (vibration) modes.88

Figure 5-6. Raman spectra of P30 sample as anodized (I), after annealing (II) and after sensitization (III).....90

Figure 5-7. UV-Vis absorption spectra (in Kubelka Munk units) of the P30 sample: as anodized (I), after annealing (II) and after sensitization (III).....91

Figure 5-8. J-V characteristic curves of back-illuminated (1 sun, AM1.5G) DSCs, using the prepared nanotubular samples as photoelectrodes.93

Figure 5-9. Electron lifetimes (τ) of the different DSCs plotted vs. the photovoltage (V), for various light intensities (1 - 0.1 Suns).....94

Figure 6-1. Molecular structures of the D35 and Z907 dyes as well as of the cobalt(II)/(III) tris(2,2'-bipyridine) complex, utilized in the present study.107

Figure 6-2. (a) Characteristic SEM images of the nanotubular film top surface. In the inset, a magnified top image and a cross section of the film are shown; (b) Graphical representation of the probable unrestricted electrolyte diffusion through the nanotubular film (left figure) and the problematic infiltration into the nanoparticulate film (right).111

Figure 6-3. The Raman investigation reveals the anatase form of the NT films after their crystallization and the rutile traces which exist at the interface between the substrate and the tubes' bottom.112

Figure 6-4. Absorbance spectra of the sensitized TNTs photoelectrodes with the Z907 (dash line) and the D35 (solid line) dyes. Absorption coefficients at maximum wavelength λ_{\max} of the dyes are also given.113

Figure 6-5. J-V characteristics of the various types of cells (a) under 1 sun illumination, (b) under dark.....114

Figure 6-6. J-V characteristics (a) under 1 sun and (b) dark, of the nanotubular D35/ I and Z907/ I DSCs.....116

Figure 6-7. Photocurrent as a function of the incident light power density, for the different DSCs. The dotted lines, representing the ideal linear behaviour, only serve as a guide to the eye.118

Figure 6-8. Photocurrent as a function of the incident power, for the D35/I and Z907/I cells, a perfect linearity was observed.119

Figure 6-9. Semi-log plot of photovoltage against the incident light power density, for the D35/Co and Z907/Co solar cells.121

Figure 6-10. Semi-log plot of photovoltage against the incident power density, for the D35/I and Z907/I solar cells.121

Figure 6-11. Plot of the dark current with the actual voltage drop at the photoelectrode (denoted as V_F) after the correction of the applied voltage for the series resistance. The I - V_F curves were fitted to the non-ideal diode equation, resulting in fitting parameter values of n and I_0123

Figure 6-12. (a) Capacitance at the TiO_2 /electrolyte interface plotted against the actual potential of the photoelectrode V_F (b) Recombination resistance (R_{rec}) plotted against the voltage at the equivalent band position V_{ecb} . Results refer to D35/Co and Z907/Co solar cells- see the text inside for details.126

Figure 6-13. Plot of R_{rec} against V_F (voltage drop in the photoelectrode); The R_{rec} - V_F curves were fitted (close to open-circuit) to a single exponential function

$(R_{\text{rec}} = R_0 \exp \left[\frac{bqV_F}{kT_0} \right])$, determining n and R_0 as fitting parameters.128

Figure 6-14. Electron lifetimes at different photovoltages (the plot was constructed by estimating lifetimes under different levels of illumination using IMVS spectroscopy).129

Figure A-1. NTs with different internal diameters (D_{in}) and wall thickness (W): $D_{\text{in}}=30$ nm, $W=10$ nm (a), $D_{\text{in}}=60$ nm, $W=25$ nm (b), $D_{\text{in}}=120$ nm, $W=50$ nm (c). ..144

Figure A-2. NTs with a variety of top surface morphologies: semi-clean and disoriented (a), clean, oriented and with separated walls (b), stuck and developed on predefined spots (c).145

Figure A-3. Complex surface morphologies that have been formed onto a patterned Ti foil. The concave parts have internal diameter from 100 to 160 nm and the internal pores can be varied from 15 to 50 nm. 1-3 pores inside the concave parts (a), 4-7 pores inside the concave parts (b), $7 >$ pores inside the concave part (2 μm length, the nanotubular film is transparent) (c).146

Figure A-4. Nanotubular films in a variety of lengths: total thickness 1200 nm (a), total thickness ~ 40 μm (b).147

Figure A-5. NTs with walls decorated by ribs: smooth walls without ribs (a), random ribs distribution (white lines) (b), controlled ribs distribution at distances of 100 nm (white lines) (c).148

Figure A-6. Double layer tubes, each layer has different morphological characteristics (a, b). Branched nanotubes, from the initial NT two new NTs can be formed (c, d).149

Figure A-7. Close bottom TiO_2 nanotubes, as detached from the titanium foil (with ultrasonic treatment) and forming supplementary morphologies.150

Figure A-8. Pure TiO₂ membranes up to (or >) 0.1 mm is possible to be developed: photograph of the membrane (a) and the corresponding SEM image (b).150

Figure A-9. Impressive colorful oxide coatings, that have been formed by anodization of titanium in sulfuric acid electrolytes (for 1 min): potential 10 V, thickness of the coating 25 nm, color gold (a); potential 20 V, thickness of the coating 50 nm, color turquoise blue (b); potential 30 V, thickness of the coating 100 nm, color raf-blue (c).151

List of Tables

Table 1-1. Recent state of the art efficiencies values for Dye Solar Cells [8].	5
Table 1-2. Recent state of the art efficiencies values for Perovskite Solar Cells [8].	6
Table 2-1. Correlation of the NTs' features with the anodization parameters.	13
Table 4-1. Electrical parameters derived from J-V curves on DSCs based on TiO ₂ nanotubes treated under different thermal conditions. It is noted that the samples marked with * (400 °C, 5 °C/min, 1 h) represent the same cell, but they have been added in the table for better comparison.	60
Table 4-2. Electrical parameters derived from the fitting of the EIS spectra using an equivalent circuit of the type: $R_s(R_{Pt+Co}C_1)(R_{rec}C_\mu)$ where constant phase elements (characterized by the parameters Y_0 and n) were routinely employed in the equivalent circuit instead of the use of simple capacitances (C_1 or C_μ) for more accurate fitting.	63
Table 4-3. Dye loading of the NTs per cm ² was investigated using UV-Vis spectroscopy by the desorption of the nanotubular samples in a 1/1 H ₂ O/ EtOH solution which contains 0.2 M NaOH.	66
Table 5-1. Morphological characteristics of the different TiO ₂ NTs obtained by analysis of the SEM images.	86
Table 5-2. Calculated morphological and structural characteristics of the TiO ₂ NTs together with experimental and theoretical anodization charge σ and anodization yield. ¹ Calculated from eq. 3a and b. ² Calculated from Raman peak at 142 cm ⁻¹ . ³ Calculated from eq. 4.	88
Table 5-3. Electrical parameters of the DSCs constructed with various anodized NT films.	93
Table 6-1. Electrical parameters of nanotubular photoelectrodes which are sensitized by D35, Z907 and N719 dyes, comprising cobalt-based and iodine-based electrolytes.	116
Table 6-2. Electrical parameters derived from J-V curves on DSCs, under different levels of light illumination.	118

List of Abbreviations

Ti	Titanium
TiO ₂	Titania or Titanium Dioxide
TNTs	Titania Nanotubes
1-D	One Dimensional
DSCs	Dye Sensitized Solar Cells
PVs	Photovoltaics
AFM	Atomic Force Microscopy
SEM	Scanning Electron Microscopy
TEM	Transmission Electron Microscopy
UV-Vis	Ultraviolet–Visible
Raman	Raman Spectroscopy
EIS	Electrochemical Impedance Spectroscopy
IMVS	Intensity Modulated Photovoltage Spectroscopy
IMPS	Intensity Modulated Photocurrent Spectroscopy
I-V	Current-Voltage
PCE	Power Conversion Efficiency
QDs	Quantum Dots

Chapter 1. Introduction

1.1. Global energy issues

Energy demand is one of the most serious problems of the societies in the world. The U.S. Energy Information Administration (EIA) [1] in the recently released International Energy Outlook 2013 (IEO2013) projects refers that:

- With world gross domestic product (GDP) rising by 3.6 percent per year, world energy use will grow by 56 percent between 2010 and 2040. Half of the increase is attributed to China and India.
- Renewable energy and nuclear power are the world's fastest-growing energy sources, each increasing by 2.5 percent per year; however, fossil fuels continue to supply almost 80 percent of world energy use through 2040.
- Given current policies and regulations, worldwide energy-related carbon dioxide emissions are projected to increase 46 percent by 2040, reaching 45 billion metric tons in 2040.

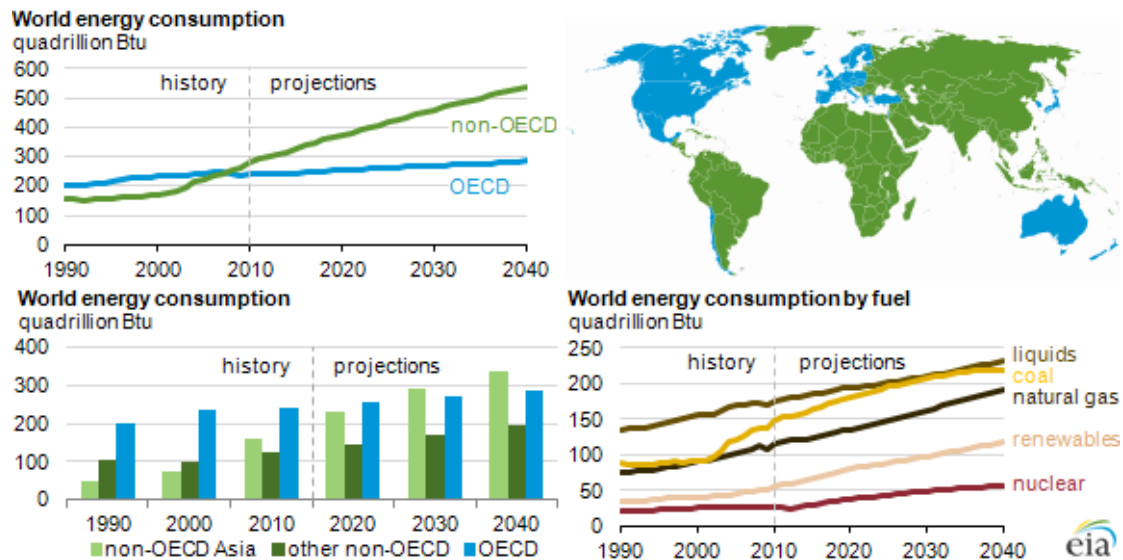


Figure 1-1. World energy consumption data [1]. Organization for Economic Co-operation and Development (OECD) i.e. developed countries, non-OECD i.e. emerging markets. 1 quadrillion Btu = 2.93×10^{11} KWh.

Taking into consideration the EIA's perspectives and the data which are presented into **Figure 1-1**, the demand for renewable energy sources is growing every day. The most accessible, clean and abundant source is the sun.

According to one of the latest publications of International Energy Agency (IEA, Greece joined the IEA in 1976) [2] the "Solar Energy Perspectives", the sun (**Figure 1-2**, Solar radiation spectrum) offers a considerable amount of power: about 885 million terawatt-hours (TWh) reach the earth's surface in a year, that is 6 200 times the commercial primary energy consumed by humankind in 2008 – and 4 200 times the energy that mankind would consume in 2035. In other words, it takes the sun one hour and 25 minutes to send us the amount of energy we currently consume in a year. By 2035, this number would grow to a little more than two hours.

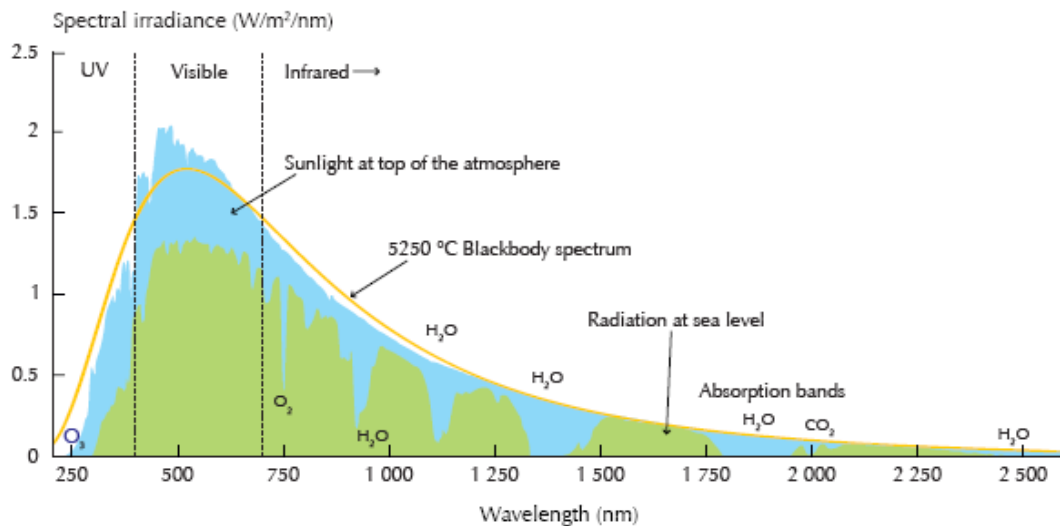


Figure 1-2. Solar radiation spectrum [2].

Regarding the above findings, it comes up as a natural sequence that, the sun's exploitation with the photovoltaics (PV) devices is maybe the most promising and green solution to the growing energy demands.

1.2. General considerations about the photovoltaics

Some milestones at the timeline of the photovoltaic evolution (with respect to the Dye Solar Cells-DSCs) from their beginning till to date are:

- 1839 - A. E. Becquerel observes the photovoltaic effect.
- 1954 - Bell Labs produce silicon solar cells.
- 1968 – H. Gerischer and sensitize zinc oxide crystals and detect photocurrent [3].
- 1991 - M. Gratzel and B. O'Regan invent the DSC, with an about 7-8 % efficiency [4].
- 2013 – H. J. Snaith reports 15 % efficiency in an improved DSC form, the perovskite solar cell or solid state Dye Solar Cell (ssDSC) [5].

In the **Figure 1-3** [6] are displayed a road map for the best research cell efficiencies.

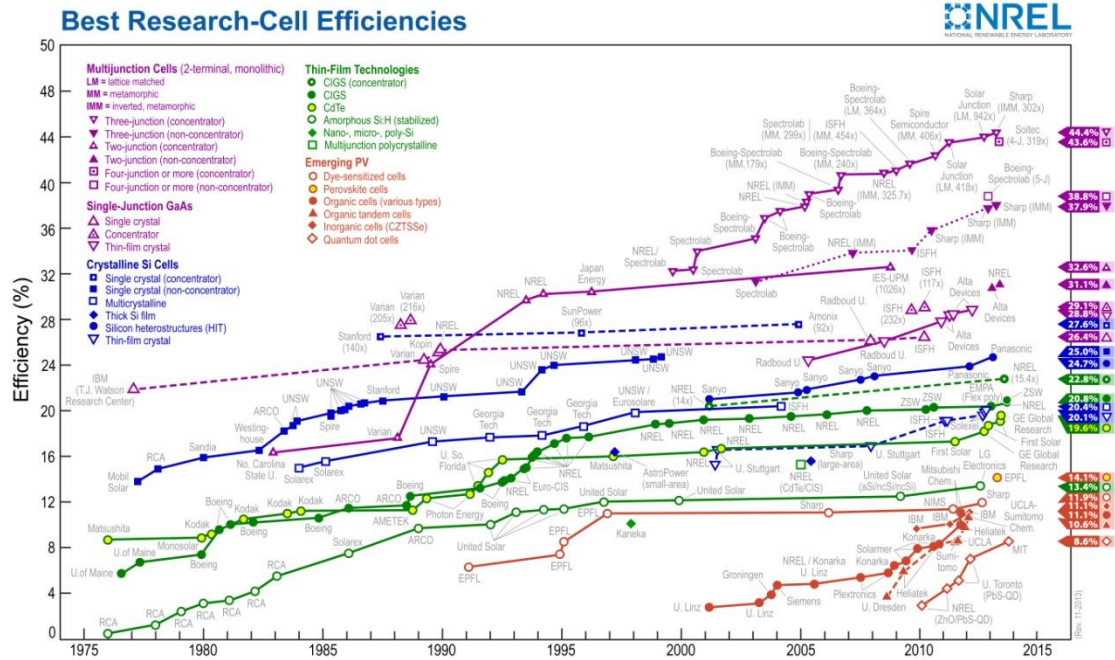


Figure 1-3. Road map for the best research cell efficiencies (National Renewable Energy Laboratory-NREL) [6].

From the **Figure 1-3** one can state that, the first generation silicon PVs have reach 25 % in yield, the second generation thin film PVs are at about 20 % and the third generation multi-junction PVs have exceeded the astonishing 40 % in power conversion efficiency. Furthermore, it is noted the increased course in the DSCs' efficiency, something which is also affirmed and by the exponentially increased number of related publications in this field, **Figure 1-4** [7].

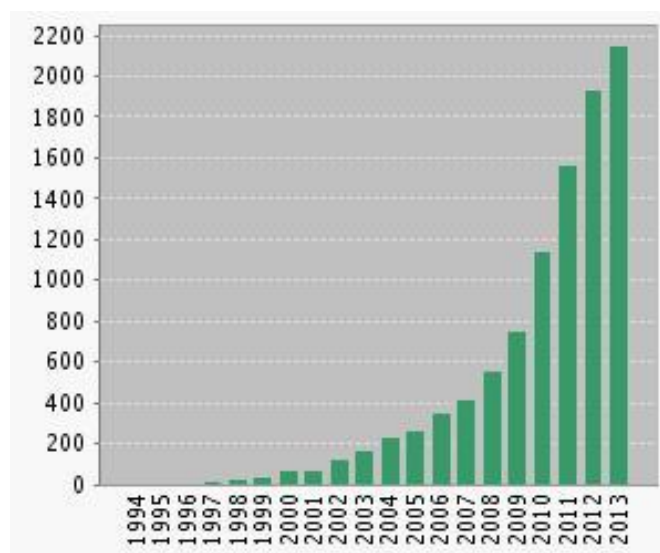


Figure 1-4. Number of publications per year obtained from a literature search using the keywords “dye sensitized” and “solar cell” (ISI Web of Knowledge) [7].

Since the breakthrough report of M. Gratzel and B. O'Regan in 1991 [4] and their pioneering idea to sensitize a mesoporous semiconductor electrode with a high internal surface area, a great progress has been succeeded in both, Dye Solar Cells and Pervoskite Solar Cells (in this type of solar cell the DSCs' architecture is retained but, instead of a dye an organometallic compound, the perovskite has been used for light harvesting). The most recent state of the art efficiency values for these two types of PVs are summarized in **Tables 1-1** and **1-2** [8].

Table 1-1. Recent state of the art efficiencies values for Dye Solar Cells [8].

Published date	Device descriptions	η (%)	Comments
23/06/2006	Black dye/ I^-/I_3^- electrolyte	11.1	Incident photon to current efficiency (IPCE) of DSSCs increases with increase in the haze of the TiO_2 electrodes, especially in the near infrared wavelength region
04/11/2011	YD2-o-C8 dye/Co (II/III) tris (bipyridyl) electrolyte	12.3	The cobalt complexes were used with custom made donor- π -acceptor zinc porphyrin molecules Cosensitisation with Y123 resulted in a record efficiency
03/01/2012	Black dye+Y1 co-adsorbent/ I^-/I_3^- electrolyte	11.4	Donor-acceptor type coadsorbents were used to avoid the dye aggregation

Table 1-2. Recent state of the art efficiencies values for Perovskite Solar Cells [8].

Published date	Device descriptions	η (%)	Comments
05/10/2011	FTO/TiO ₂ /TiO ₂ +Y123 dye/spiro-OMeTAD + FK102/Ag	7.2	Y123 dye and FK102 for p-type doping in spiro-OMeTAD
08/03/2012	FTO/TiO ₂ /Sb ₂ S ₃ + P3HT:PCBM / PEDOT:PSS/Au	6.3	Inorganic-organic heterojunction solar cell by Sb ₂ S ₃ sensitising
24/05/2012	FTO/TiO ₂ /TiO ₂ +N719 dye/ CsSnI _{2.95} F _{0.05} :SnO ₂ /Pt	8.5	CsSnI _{2.95} F _{0.05} :SnO ₂ as p-type perovskite material
21/08/2012	FTO/TiO ₂ /TiO ₂ +CH ₃ NH ₃ PbI ₃ / spiro-OMeTAD/Au	9.7	CH ₃ NH ₃ PbI ₃ perovskite as n-type material
02/11/2012	FTO/TiO ₂ /Al ₂ O ₃ +CH ₃ NH ₃ PbI ₂ Cl/ spiro-MeOTAD/Ag	10.9	CH ₃ NH ₃ Pb ₂ Cl perovskite as n-type material
27/03/2013	FTO/TiO ₂ / Al ₂ O ₃ +CH ₃ NH ₃ PbI ₃ - _x Cl _x /spiro-OMeTAD/Ag	12.3	Optimised structure by improving the crystallisation with less than 150 °C fabrication process
05/05/2013	FTO/TiO ₂ /TiO ₂ +CH ₃ NH ₃ PbI ₃ / PTAA/Au	12.0	CH ₃ NH ₃ PbI ₃ perovskite as n-type material and PTAA as the HTM
18/07/2013	FTO/TiO ₂ /TiO ₂ +CH ₃ NH ₃ PbI ₃ /Co (III) doped spiro-MeOTAD/Au	15.0	CH ₃ NH ₃ PbI ₃ perovskite as n-type material and 10% Co(III) complex doped spiro-MeOTAD as the HTM

The current top values for the Dye Solar Cells are 12 % and for the Perovskite Solar Cell 15 %. These efficiencies are high enough to justify the increased interest for the DSCs and to intrigue for further research activity.

1.3. Objectives and motivations

The objectives of this study concern:

- Firstly, the preparation of well controlled titania nanotubes via anodic oxidation of titanium (chapters 3 and 5).
- Secondly, the integrated characterization (morphological and structural) of TNTs (chapters 4 and 5).
- Thirdly, the application of the nanotubular photoelectrode in the Dye Solar Cell (chapters 3-6) as an alternative to the usual nanoparticulate one.

The elaboration of this thesis was based on the triple motivation of learning-development-dissemination of knowledge about the TNTs' growth mechanisms and the operational principles of the DSCs. Additionally the development of the existing DSCs, through the manipulation of the titania architectures, the low cost production of the nanotubular photoelectrodes and the flexibility-usability which these provide, was a strong impulse for this research. [9,10]. The

ultimate aim is the outcome of this research to have a significant contribution to the literature of DSCs.

1.4. References

1. EIA. Available at: www.eia.gov
2. IEA. Available at: www.iea.org
3. H. Gerischer, H. Tributsch Ber. "Electrochemical studies on the spectral sensitization of zinc oxide single crystals" Bunsen-Ges. Phys. Chem. 72 (1968) 437.
4. B. O'Regan, M. Graetzel "A low-cost, high-efficiency solar cell based on dye-sensitized colloidal TiO₂ films" Nature 353 (1991) 737.
5. M. Liu, M. B. Johnston, H. J. Snaith "Efficient planar heterojunction perovskite solar cells by vapour deposition" Nature doi:10.1038/nature12509.
6. NREL. Available at: www.nrel.gov
7. ISI Web of Knowledge. Available at: www.isiknowledge.com
8. H. M. Upadhyaya, S. Senthilarasu, M-H. Hsu, D. K. Kumar "Recent progress and the status of dye-sensitized solar cell (DSSC) technology with state-of-the-art conversion efficiencies" Sol. Energ. Mat. Sol. 119 (2013) 291.
9. C. A. Grimes, G. K. Mor, "TiO₂ Nanotube Arrays Synthesis, Properties, and Applications" Springer (2009).
10. H-P. Jen, M-H. Lin, L-L. Li, H-P. Wu, W-K. Huang, P-J. Cheng, E. W-G Diao "High-Performance Large-Scale Flexible Dye-Sensitized Solar Cells Based on Anodic TiO₂ Nanotube Arrays" ACS Appl. Mater. Interfaces, 5 (2013) 10098.

Chapter 2. Literature Survey

2.1. Electrochemical synthesis of the TiO_2 nanotubes

2.1.1. Titanium dioxide (TiO_2)

Titania (TiO_2) is a mineral oxide which is mainly sourced from the ore ilmenite (FeTiO_3). The most common use of titania is as a white pigment, in cosmetics, toothpastes, sunscreens, self-cleaning materials and food (E171). The production in TiO_2 pigment on the year 2012 touches the 7.000 tons worldwide, according to the U.S. Geological Survey [1]. Titanium dioxide is chemically and biologically stable, non-toxic and easily producible with low cost (selling price for the crude ore of \$11.75 per kilogram [1]). TiO_2 is founded in several crystal forms, but the best known are the anatase, rutile and brookite. Rutile is thermodynamically the most stable form, anatase is however preferred for energy applications, because it has better electrical characteristics [2]. The crystal structure of the anatase belongs to the tetragonal system and its basic building unit is the octahedral **Figure 2-1** [3]. TiO_2 has reflective index $n=2.5$, band gap $E_g=3.2$ eV [4] and is an n type semiconductor, due to crystal defects (oxygen vacancies, Ti^{3+} ions) [5].

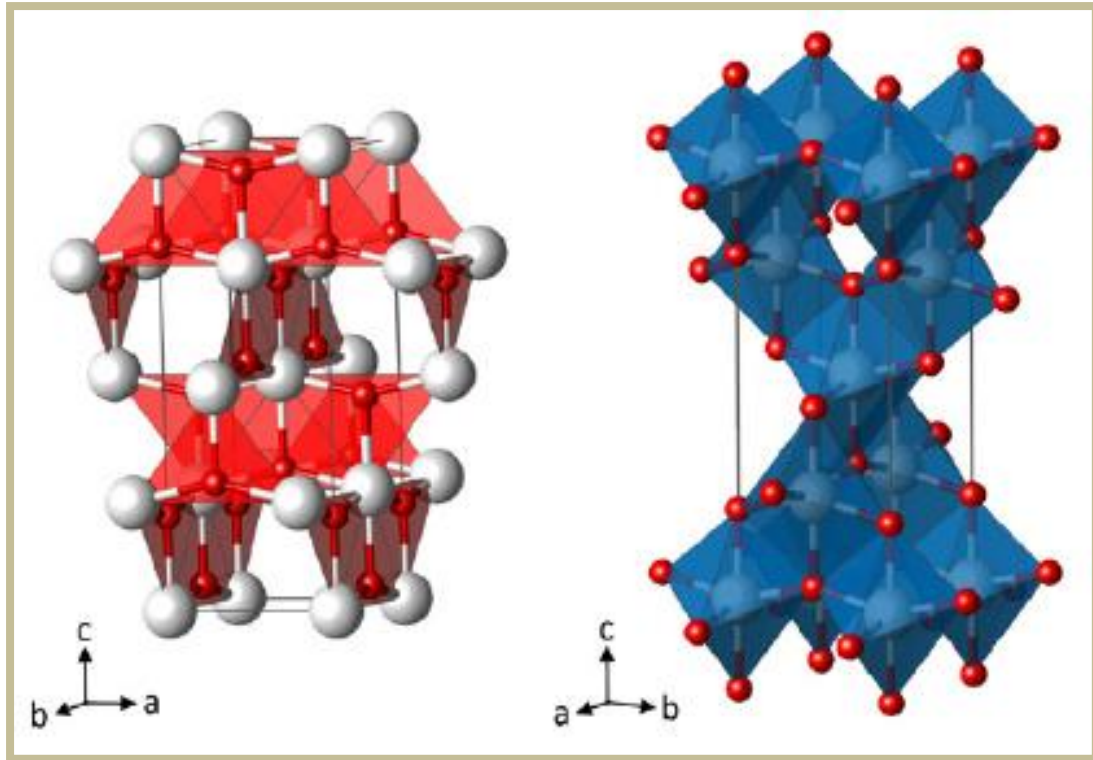


Figure 2-1. Planar Ti_3O building-block representation (left) and TiO_6 octahedral (right) for the TiO_2 anatase phase (Ti-white, O-red) [3].

2.1.2. Brief history on the electrochemical synthesis of the TiO_2 nanotubes

The discovery of the carbon nanotubes [6] stimulated intensive research activity in a wide range of materials round this special morphology. Nanotubes have been established in the literature as an advanced 1D structure. They belong in the same family of 1D materials (together with nanowires and nanorods), due to their lengthwise growth [7]. A lot of works in the literature have taken advantage of their 1D character and their unique properties (including vectorial electron transport and discovery of an antenna Raman effect [8]) to apply them in promising solar energy conversion to electricity applications, exploiting the transport directionality that they offer to the photogenerated charges [9,10].

There are literature references on the electrochemical preparation of the titania nanoporous materials since 1987 [11], but a

real impulse was given in 1999 by Zwillig and co-workers [12,13] in their original works about the anodic oxidation of titanium and its alloys in acidic electrolytes. Self-assembled titania nanotubes are easily prepared by anodic oxidation of a titanium substrate, in fluoride based electrolytes [14]. The potential applications of the TNTs cover a wide research range, photovoltaics [15], photocatalysis [16], photoelectrolysis [17], gas sensing [18], biomedical implants [19] and batteries [20].

Up to date the anodic oxidation of Ti in Fluoride (F^-) rich environments has been passed through three phases. In the first generation the synthesis was done in acidic (HF) water based electrolytes [21,22], but due to highly corrosive solutions the nanotubes' thickness were confined to some hundred of nanometers. The second generation nanotubes were grown in buffered neutral electrolytes which contained NaF, KF or NH_4F instead of HF [23], thus the thickness of TNTs layers was increased and reached some micrometers. It was although, the third growth generation of nanotubes in organic polar electrolytes (mainly ethylene glycol) almost free of water [24], that enables the development of thick layers/membranes (1 mm) [25] and in a variety of morphologies (single wall, double wall, multilayer and branched nanotubes) [26-29]. A more detailed discussion about the sophisticated nanotubular morphologies that were came across during this study is incorporated in the thesis' appendix.

Even nowadays, the anodically prepared TNTs continue to be at the forefront of the research activity [30]. The **Figure 2-2** displays a representation of the self-organized and oriented nanotube arrays and highlights their major assets.

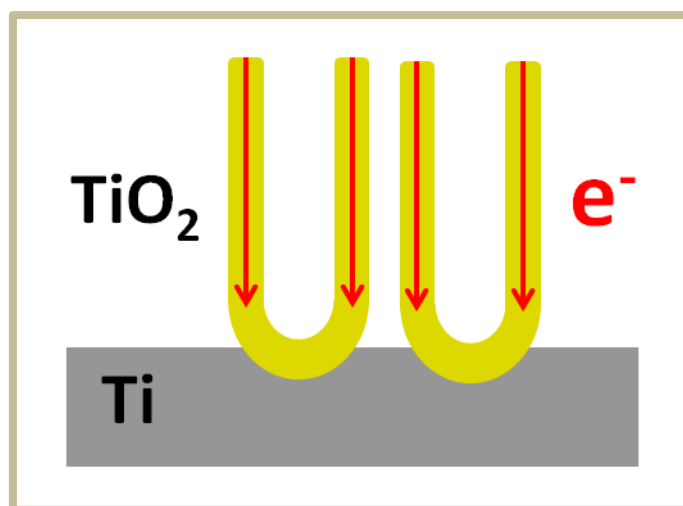


Figure 2-2. Representation of the vectorial electron transport at the nanotubes.

The nanotubes are particularly favorable in energy applications due to their unique electrical and structural properties [31]. The existence of a continuous wall eliminates the grain boundaries, minimizes the electron trapping/detrapping and ensures the vectorial electron transport without significant losses [32]. On the other hand the electrochemical preparation provides easily controllable 1-D morphology at the nanoscale; in fact, the nanotube can be modified in order to be easily accessible for doping, infiltration and diffusion concepts [33-34].

2.1.3. Anodic oxidation of titanium

The **Figure 2-3** presents an electrochemical cell and the final product of the titanium anodic oxidation, the TiO₂ nanotubes.

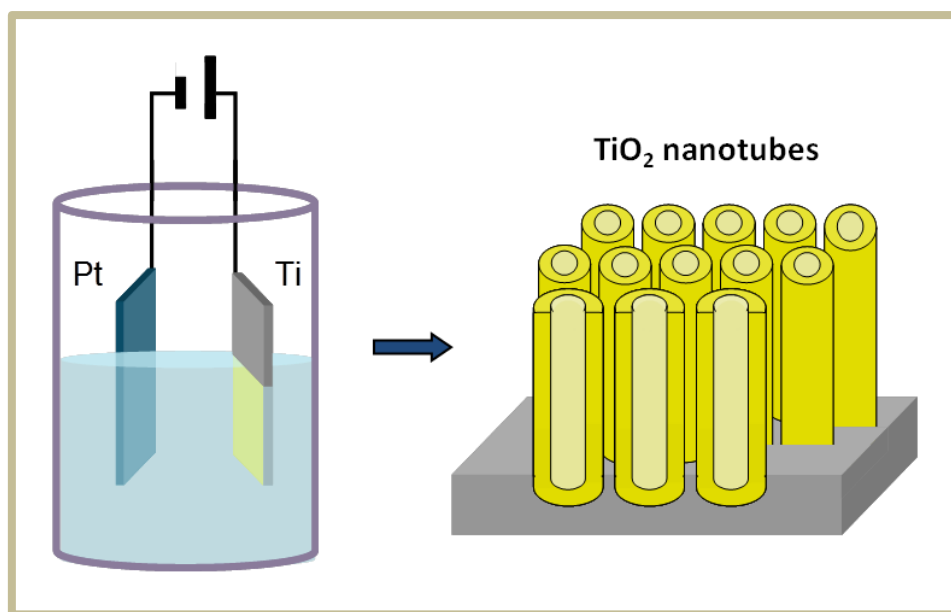


Figure 2-3. Electrochemical cell (left) and shaped TiO_2 nanotubes (right).

The electrochemical configuration is constituted by a temperature controlled and inert to chemicals (made by Teflon-PTFE) cell, the electrolyte, the two electrodes and an external source. The apparatus is supplied either by constant potential (potentiostatic oxidation) [36], or by constant current (galvanostatic oxidation) [37]. The working electrode (anode) is a titanium foil and the counter electrode (cathode) is usually a platinum foil or mesh. The electrolyte consists of the main solvent (a polar organic compound-ethylene glycol), the co-solvent (H_2O) and the supporting electrolyte (NH_4F). Each one of these parameters plays a crucial role on the nanotubes growth. The temperature governs the growth and the dissolution rate and subsequently the length of the nanotubular film [38]. The applied bias/current induces the Faradaic (ionic) current, controls the tube diameter, the thickness of the nanotubes walls and the growth rate [39]. The main solvent (ethylene glycol) is responsible for the conductivity, the pH and the kinetics of the ions within the electrolyte [40,41]. The co-solvent (H_2O) determines the conductivity, controls the thickness of the nanotubes walls, offers the oxygen for the oxidation of titanium and manages the growth rate [42]. The supporting electrolyte NH_4F causes the titanium etching (nanotubular morphology) and the

dissolution of TiO_2 [43]. Additionally, of the same importance is the duration of the oxidation, the time adjusts the length of the nanotubular film [44]. As it is concluded and indicated in the Table 2-1, the most of the parameters are interrelated; therefore in order to achieve the desirable morphology a balance is need to set up among them.

Table 2-1. Correlation of the NTs' features with the anodization parameters.

Cell \ NTs	Thickness	Diameter	Wall	Growth Rate	Dissolution Rate	Optimum NTs
V/J ↑	↑	↑	↑	↑	↑	Depending on the morphology in quest, generally a tuning of all the parameters should be done
NH_4F ↑	↑	—	↓	↑	↑	
H_2O ↑	↓	↑	↑	↓	↓	
t ↑	↑	—	↓	↓	—	
T ↑	↑	—	↓	↑	↑	

Once the two electrodes have been immersed in the electrolyte and the cell has biased the oxidation begins. The anodization procedure has three stages as shown in the **Figure 2-5**.

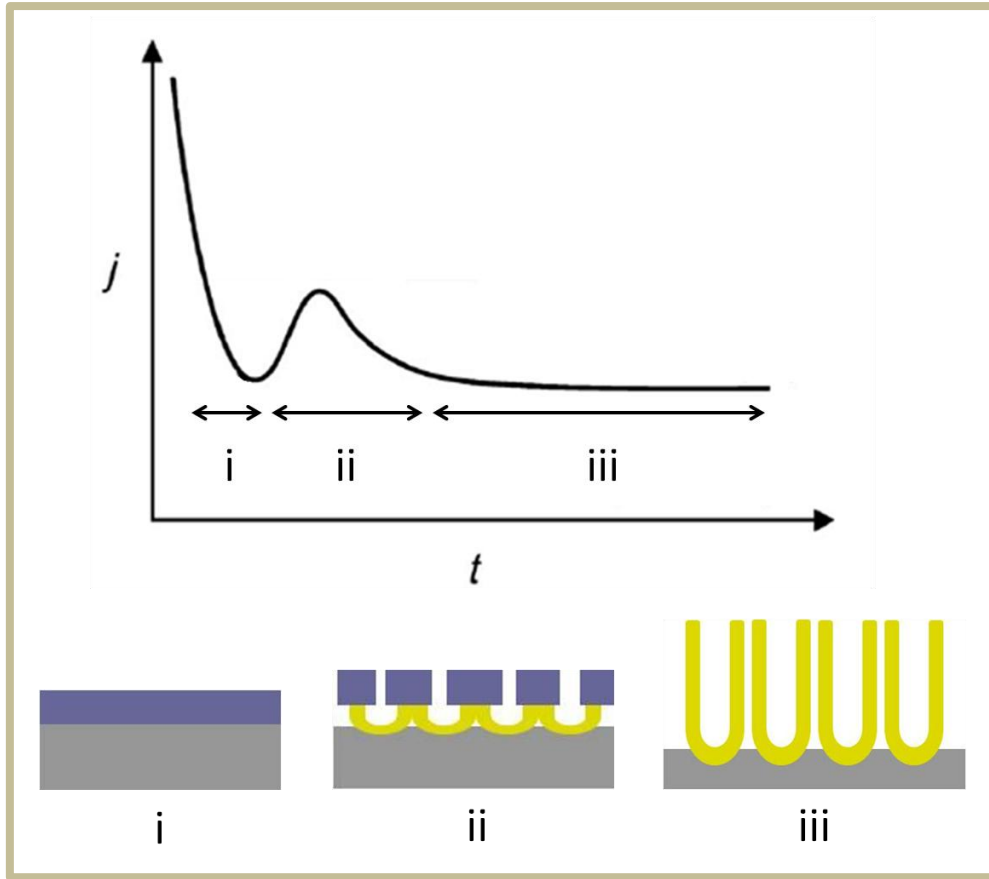
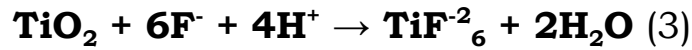
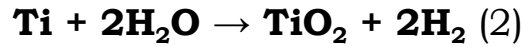
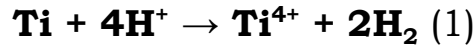


Figure 2-5. The potentiostatic anodization's evolution in three stages and the corresponding current-time (j - t) graph.

In the initial stage (i), during the first 1-2 minutes, an abrupt decay of current happens, due to the formation of a compact TiO_2 layer (blue color) at the Ti surface (gray color) [45]. Thereafter, owing to some “weak” points on the compact TiO_2 layer, the electrolyte's fluoride ions/ F^- (and the oxygen ions too) start to penetrate through it; when the ions reach the Ti/ TiO_2 interface, they start to create a new porous-tubular layer (yellow color), this transition lasts 10-15 minutes (ii) [45]. At the third stage (iii), a quasi steady state is established; the anodic current remains almost constant and the tubes continue to grow further [45].

During the anodization certain electrochemical reactions occur inside the cell. The Ti anode is oxidized-losing electrons (TiO_2 formation) and on the Pt cathode the reduction of the hydrogen ions occurs, gaining electrons (H_2 gas released); the sum of these two

activities is equation (1), the total redox reaction that takes place in the cell.



The reactions (2) and (3) describe the chemical way that the oxide is composed and dissociated respectively. Specifically, equation (2) is the overall electric field driven oxidation of the metal at the oxide/metal interface [42] and (3) is the field assisted oxide dissolution at the electrolyte/oxide interface [46]. Nanotubes' generation is possible only when a balance between these two competitive reactions is settled. If the dissolution rate is too high, the Ti/TiO₂ are solvated in the electrolyte and only corrosion is observed; on the other hand when the dissolution rate is negligible, only a thick TiO₂ compact layer is detected [45]. It is clear now that the chemical dissolution of TNTs plays a key role in the formation of nanotubes.

Taking a closer look at the mechanistic model of nanotubes array development in **Figure 2-6** [47,48], one could note a few crucial points. In **Figure 2-6** (a) the fluoride and the oxygen anions transport through the oxide (due to small ionic radius) and cause the etching and the oxidation (growth rate) of the Ti (2); simultaneously, at the electrolyte/oxide interface the TiO₂ is dissolved (dissolution rate) according to (3). When the growth rate becomes equal to the dissolution rate (after prolonged anodization) the development of the tubes stops [49]. **Figure 2-6** (b) presents the flow mechanism, that the oxide's volume is expanded from the bottom where is composed to the top of the tubes [47].

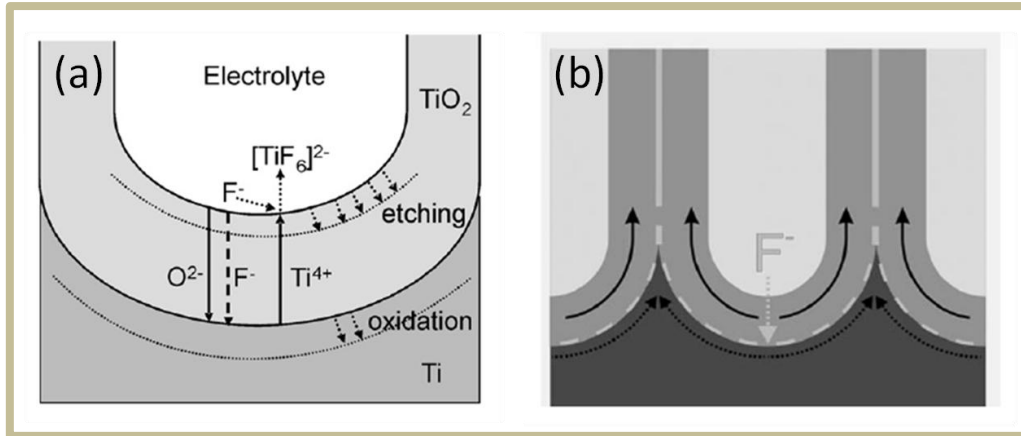


Figure 2-6. Mechanistic model for the nanotubes development (a), flow mechanism for the upwards oxide's expansion (b) [47].

The last remark concerns the formation of nanotubes instead of a nanoporous structure. The precise origin remains under delegation, but it is believed that this separation is due to the weaker and more soluble outer parts of nanotubes [50].

So far, TNTs have been displayed in many representations schematically, but how do the nanotubes look like macroscopically and microscopically? **Figure 2-7** shows the photos of an anodized titanium foil (a) and a nanotubular film (membrane) that has detached from the Ti substrate [51]. The circular anodized area (yellow circuit) is about 1.32 cm².

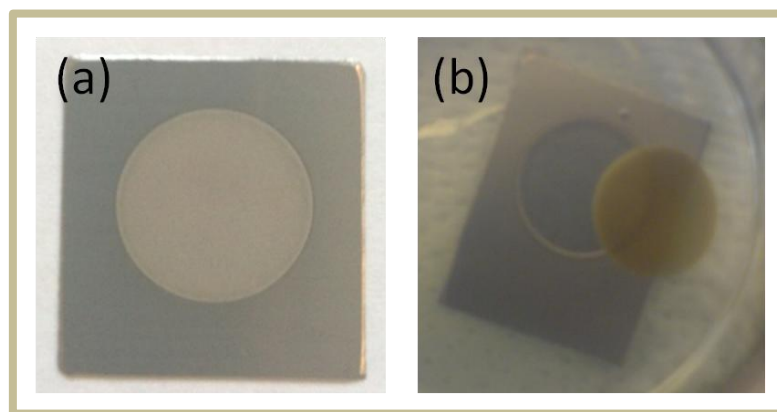


Figure 2-7. Photos of an anodize Ti foil (circular part) (a), detached TNT film (membrane) (b).

The microscopically view of the **Figure 2-8** is more interesting; some impressive oxide architectures are shown in different perspectives.

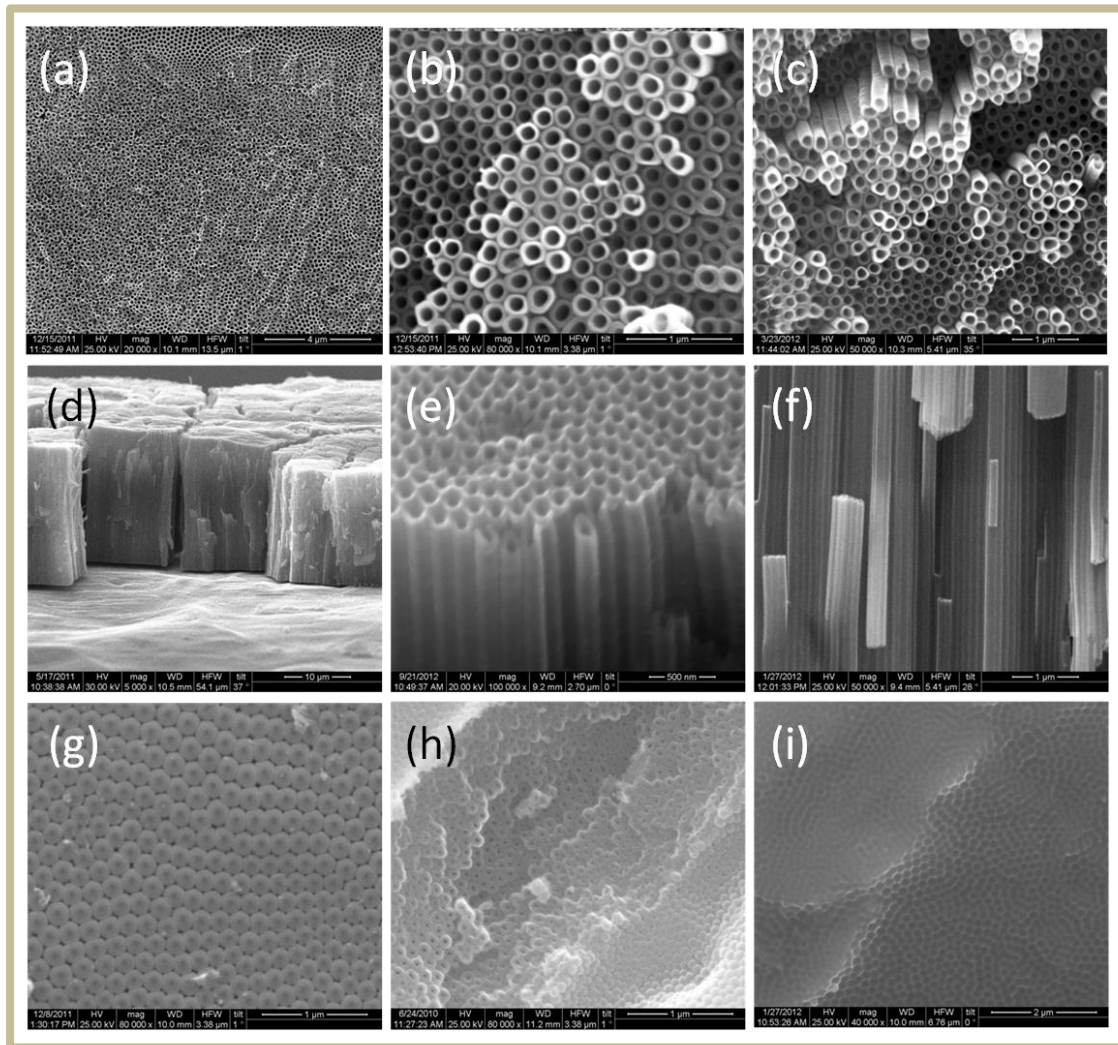


Figure 2-8. SEM (scanning electron microscopy) images of the TiO_2 nanotubes. Top surface of NTs (a)-(c), cross section of the NTs (d)-(f), bottom of the NTs (g),(h), patterned Ti foil after the detach of TiO_2 nanotubular film-membrane (i).

The **Figures 2-8** (a)-(c) and (d)-(f) SEM (scanning electron microscopy) demonstrate a few homogeneous top surfaces and cross sections correspondingly, of some self assembled titania nanotube samples, in various magnifications and perspectives. Image (g) shows the bottom of the NTs after the detachment of the TiO_2 film from the Ti foil (which has a patterned area now-(i)) and last (h) is again a view of the nanotubes' bottom with some caps to have been removed. As soon as the TNTs have been developed they are amorphous, but with the optimum annealing they can obtain the preferable crystallinity [52,53].

Finalizing this marathon chapter about the anodization procedure, there is enough room for one last comment; it is almost “seductive” the way that the electrochemistry can be at the same time so effective and creative.

2.2. Dye solar cell (DSC)

2.2.1 Front side illuminated DSCs

Dyesol is one of the global leading companies in the construction of DSCs [54]. Head researchers in Dyesol’s R&D department H. Desilvestro and D. Milliken believe that by 2018, it is possible DSCs and in particular solid state DSCs will reach efficiencies of 20 % (30 % is the maximum theoretical attainable efficiency for single junction cell) [55] with a parallel cost reduction. Characteristically, it is expected that the DSCs’ manufacturing cost will be much lower than that of the Si PV. Also, Dyesol has performed and surpassed a lot of durability tests (5000 hours DSC stability at elevated temperature, according to its announcement in the EMRS 2013 Strasburg meeting) with a view to certification of the international standards before the products commercialization. The PV market is rapidly expanding and soon (the next 20 years) [56] the solar generated electricity will be one of the most economical (half that of coal \$99.60 per MWh) and at the same time a source of green energy. DSC technology includes a series of advantages: low energy and cost manufacturing process, wide use of abundant non toxic materials in small quantities, increased energy collection in real world solar conditions and incorporation in building materials (windows, roofs) with high aesthetical and variable results [54]. Today, cutting-edge DSC technology still stays on track since its birth on 1991.

The Dye Solar Cell has a multilayer-sandwich structure, **Figure 2-9** [54]. In basic realization a DSC comprises a layer of nanoparticulate titania [57] formed on a transparent electrically conducting substrate (conductive glass-TCO) and photosensitized by a monolayer of Ruthenium complex dye [58]. An electrolyte, based on an Iodide-tri-iodide redox system [59] is placed between the layer of photosensitized titania and a second electrically conducting catalytic substrate [60].

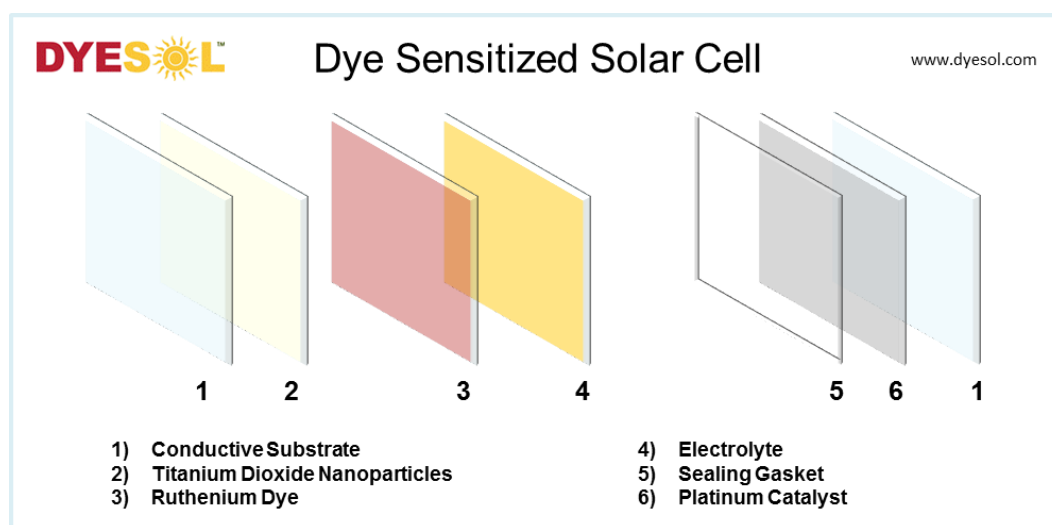


Figure 2-9. Schematic overview of the DSC multilayer structure. [54].

The exciting trick of the sensitization of a transparent semiconductor (TiO_2) with a visible light absorbing dye lies in the heart of DSC's operation mechanism, **Figure 2-10** [61]. The dye is excited after a photon absorption, equation (4) [62] and injects an electron into the conduction band of the TiO_2 , equation (5) [62]. Then the electron is transported from one TiO_2 nanoparticle to another [63] till it arrives at the conductive substrate, in which it is collected from the external circuit. The oxidized state of the dye is restored to its ground state by an electron transfer from the electrolyte, equation (6) [64]. The regenerative cycle is completed at the cathode where the electrolyte is reduced by receiving electron from the external circuit, equation (7) [64].

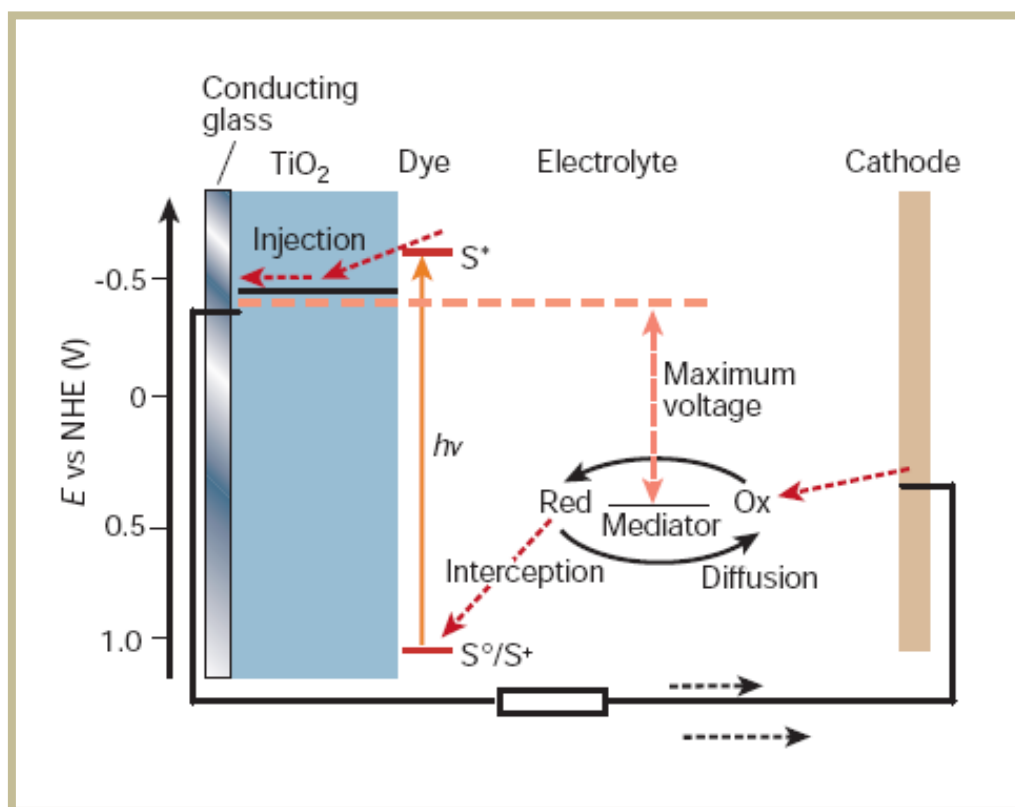
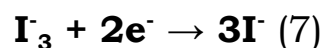
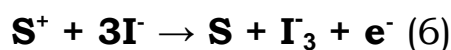
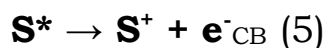
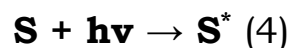


Figure 2.10. Principle of operation and energy level scheme of the dye-sensitized nanocrystalline solar cell [61].



Besides this simple view, of a DSC it should be noted that the current generation is a competitive (time dependant) process, among the forward (4)-(7) reactions and some recombination reactions, which are illustrated in **Figure 2-11** [65]. The cell's kinetics depends on each component (e.g. the solvent of the redox couple) and the interface reactions. All these define the whole cell performance [66].

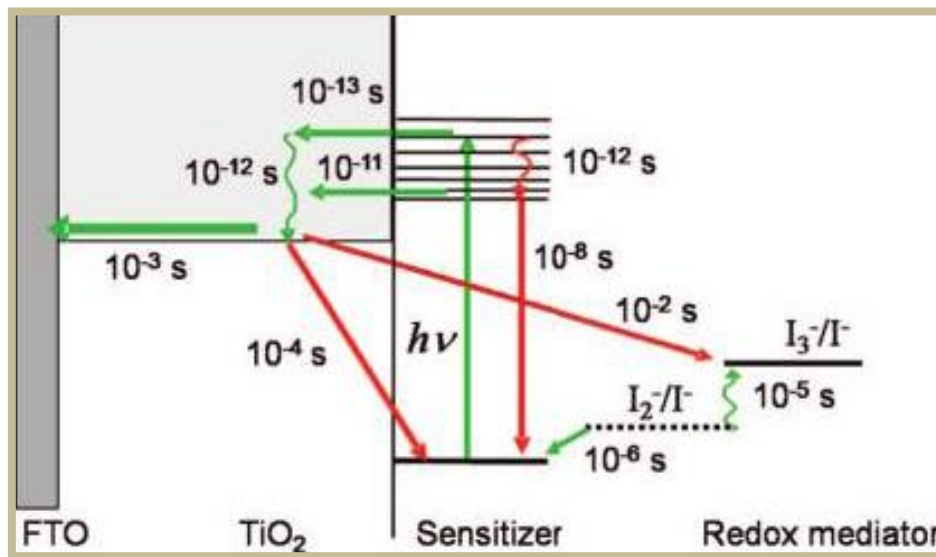


Figure 2-11. Kinetics of a Ru-based sensitized TiO_2 solar cell with I^-/I_3^- redox mediator. Typical time constants for the forward reactions (green arrow) and the loss-recombination reactions (red arrow) [65].

The TiO_2 film morphology is of vital importance and must fulfill some crucial criteria in order to be an appropriate substrate. The total film thickness usually is about 10 microns, with nanoparticles of 10-30 nm and optimum porosity round to 50-60 % [67].

In order to evaluate PVs at any stage of the production, laboratorial or commercial, the cell's performance must be known as well as the rest of the electrical parameters that are simply estimated from the I-V curve, **Figure 2-12**.

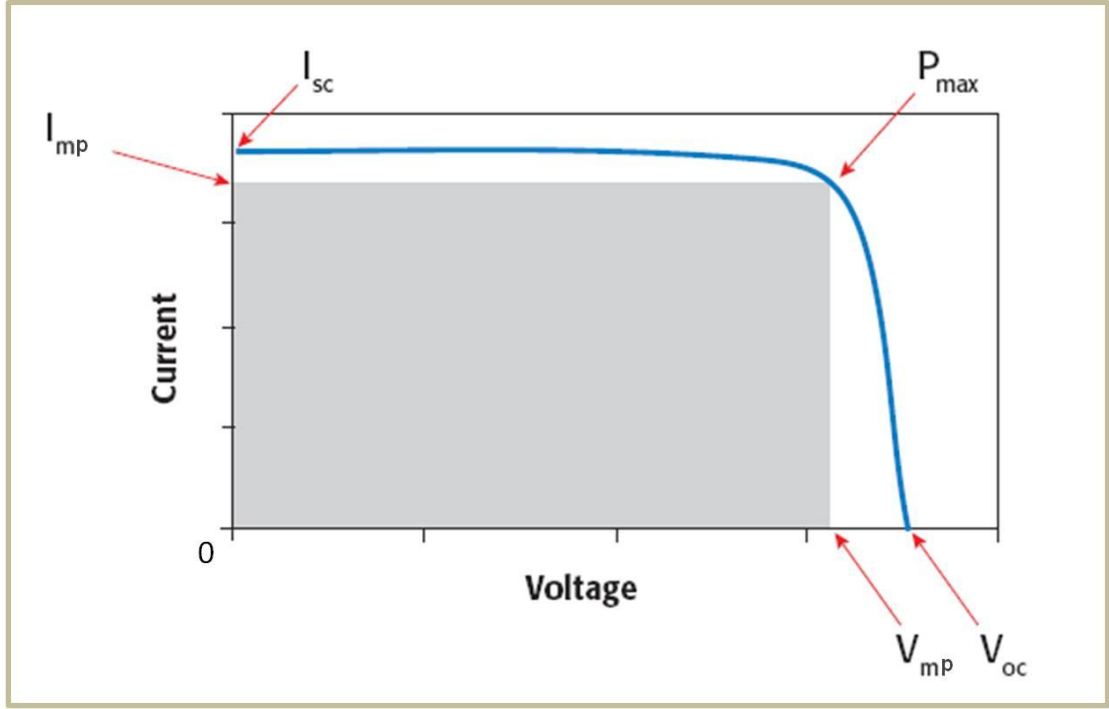


Figure 2-12. Characteristic I-V curve of a PV and the corresponding electrical parameters.

The overall solar to electrical energy conversion efficiency (η) for a solar cell is given by equation (8) [68], by the photocurrent density measured at short-circuit (J_{sc}), the open-circuit photovoltage (V_{oc}), the fill factor of the cell (FF) and the intensity of the incident light (P_{in}). The fill factor can attain values between 0 and 1 and is defined by the ratio of the maximum power point (P_{max}) divided by the ($V_{oc} * J_{sc}$) product according to equation (9) [69]. The maximum power point (P_{max}) is obtained as the product of the maximum density of current and voltage ($V_{mp} * J_{mp}$). The P_{in} is the input solar irradiance (1000 W/m^2 - AM (air mass) 1.5 G) [70,71], this value is equal to the solar radiation on a shiny day when the sun is at zenith.

$$\eta = J_{sc} V_{oc} FF / P_{in} \quad (8)$$

$$FF = P_{max} / J_{sc} V_{oc} \quad (9)$$

Concluding this part, it would be fair to pay some attention on the driving force behind the solar cells' energy generation. The origin of the photovoltaic effect comes from the difference between the semiconductor's Fermi level and the electrochemical potential of the electrolyte, designated as maximum voltage in **Figure 2.10**. With respect to the cell's operation conditions the V_{oc} is defined by equation (10) [72], which is one of the most important equations in the theory of photovoltaics. Where, K_B is Boltzmann's constant, T the absolute temperature, e the electron charge, I_{sc} the short circuit current and I_0 the dark or saturation current.

$$V_{oc} = \frac{K_B T}{e} \log \left(\frac{I_{sc} + I_0}{I_0} \right) \quad (10)$$

2.2.2 Back side illuminated DSCs

The main difference between the front and the back side illuminated DSCs is in the direction of the incident light, at the latter the light harvesting is realized through the counter electrode (cathode), **Figure 2.13** (a) and (b). This special characterization-preparation technique has led many groups to exploit the advantages of an alternative to glass substrate [73]. Titanium is one of the most preferable substrates, due to the low cost and the elevated conductivity in contrast to the TCO [74]. Furthermore the use of a flexible Ti foil permits its surface to be easily manipulated (roughen), in order to increase the light scattering. As a result, there are a lot of works in which the use of a titanium substrate in combination with composite TiO_2 layers [75,76] has driven to highly efficient (PCE values up to 8.5 %) back illuminated DSCs [77].

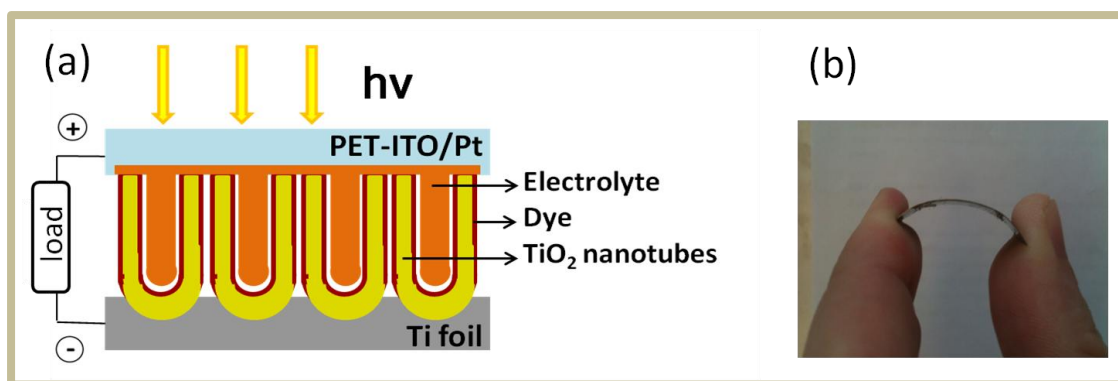


Figure 2.13. Scheme of a flexible back illuminated DSC, based on TiO_2 nanotubes (a) and the corresponding functional cell with total thickness lower than 1 mm (b).

The back illuminated DSCs based on anodically oxidized Ti foils is a distinct category of cells, that take advantage of the unique nanotubular morphology, **Figure 2.13** (a). The single nanotubular cells have attained efficiencies of about 6 % [78,79] and when they were subjected to a post treatment (commonly, decoration with TiO_2 nanoparticles) [80], reached the considerable efficiency of 8 % [81,82]. The highest yield in the classic front side illuminated nanoparticulate DSCs (**Table 1.1**) is around 12 %, this means that, the back side illuminated nanotubular DSCs remaining with about 30 % lower efficiencies. This decrease in efficiency is fully justified by light losses on the back illumination mode due to the reflection from the Pt layer at the counter electrode and the light absorption from the electrolyte [83].

However, a direct comparison between the nanoparticulate and the nanotubular DSCs will highlight the assets of the last **Figure 2-14**.

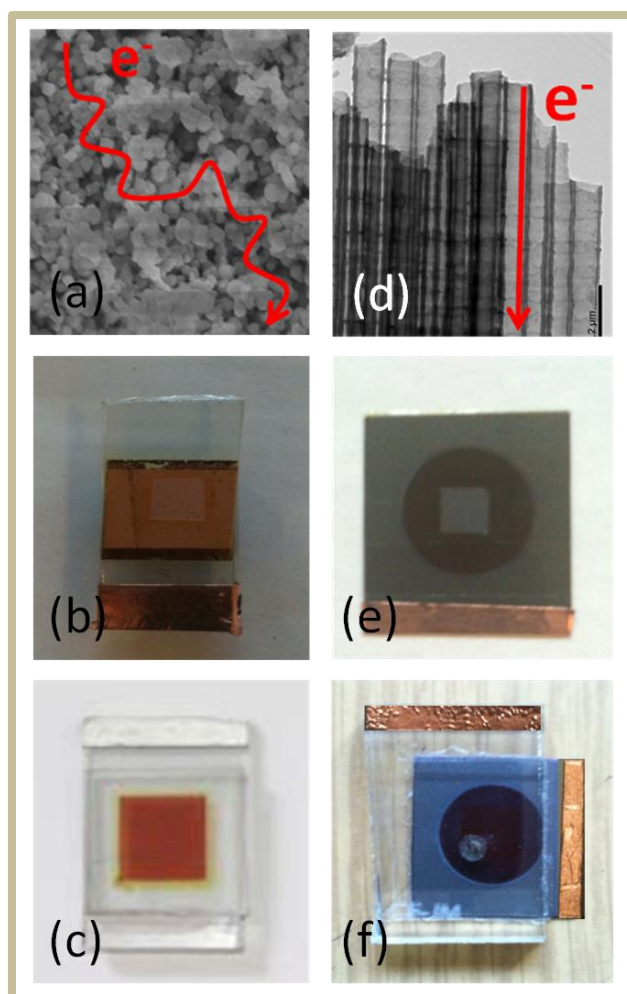


Figure 2-14. Electron transport in a nanoparticulate (a) and a nanotubular (d) TiO_2 layer. Images of a nanoparticulate front side illuminated photoelectrode (b) and the corresponding sealed DSC (c). Accordingly the nanotubular photoelectrode (e) and the back illuminated DSC (f).

The nanotubes offer a straight path with reduced grain boundaries for directed electron transport, in contradiction to the random walk on the nanoparticles [84]. The open pores of the nanotubes facilitate the electrolyte diffusion (even if it is solvent free with low viscosity), on the contrary the nanoparticulate photoelectrodes hinder the electrolyte's percolation [85]. Additionally, the coarse top surface of the tubes scatters the light better than the smooth nanoparticulate surface [86].

Nevertheless, the nanotubular DSCs haven't succeeded up to date, to cope with the high prospects for really enhanced efficiencies. The reasons for that, are grounded in the fabrication procedure. According to the exceptional studies of Boschloo [87] and

Schemuttenmaer [88], the state distribution within the band gap of the nanotubes differs substantially from the nanoparticles. The density of the shallow traps-states (Ti^{3+} defects due to oxygen vacancies, interstitial Ti and F^- ions) is extended and forms impurity bands 1 eV below the conduction band edge, which result in a vast number of exciton-like traps [88]. Also, in NTs the Fermi level and the deep traps (surface states) [89], are localized lower in the band gap than in the NPs; possibly because of a p-type doping (N and C atoms that come from the anodization electrolyte), that compensates the TNTs n-type semiconductivity by the possession of acceptor states above the valence band. Taking into consideration these notes it is understandable now why the NTs have comparable transport times to the NPs, despite their higher degree of orientation that provides them with higher electron life times [85,90].

The importance of ordering [91] is unexceptionable, but some critical factors [92] both, in the oxidation procedure and in the post treatment should be taken into account. The geometry of the tubes directly affects the DSCs performance. The nanotube wall has to be thick enough for a space charge layer to form for faster electron transportation and reduced recombination [93]. An estimated critical wall thickness is about 30-40 nm. There is also an optimum nanotube length for effective electron collection in consideration of dye loading capacity and electron diffusion length [94]. In back-side illuminated DSCs, the optimal length and pore diameter can be found as a function of the total porosity. It is strongly believed that the porosity of the nanotubular photoelectrodes must be the same as those made from nanoparticles, around 50-60 %. After that the ranges of the affordable values for the length is from 10 to 40 μm [95] and for the pore diameter from 30 to 90 nm [96]. Another tricky point, which has caused a lot of debates [97], is the removing of the structural disorder (“nanograss” dissolved NTs due to extended anodization) from the NTs’ surface. Nanograss blocks entering of the dye and the electrolyte inside the NTs and reduces the transport of the electrons due to the

increased surface recombination. Last but not least, is the importance of the post treatments and mainly the annealing. Only a few works have been published which correlate the NTs annealing conditions with the DSCs' efficiency and features [98,99]. Probably, annealing is one of the best ways to control the trap distribution within the TiO_2 band gap and subsequently to raise the cells' performance.

2.3. Experimental part

The electrochemical set-up which was used for the titanium anodization is shown in **Figure 2-15**. It consists of a conventional two-electrode configuration with platinum mesh as a counter electrode. The Ti working electrode (foil) was pressed against an O-ring (rubber), of a Teflon (PTFE) electrochemical cell, with 1.32 cm^2 exposed to the electrolyte. The Pt electrode was placed parallel to the Ti electrode at the distance of 2 cm. The potential/current was applied between the working and the counter electrode using a voltage or a current supplier. The electrolytes were prepared from reagent grade chemicals and their volume was kept stable for all the experiments at 100 ml. In order to keep the temperature of the electrolyte constant at the prolonged anodizations, a temperature control system was adjusted to the electrochemical cell [100-102].

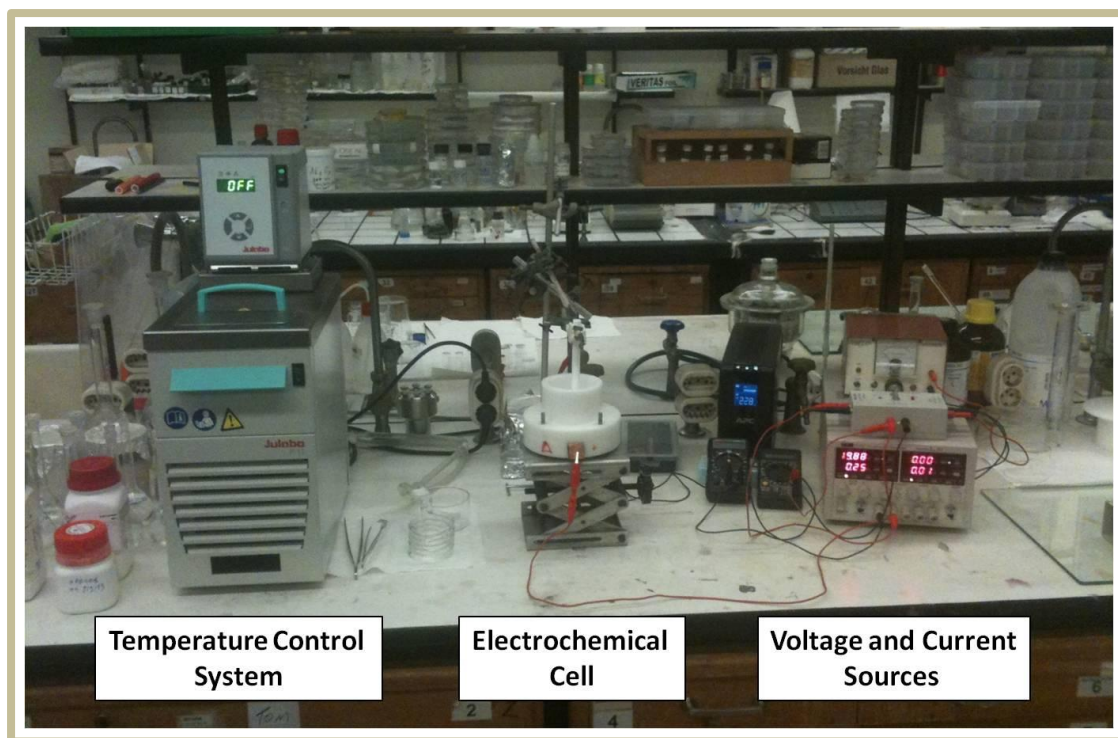


Figure 2-15. Image of the electrochemical setup for Ti anodization.

The DSCs prepared and studied with the use of the TNTs as photo-anodes. The morphological and structural characterization of the TNTs was utilized with the techniques of Atomic Force Microscopy (AFM), Scanning Electron Microscopy (SEM), Transmission Electron Microscopy (TEM), Ultraviolet-Visible (UV-Vis) and Raman spectroscopy. Additionally, the in-situ evaluation and characterization of DSCs was done taking advantage of the methods of Electrochemical Impedance Spectroscopy (EIS), Intensity Modulated Photovoltage/Photocurrent Spectroscopy (IMVS/IMPS) and lastly the power conversion efficiency experiments were conducted by the Current-Voltage (I-V) measurements **Figure 2-16**.

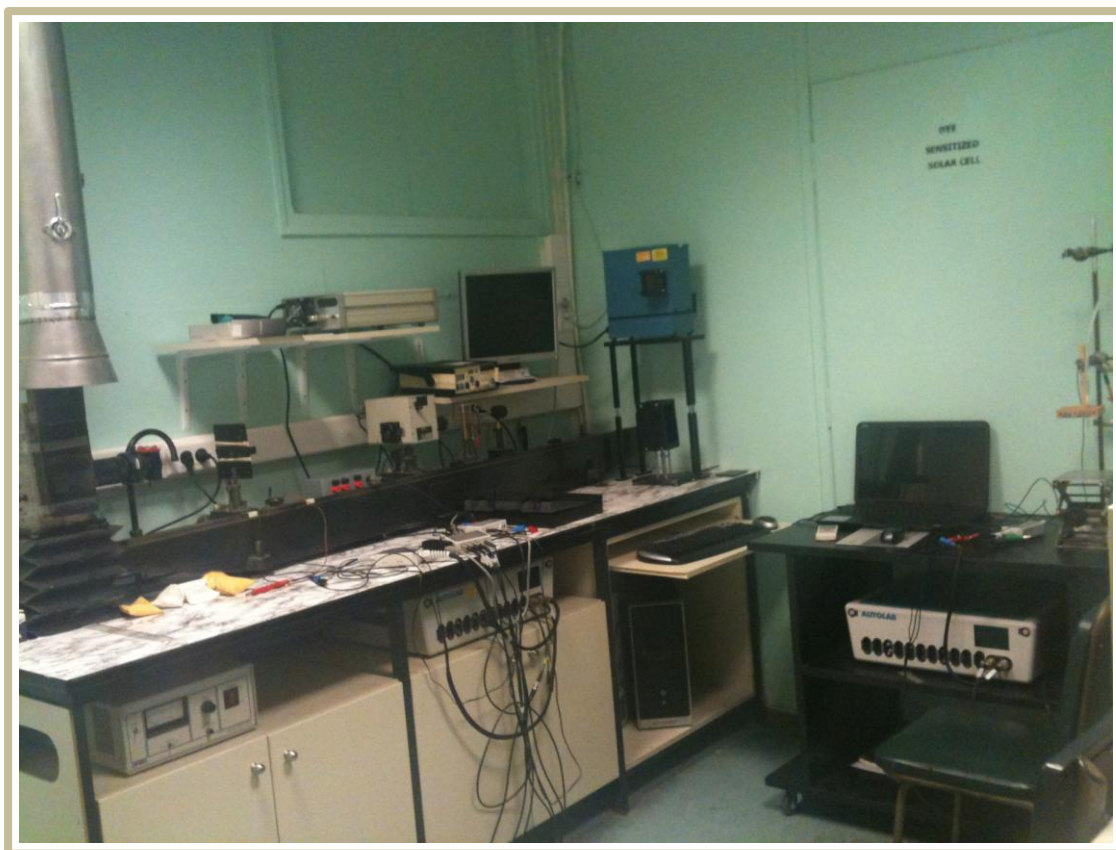


Figure 2-16. Equipment (solar simulators, potentiostats, etc) for the characterization of the Dye Solar Cells.

2.4. References

1. USGS. Available at: www.usgs.gov
2. X. Chen, S. S. Mao "Titanium Dioxide Nanomaterials: Synthesis, Properties, Modifications, and Applications" *Chem. Rev.* 107 (2007) 2891.
3. M. Landmann, E. Rauls, W. G. Schmidt "The electronic structure and optical response of rutile, anatase and brookite TiO_2 " *J. Phys. Condens. Matter* 24 (2012) 195503.
4. U. Diebold "The surface science of titanium dioxide" *Surf. Sci. Rev.* 48 (2003) 53.
5. C. Di Valentin, G. Pacchioni, A. Selloni "Reduced and n-Type Doped TiO_2 : Nature of Ti^{3+} Species" *J. Phys. Chem. C* 113 (2009) 20543.

6. S. Iijima "Helical microtubules of graphitic carbon" *Nature* 354 (1991) 56.
7. W-G. Kim, S. Nair "Membranes from nanoporous 1D and 2D materials: A review of opportunities, developments, and challenges" *Chem. Eng. Sci.* 104 (2013) 908.
8. V. Likodimos, T. Stergiopoulos, P. Falaras "Phase composition, size, orientation, and antenna effects of self-assembled anodized titania nanotube arrays: a polarized micro-Raman investigation" *J. Phys. Chem. C* 112 (2008) 12687.
9. S. Banerjee, S. K. Mohapatra, P. P. Das, M. Misra "Synthesis of Coupled Semiconductor by Filling 1D TiO₂ Nanotubes with CdS" *Chem. Mater.* 20 (2008) 6784.
10. C. A. Grimes, O. K. Varghese, G. K. Mor, M. Paulose, X. Feng "Photonic Fuels and Photovoltaics: Application of Self-Assembled 1D TiO₂ Nanotube/wire Arrays" *Abstracts of Papers of the American Chemical Society, Meeting Abstract: 39-FUEL* 239 (2010) 21.
11. M. Assefpour-Dezfuly, C. Vlachos, E. H. Andrews "Oxide morphology and adhesive bonding on titanium surfaces" *J. Mater. Sci.* 19 (1984) 3626.
12. V. Zwillling, M. Aucouturier, E. Darque-Ceretti "Anodic oxidation of titanium and TA6V alloy in chromic media. An electrochemical approach" *Electrochim. Acta* 45 (1999) 921.
13. V. Zwillling, E. Darque-Ceretti, A. Boutry-Forveille, D. David, M. Y. Perrin, M. Aucouturier "Structure and Physicochemistry of Anodic Oxide Films on Titanium and TA6V Alloy" *Surf. Interface Anal.* 27 (1999) 629.
14. A. G. Kontos, A. I. Kontos, D. S. Tsoukleris, V. Likodimos, J. Kunze, P. Schmuki, P. Falaras "Photo-induced effects on self-organized TiO₂ nanotube arrays: the influence of surface morphology" *Nanotechnology* 20 (2009) 045603.
15. T. Stergiopoulos, A. Valota, V. Likodimos, Th. Speliotis, D. Niarchos, P. Skeldon, G. E. Thompson, P. Falaras "Dye-sensitization of self-assembled titania nanotubes prepared by galvanostatic

anodization of Ti sputtered on conductive glass” *Nanotechnology* 20 (2009) 365601.

16. A.G. Kontos a, A. Katsanaki, T. Maggos, V. Likodimos, A. Ghicov, D. Kim, J. Kunze, C. Vasilakos, P. Schmuki, P. Falaras “Photocatalytic degradation of gas pollutants on self-assembled titania nanotubes” *Chem. Phys. Lett.* 490 (2010) 58.

17. P. P. Das, S. K. Mohapatra, M. Misra “Photoelectrolysis of water using heterostructural composite of TiO₂ nanotubes and nanoparticles” *J. Phys. D: Appl. Phys.* 41 (2008) 245103.

18. L. X. Yang, S. L. Luo, Q. Y. Cai, S. Z. Yao “A review on TiO₂ nanotube arrays: Fabrication, properties, and sensing applications” *Chinese Sci. Bull.* 55 (2010) 331.

19. S. Minagar, C. C. Berndt, J. Wanga, E. Ivanova, C. Wen “A review of the application of anodization for the fabrication of nanotubes on metal implant surfaces” *Acta Biomater.* 8 (2012) 2875.

20. W. Guo, X. Xue, S. Wang, C. Lin, Z. L. Wang “An Integrated Power Pack of Dye-Sensitized Solar Cell and Li Battery Based on Double-Sided TiO₂ Nanotube Arrays” *Nano Lett.* 12 (2012) 2520.

21. J. Bai, B. Zhou, L. Li, Y. Liu, Q. Zheng, J. Shao, X. Zhu, W. Cai, J. Liao, L. Zou “The formation mechanism of titania nanotube arrays in hydrofluoric acid electrolyte” *J. Mater. Sci.* 43 (2008) 1880.

22. R. Beranek, H. Hildebrand, P. Schmuki “Self-Organized Porous Titanium Oxide Prepared in H₂SO₄/HF Electrolytes” *Electrochem Solid St.* 6 (2003) B12.

23. Q. Cai, M. Paulose, O. K. Varghese, C. A. Grimes “The effect of electrolyte composition on the fabrication of self-organized titanium oxide nanotube arrays by anodic oxidation” *J. Mater Res.* 20 (2005) 230.

24. S. P. Albu, A. Ghicov, J. M. Macak, P. Schmuki “250 μ m long anodic TiO₂ nanotubes with hexagonal self-ordering” *Phys. Stat. Sol. (RRL)* 1 (2007) R65.

25. M. Paulose, H. E. Prakasam, O. K. Varghese, L. Peng, K. C. Popat, G. K. Mor, T. A. Desai, C. A. Grimes “TiO₂ Nanotube Arrays of 1000 μ m

- Length by Anodization of Titanium Foil: Phenol Red Diffusion" *J. Phys. Chem. C* 111 (2007) 14992.
26. H. Mirabolghasemi, N. Liu, K. Lee, P. Schmuki "Formation of 'single walled' TiO₂ nanotubes with significantly enhanced electronic properties for higher efficiency dye-sensitized solar cells" *Chem. Commun.* 49 (2013) 2067.
 27. Y. Ji, K-C. Lin, H. Zheng, J-j. Zhu, A. C. S. Samia "Fabrication of double-walled TiO₂ nanotubes with bamboo morphology via one-step alternating voltage anodization" *Electrochem. Commun.* 13 (2011) 1013.
 28. H-J. Oh, I-K. Kim, K-W. Jang, J-H. Lee, S. Lee, C-S. Chi "Influence of Electrolyte and Anodic Potentials on Morphology of Titania Nanotubes" *Met. Mater. Int.* 18 (2012) 673.
 29. S. P. Albu, D. Kim, P. Schmuki "Growth of Aligned TiO₂ Bamboo-Type Nanotubes and Highly Ordered Nanolace" *Angew. Chem. Int. Ed.* 47 (2008) 1916.
 30. S. Kurian, H. Seo, H. Jeon "Significant Enhancement in Visible Light Absorption of TiO₂ Nanotube Arrays by Surface Band Gap Tuning" *J. Phys. Chem. C* 117 (2013) 16811.
 31. W. Wei, G. Oltean, C-W. Tai, K. Edström, F. Björefors, L. Nyholm "High energy and power density TiO₂ nanotube electrodes for 3D Li-ion microbatteries" *J. Mater. Chem. A* 1 (2013) 8160.
 32. A. E. Mohamed, S. Rohani "Modified TiO₂ nanotube arrays (TNTAs): progressive strategies towards visible light responsive photoanode, a review" *Energy Environ. Sci.* 4 (2011) 1065.
 33. Y-C. Nah, I. Paramasivam, P. Schmuki "Doped TiO₂ and TiO₂ Nanotubes: Synthesis and Applications" *Chem. Phys. Chem.* 11 (2011) 2698.
 34. S. L. Lim, Y. Liu, G. Liu, S. Y. Xu, H. Y. Pan, E-T Kang, C. K. Ong "Infiltrating P3HT polymer into ordered TiO₂ nanotube arrays" *Phys. Status Solidi. A* 208 (2011) 658.

35. Y. Zhuo, L. Huang, Y. Ling, H. Li, J. Wang "Preliminary investigation of solution diffusive behavior on V-doped TiO₂ nanotubes array by electrochemical impedance spectroscopy" *J. Nanosci. Nanotechnol.* 13 (2013) 954.
36. A. G. Kontos, A. I. Kontos, D. S. Tsoukleris, V. Likodimos, J. Kunze, P. Schmuki, P. Falaras "Photo-induced effects on self-organized TiO₂ nanotube arrays: the influence of surface morphology" *Nanotechnology* 20 (2009) 045603.
37. H. Habazaki, Y. Konno, Y. Aoki, P. Skeldon, G. E. Thompson "Galvanostatic Growth of Nanoporous Anodic Films on Iron in Ammonium Fluoride-Ethylene Glycol Electrolytes with Different Water Contents" *J. Phys. Chem. C* 114 (2010) 18853.
38. G. D. Sulkaa, J. Kapusta-Kolodzieja, A. Brzozkab, M. Jaskuła "Anodic growth of TiO₂ nanopore arrays at various temperatures" *Electrochim. Acta* 104 (2013) 526.
39. A. Valota, M. Curioni, D. J. Leclere, P. Skeldon, P. Falaras, G. E. Thompson "Influence of Applied Potential on Titanium Oxide Nanotube Growth" *J. Electrochem. Soc.* 157 (2010) K243.
40. S. Yoriya, C. A. Grimes "Self-assembled anodic TiO₂ nanotube arrays: electrolyte properties and their effect on resulting morphologies" *J. Mater. Chem.* 21 (2011) 102.
41. X. Feng, J. M. Macak, P. Schmuki "Robust Self-Organization of Oxide Nanotubes over a Wide pH Range" *Chem. Mater.* 19 (2007) 1534.
42. S. Berger, J. Kunze, P. Schmuki, A. T. Valota, D. J. LeClere, P. Skeldon, G. E. Thompson "Influence of Water Content on the Growth of Anodic TiO₂ Nanotubes in Fluoride-Containing Ethylene Glycol Electrolytes" *J. Electrochem. Soc.* 157 (2010) C18.
43. Y. Ku, Y. S. Chen, W. M. Hou, Y. C. Chou "Effect of NH₄F concentration in electrolyte on the fabrication of TiO₂ nanotube arrays prepared by anodization" *Micro Nano Lett.* 7 (2012) 939.

44. K. Shankar, G. K. Mor, H. E. Prakasam, S. Yoriya, M. Paulose, O. K. Varghese, C. A. Grimes "Highly-ordered TiO₂ nanotube arrays up to 220 μ m in length: use in water photoelectrolysis and dye-sensitized solar cells" *Nanotechnology* 18 (2007) 065707.
45. P. Roy, S. Berger, P. Schmuki "TiO₂ Nanotubes: Synthesis and Applications" *Angew. Chem. Int. Ed.* 50 (2011) 2904.
46. Z. Su, W. Zhou "Formation, morphology control and applications of anodic TiO₂ nanotube arrays" *J. Mater. Chem.* 21 (2011) 8955.
47. J.M. Macak, H. Tsuchiya, A. Ghicov, K. Yasuda, R. Hahn, S. Bauer, P. Schmuki "TiO₂ nanotubes: Self-organized electrochemical formation, properties and applications" *Curr. Opin. Solid St. M.* 11 (2007) 3.
48. J. M. Macak, H. Hildebrand, U. Marten-Jahns, P. Schmuki "Mechanistic aspects and growth of large diameter self-organized TiO₂ nanotubes" *J. Electroanal. Chem.* 621 (2008) 254.
49. G. K. Mor, O. K. Varghese, M. Paulose, K. Shankar, C. A. Grimes "A review on highly ordered, vertically oriented TiO₂ nanotube arrays: Fabrication, material properties, and solar energy applications" *Sol. Energ. Mat. Sol. C.* 90 (2006) 2011.
50. S. Berger, S. P. Albu, F. Schmidt-Stein, H. Hildebrand, P. Schmuki, J. S. Hammond, D. F. Paul, S. Reichlmaier "The origin for tubular growth of TiO₂ nanotubes: A fluoride rich layer between tube-walls" *Surf. Sci.* 605 (2011) L57.
51. K-L. Li, Z-B. Xie, S. Adams "A reliable TiO₂ nanotube membrane transfer method and its application in photovoltaic devices" *Electrochim. Acta* 62 (2012) 116.
52. D. Fanga, Z. Luob, K. Huanga, D. C. Lagoudas "Effect of heat treatment on morphology, crystalline structure and photocatalysis properties of TiO₂ nanotubes on Ti substrate and freestanding membrane" *J. Electroanal. Chem.* 637 (2009) 6.
53. Y. Liao, W. Que, P. Zhong, J. Zhang, Y. He "A facile method to crystallize amorphous anodized TiO₂ nanotubes at low temperature" *ACS Appl. Mater. Interfaces* 3 (2011) 2800.

54. Dyesol. Available at: www.dyesol.com
55. H. J. Snaith "Estimating the Maximum Attainable Efficiency in Dye-Sensitized Solar Cells" *Adv. Funct. Mater.* 20 (2010) 13.
56. EIA. Available at: www.eia.gov
57. N. Alexaki, T. Stergiopoulos, A. G. Kontos, D. S. Tsoukleris, A. P. Katsoulidis, P. J. Pomonis, D. J. LeClere, P. Skeldon, G. E. Thompson, P. Falaras "Mesoporous titania nanocrystals prepared using hexadecylamine surfactant template: Crystallization progress monitoring, morphological characterization and application in dye-sensitized solar cells" *Micropor. Mesopor. Mater.* 124 (2009) 52.
58. G. C. Vougioukalakis, A. I. Philippopoulos, T. Stergiopoulos, P. Falaras "Contributions to the development of ruthenium-based sensitizers for dye-sensitized solar cells" *Coordin. Chem. Rev.* 255 (2011) 2602.
59. T. Stergiopoulos, P. Falaras "Minimizing Energy Losses in Dye-Sensitized Solar Cells Using Coordination Compounds as Alternative Redox Mediators Coupled with Appropriate Organic Dyes" *Adv. Energy Mater.* 2 (2012) 616.
60. A. V. Katsanaki, H. S. Karayianni, M-C. Bernard, D. S. Tsoukleris, P. Falaras "Preparation and Characterization of Nanocrystalline Pt/TCG Counterelectrodes for Dye-Sensitized Solar Cells" *J. Sol. Energy Eng.* 130 (2008) 041008.
61. M. Grätzel "Photoelectrochemical cells" *Nature* 414 (2001) 338.
62. L. Peter "'Sticky Electrons' Transport and Interfacial Transfer of Electrons in the Dye-Sensitized Solar Cell" *Acc. Chem. Res.* 42 (2009)1839.
63. K. Park, Q. Zhang, D. Myers, G. Cao "Charge transport properties in TiO₂ network with different particle sizes for DSCs" *ACS Appl. Mater. Interfaces* 5 (2013) 1044.
64. T. Stergiopoulos "Spectroscopic Characterization of Photoelectrochemical solar Cells" PhD Thesis University of Patras 2006.

65. G. Boschloo, A. Hagfeldt "Characteristics of the Iodide/Triiodide Redox Mediator in Dye-Sensitized Solar Cells" *Acc. Chem. Res.* 42 (2009) 1819.
66. A. J. Frank, N. Kopidakis, J. V. D. Lagemaat "Electrons in nanostructured TiO₂ solar cells: transport, recombination and photovoltaic properties" *Coordin. Chem. Rev.* 248 (2004) 1165.
67. A. Hagfeldt, G. Boschloo, L. Sun, L. Kloo, H. Pettersson "Dye-Sensitized Solar Cells" *Chem. Rev.* 110 (2010) 6595.
68. M. Grätzel "Dye-sensitized solar cells" *J. Photochem. Photobiol. C* 4 (2003) 145.
69. M. Grätzel "Recent Advances in Sensitized Mesoscopic Solar Cells" *Acc. Chem. Res.* 42 (2009) 1788.
70. F. O. Lenzmann, J.M. Kroon Recent Advances in Dye-Sensitized Solar Cells *Adv. Optoelectron.* 2007 (2007).
71. Photovoltaic Education. Available at: www.pveducation.org
72. M. A. Omar "Elementary Solid State Physics" Book Addison-Wesley 1975.
73. H-G. Yun, B-S. Bae, M. G. Kang "A Simple and Highly Efficient Method for Surface Treatment of Ti Substrates for Use in Dye-Sensitized Solar Cells" *Adv. Energy Mater.* 1 (2011) 305.
74. J. M. Kroon, N. J. Bakker, H. J. P. Smit, P. Liska, K. R. Thampi, P. Wang, S. M. Zakeeruddin, M. Gratzel, A. Hinsch, S. Hore, U. Wurfel, R. Sastrawan, J. R. Durrant, E. Palomares, H. Pettersson, T. Gruszecki, J. Walter, K. Skupien, G. E. Tulloch "Nanocrystalline Dye-sensitized Solar Cells Having Maximum Performance" *Prog. Photovolt: Res. Appl.* 15 (2007) 1.
75. T-Y. Tsai, C-M. Chen, S-J. Cherng, S.-Y. Suen "An efficient titanium-based photoanode for dye-sensitized solar cell under back-side illumination" *Prog. Photovolt: Res. Appl.* 21 (2013) 226.
76. S. Ito, N-L. C. Ha, G. Rothenberger, P. Liska, P. Comte, S. M. Zakeeruddin, P. Pechy, M. K. Nazeeruddin, M. Gratzel "High-efficiency

- (7.2%) flexible dye-sensitized solar cells with Ti-metal substrate for nanocrystalline-TiO₂” photoanode Chem. Commun. (2006) 4004.
77. J. An, W. Guo, T. Ma “Enhanced Photoconversion Efficiency of All-Flexible Dye-Sensitized Solar Cells Based on a Ti Substrate with TiO₂ Nanoforest Underlayer” Small 8 (2012) 3427.
78. P. Roy, S. P. Albu, P. Schmuki “TiO₂ nanotubes in dye-sensitized solar cells: Higher efficiencies by well-defined tube tops” Electrochem. Commun. 12 (2010) 949.
79. L-L. Li, C.-Y. Tsai, H-P. Wu, C-C. Chen, E. W-G. Diao “Fabrication of long TiO₂ nanotube arrays in a short time using a hybrid anodic method for highly efficient dye-sensitized solar cells” J. Mater. Chem. 20 (2010) 2753.
80. N. Mir, K. Lee, I. Paramasivam, P. Schmuki “Optimizing TiO₂ Nanotube Top Geometry for Use in Dye-Sensitized Solar Cells” Chem. Europ. J. 18 (2012) 11862.
81. J. Wang, Z. Lin “Dye-Sensitized TiO₂ Nanotube Solar Cells with Markedly Enhanced Performance via Rational Surface Engineering” Chem. Mater. 22 (2010) 579.
82. M. Ye, X. Xin, C. Lin, Z. Lin “High Efficiency Dye-Sensitized Solar Cells Based on Hierarchically Structured Nanotubes” Nan Lett. 11 (2011) 3214.
83. J. Y. Kim, J. H. Noh, K. Zhu, A. F. Halverson, N. R. Neale, S. Park, K. S. Hong, A. J. Frank “General Strategy for Fabricating Transparent TiO₂ Nanotube Arrays for Dye-Sensitized Photoelectrodes: Illumination Geometry and Transport Properties” ACS Nano 5 (2011) 2647.
84. P. Roy, D. Kim, K. Lee, E. Spiecker, P. Schmuki “TiO₂ nanotubes and their application in dye-sensitized solar cells” Nanoscale 2 (2010) 45.
85. K. Zhu, N. R. Neale, A. Miedaner, A. J. Frank “Enhanced Charge-Collection Efficiencies and Light Scattering in Dye-Sensitized Solar Cells Using Oriented TiO₂ Nanotubes Arrays” Nano Lett. 7 (2007) 69.

86. M. Yutao, L. Yuan, X. Xurui, L. Xueping, Z. Xiaowen "Synthesis of TiO₂ nanotubes film and its light scattering property" Chin. Sci. Bull. 50 (2005) 1985.
87. R. Mohammadpour, A. Irajizad, A. Hagfeldt, G. Boschloo "Comparison of Trap-state Distribution and Carrier Transport in Nanotubular and Nanoparticulate TiO₂ Electrodes for Dye-Sensitized Solar Cells" Chem. Phys. Chem. 11 (2010) 2140.
88. C. Richter, C. A. Schmuttenmaer "Exciton-like trap states limit electron mobility in TiO₂ nanotubes" Nat. Nanotechnol. 5 (2010) 769.
89. J. Bisquert, F. Fabregat-Santiago, I. Mora-Sero, G. Garcia-Belmonte, S. Gimenez "Electron Lifetime in Dye-Sensitized Solar Cells: Theory and Interpretation of Measurements" J. Phys. Chem. C 113 (2009) 17278.
90. J. R. Jennings, A. Ghicov, L. M. Peter, P. Schmuki, A. B. Walker "Dye-Sensitized Solar Cells Based on Oriented TiO₂ Nanotube Arrays: Transport, Trapping, and Transfer of Electrons" J. Am. Chem. Soc. 130 (2008) 13364.
91. J. P. Gonzalez-Vazquez, V. Morales-Flórez, J. A. Anta "How Important is Working with an Ordered Electrode to Improve the Charge Collection Efficiency in Nanostructured Solar Cells?" J. Phys. Chem. Lett. 3 (2012) 386.
92. A. Ghicov, S. P. Albu, R. Hahn, D. Kim, T. Stergiopoulos, J. Kunze, C-A. Schiller, P. Falaras, P. Schmuki "TiO₂ Nanotubes in Dye-Sensitized Solar Cells: Critical Factors for the Conversion Efficiency" Chem. Asian J. 4 (2009) 520.
93. L. Sun, S. Zhang, X. Sun, X. He "Effect of the Geometry of the Anodized Titania Nanotube Array on the Performance of Dye-Sensitized Solar Cells" J. Nanosci. Nanotechnol. 10 (2010) 4551.
94. P. Zhong, W. Que, Y. Liao, J. Zhang, X. Hu "Improved performance in dye-sensitized solar cells by rationally tailoring anodic TiO₂ nanotube length" J. Alloys Compd. 540 (2012) 159.
95. C-C. Chen, H.-W. Chung, C-H. Chen, H-P. Lu, C-M. Lan, S-F. Chen, L. Luo, C-S. Hung, E. W-G. Diau "Fabrication and

Characterization of Anodic Titanium Oxide Nanotube Arrays of Controlled Length for Highly Efficient Dye-Sensitized Solar Cells” J. Phys. Chem. C 112 (2008) 19151.

96. N. Liu, K. Lee, P. Schmuki “Small Diameter TiO₂ Nanotubes vs. Nanopores in Dye Sensitized Solar Cells” Electrochem. Commun. 15 (2012) 1.

97. P. Roy, S. P. Albu, P. Schmuki “TiO₂ nanotubes in dye-sensitized solar cells: Higher efficiencies by well-defined tube tops” Electrochem. Commun. 12 (2010) 949.

98. S. P. Albu, H. Tsuchiya, S. Fujimoto, P. Schmuki “TiO₂ Nanotubes – Annealing Effects on Detailed Morphology and Structure” Eur. J. Inorg. Chem. 2010 (2010) 4351.

99. K. Zhu, N. R. Neale, A. F. Halverson, J. Y. Kim, A. J. Frank “Effects of Annealing Temperature on the Charge-Collection and Light-Harvesting Properties of TiO₂ Nanotube-Based Dye-Sensitized Solar Cells” J. Phys. Chem. C 114 (2010) 13433.

100. I. J. Macak “Growth of Anodic Self-Organized Titanium Dioxide Nanotube Layers” PhD Thesis University of Erlangen-Nuremberg 2008.

101. S. P. Albu “Morphology and Growth of Titania Nanotubes. Nanostructuring and Applications” PhD Thesis University of Erlangen-Nuremberg 2012.

102. Y. R. Smith, R. S. Ray, K. Carlson, B. Sarma, M. Misra “Self-Ordered Titanium Dioxide Nanotube Arrays: Anodic Synthesis and Their Photo/Electro-Catalytic Applications” Materials 6 (2013) 2892.

Chapter 3. Sensitizer activated solar cells based on self-organized TiO₂ nanotubes

This chapter reports the preparation of NTs under low applied voltage (30 V) in NH₄F/ethylene glycol electrolytes containing a slight amount of water. An investigation of the effects of polishing the Ti foils (before anodization) and the removal of the nanograss (structural disorder created at the top surface of the NTs due to the prolonged exposure of the tubes inside the F⁻ rich environment) on the nanotubular films properties. After optimization of the anodization conditions, homogeneous anodic films consisting of smooth and long NTs are prepared, which, when incorporated as photoelectrodes in dye-sensitized solar cells, present overall power conversion efficiencies of about 3 % under backside illumination conditions.

3.1. Introduction

Particular emphasis has recently been given on anodic TiO₂ nanotubes (NTs) [1,2]. Upon controlling the conditions of electrochemical oxidation, vertically oriented NT arrays with high aspect ratios have been grown [3,4], attaining very promising efficiencies up to 7-7.3 %, when utilized as photoelectrode in DSCs [5,6]. However, the above efficiencies were achieved for NTs prepared at large potentials (50-60 V), imposing an extremely high electric field at the electrode/electrolyte interface, especially at the first stages of the anodization. This causes serious problems that may affect the morphology and adherence of these films, especially after thermal annealing at temperatures above 450 °C.

On the other hand, the growth of high aspect ratio TiO₂ NTs under relatively low (<40 V) anodization potentials has received less

attention [7-9]. In that case, use of anhydrous ethylene glycol (EG) electrolyte was reported to result in the formation of 12 μm NTs at 30 V [7], while addition of small amounts of water yielded 5 μm NTs leading to an overall DSC efficiency of 2.8 % [8]. Moreover, 14 μm NTs were prepared by anodization at 35 V and the performance of the DSCs was improved to $\eta=3.3$ % after post treatment with TiCl_4 [9].

In this chapter, is communicated the growth of long, homogeneous TiO_2 NTs arrays by applying a low anodization potential of + 30 V (vs. Pt) in $\text{NH}_4\text{F}/\text{EG}$ electrolytes containing a slight amount of water. The (polishing) effects of pre-treatment of the substrates for anodization (Ti-foils) together with those of a post-treatment procedure of the anodic films in order to remove structural disorder (nanograss) from the NTs surface are investigated. Finally, optimum pre and post-treatment leads to nanotubular titania photoelectrodes, which attain a relatively high overall photovoltaic efficiency of about 3 %.

3.2. Experimental

3.2.1 Pre-treatment of Ti foils

For some experiments, prior to the anodization process, Ti foils (0.25 mm, 99.7 % purity, Sigma Aldrich) were polished with sandpaper (No 1200) and then with diamond paste (6 μm). Their morphology was characterized using a PHILIPS Quanta Inspect scanning electron microscope (SEM) and a Digital Instruments Nanoscope III atomic force microscope (AFM).

3.2.2. Anodization conditions and post-treatment for the anodic films

Anodization was carried out by applying +30 V (vs. a Pt mesh) using an Autolab PGSTAT-30 potentiostat (Ecochemie) for a period of 16 h. The electrolyte solution consisted of 0.45 wt % of anhydrous NH_4F (95 %, Janssen Chimica) in ethylene glycol (99.5%, Panreac) and a small amount of DI water (1 vol %). After anodization, the “nanograss”, appearing at the surface of the tubes, was removed by immersing the samples in EtOH for 24 h and then soaking them in ultrasounds for 15 min. Furthermore, the anodic samples were subsequently annealed at 450 °C for 60 minutes (heating rate of 5 °C min^{-1}) [10].

3.2.3. Cell assembly and measurements

After annealing, the TiO_2 NTs films were immersed in N719 dye (Dyesol Ltd.) solution for 3 days. DSCs were constructed by placing a drop of a liquid electrolyte onto the photoelectrode and sandwiching against a Pt counter electrode (CE). I-V characteristics were obtained through linear sweep voltammetry by illuminating the DSCs from the transparent CE side, using solar simulated light (1 sun, 1000 W m^{-2}) from a 300W-Xe source operating in combination with AM 1.5G and UV cut-off optical filters (Oriel).

3.3. Results and discussion

3.3.1 Pre-treatment effects

In literature, there are no specific data concerning the effects of polishing the metal foils on the anodization process. In order to investigate such effects, the Ti foils were polished with standard procedures. The SEM image **Figure 3-1** (a) shows the original rough surface of the Ti metal endowed with deep cracks, while after

polishing, it converts into a relatively smooth and flat surface, where only some features remain with negligible depth **Figure 3-1** (b). Likewise, the top-view AFM 3D images obtained under similar magnification **Figure 3-1** (c) and (d) proved that the untreated samples present a greater roughness (25 nm) in comparison with the polished foils (5 nm), in perfect agreement with the SEM images.

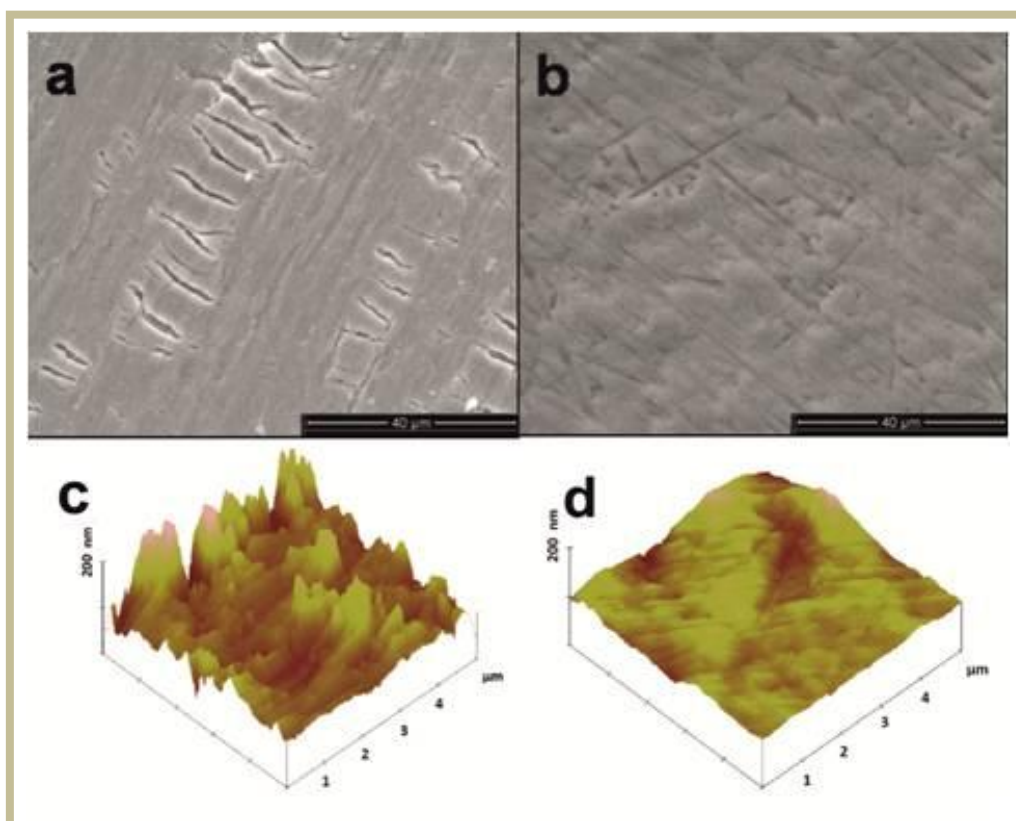


Figure 3-1. SEM and AFM images of Ti foils before (a, c) and after polishing (b, d), respectively.

3.3.2 Anodization

Regardless of the Ti foil pre-treatment, the anodized samples do not present any significant variation on their final structure and morphology. Thus, **Figure 3-2** (a) depicts a characteristic SEM image for the top surface of the NTs after anodization of a polished Ti foil, showing that the top of the NTs is covered by “nanograss”. This is due to the prolonged anodization time, where tubes are collapsed or

bundled as a consequence of the etching by the corrosive electrolyte [11]. Additionally, looking at the cross-section of the anodic films **Figure 3-2** (b), we can determine the thickness of the NTs, being in the order of 15-18 μm . It is also important to notice that no ribs or defects are evident at the surface of the NT walls, due to the low water content in the electrolyte [12].

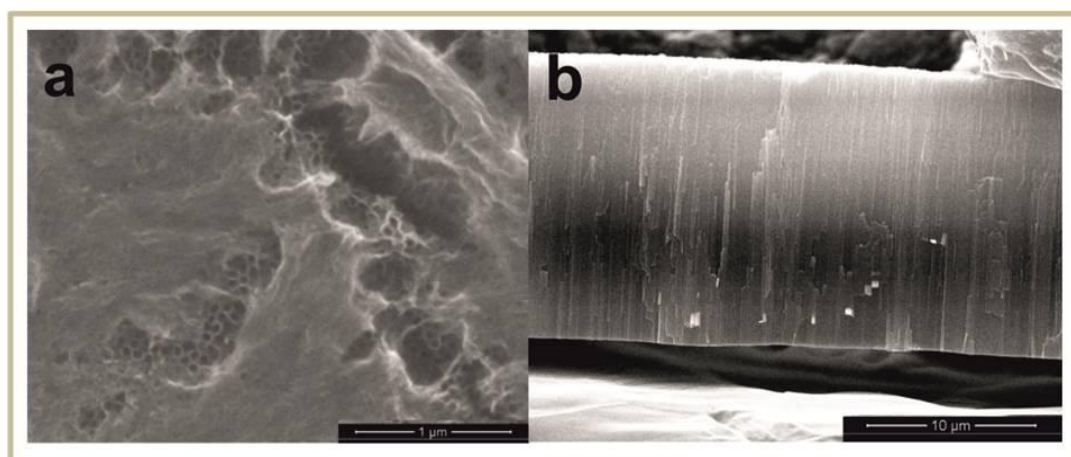


Figure 3-2. SEM top images of the grassy surface of the NTs (a) along with cross section images of the tubes after anodization of polished samples (b). Note that similar images were obtained for the unpolished samples.

3.3.3. Post-treatment effects

Owing to the “nanograss” covering most of sample surface, we were not able to clearly visualize the NTs. To this end, the next step was to remove the “nanograss” [13-17] by immersing and sonicating the anodic films in ethanol. **Figure 3-3** (a) illustrates the top surface of the tubes after extensive removal of the grass, where now, in contradiction to **Figure 3-2** (a), the tubes are clearly visible. The morphological characteristics parameters of the NTs can then be readily distinguished at higher magnification images, as shown in **Figure 3-3** (b), where an internal NT pore diameter of 60 nm and a wall thickness of 15 nm are determined. On the other hand, inspection of at the lower part of the NTs **Figure 3-3** (c), reveals that a smaller pore diameter (30 nm) and a larger wall thickness (45 nm)

exist at the bottom of the tubes. This implies that the tubes are self-assembled at the foil under an asymmetric morphology, most probably due to the larger etching rate by the corrosive electrolyte at regions, where the electrolyte is in close contact with the NTs. Additionally, by mechanically bending the samples, separated nanotube arrays were obtained and their closed bottoms are shown in **Figure 3-3** (d).

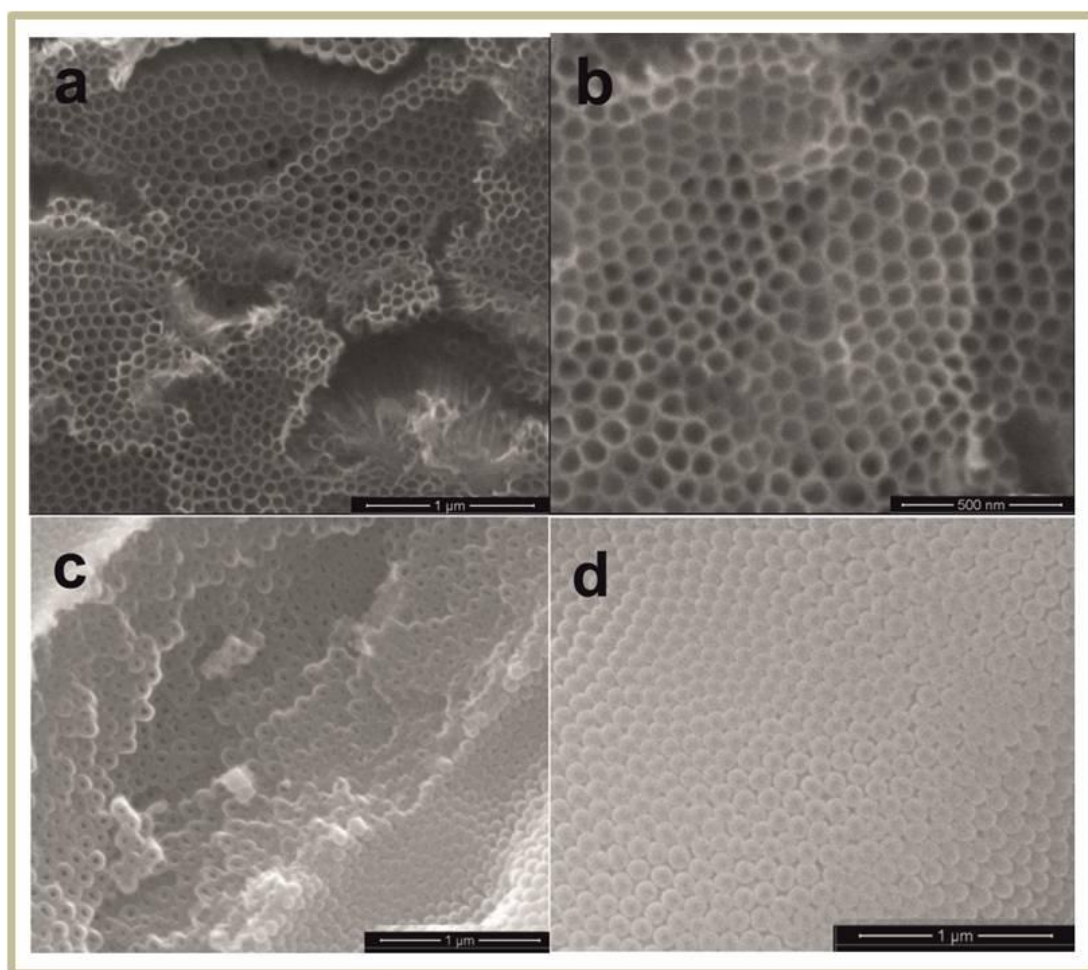


Figure 3-3. SEM top images of NTs after removal of nanograss (a) and under higher magnification (b). Top images of the lower part of the tubes, revealing the greater NT diameter present at the bottom of the NTs (c) and the presence of the barrier layer (d).

3.3.4. Incorporation into solar cells

Post-thermal treatment was subsequently applied in order to convert the as-grown NTs from the amorphous to the anatase phase (confirmed by micro-Raman spectroscopy, not shown). To evaluate the photovoltaic performance of the NTs sensitized by the N719 dye, DSCs were constructed and the I-V curves of the cells were recorded **Figure 3-4**. Deriving all the electrical parameters from the I-V analysis, it was found that the raw NTs (without pre and post-treatment) present the lowest efficiency, of the order of 2.64 % (with J_{sc} = 6.63 mA/cm², V_{oc} = 740 mV, FF= 0.53). When the foils were polished and then subjected to anodization, the photocurrent (J_{sc}) was slightly decreased (6.36 mA/cm²) but the synergistic increase of photopotential (V_{oc} =783 mV) and filling factor (FF=0.54) kept the efficiency relatively constant (η =2.70 %). On the contrary, combining the pre and post-treatments (removal of “nanograss”), we were able to largely increase the obtained J_{sc} (7.87 mA/cm²) and then boost the efficiency up to 2.94 % despite the lower V_{oc} (763 mV) and FF (0.49). The above result seems very reasonable, since it is anticipated that the presence of nanograss may lead to carriers recombination at the interface between the grass and the NTs thus, a clean top can fully take advantage from the vectorial transport along the nanotube axis.

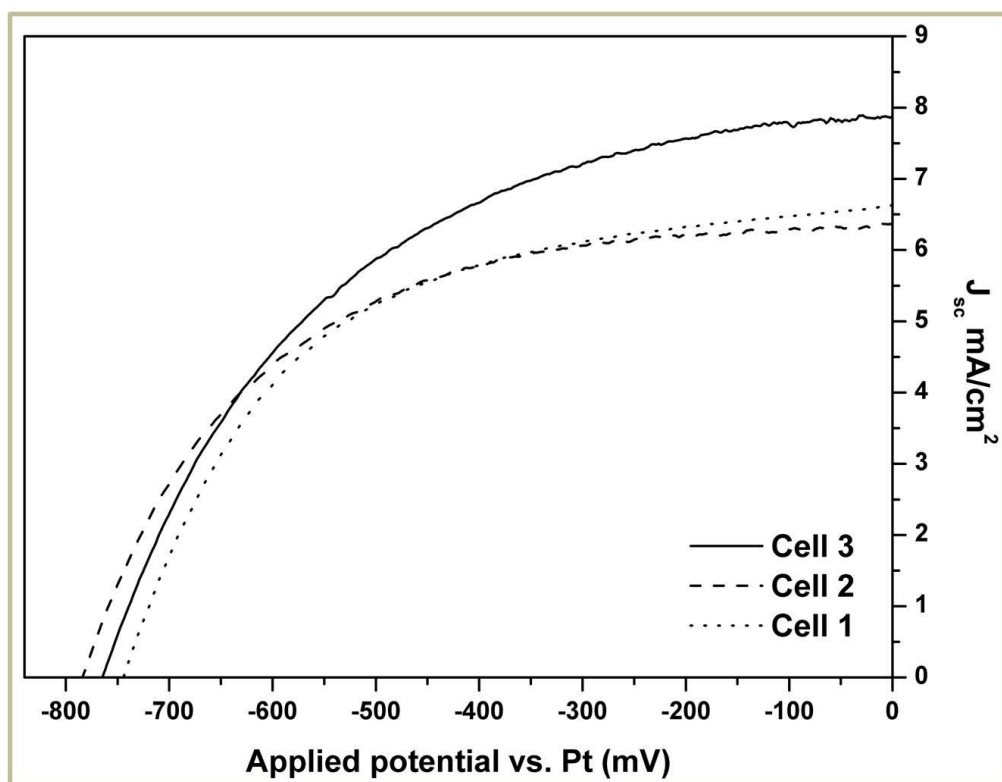


Figure 3-4. Current-voltage (I-V) characteristics of the DSCs based on NTs electrodes (cell 1-3), obtained under 1 sun (AM 1.5G) illumination; Cell 1 is constructed with raw NTs, cell 2 contains anodic films prepared on a polished substrate and cell 3 refers to a DSC with NTs grown on a polished foil and after removal of “nanograss”.

3.4. Conclusions

TiO₂ NTs of high quality have been prepared at a low anodization voltage (+ 30 V vs. Pt) in NH₄F/EG electrolytes containing a slight amount of water. The Ti foils were subjected to polishing before anodization. However, the slight differences observed on the roughness of their surface do not seem to affect the anodization process and consequently the structure and morphology of the as-prepared NTs. Thus, both (pre-treated or not) anodic films were as thick as 15-18 μm, with smooth walls and a large net of “nanograss” covering the surface of the tubes. When these samples were sonicated in ethanol, the grass was substantially removed and the underneath NTs appeared having a pore diameter of 60 nm and a wall thickness of 15 nm, gradually changing to 30 and 45 nm, correspondingly towards

the bottom of the NTs. The NTs were used as photoanodes in DSCs, where the raw and pretreated materials have shown an efficiency of about 2.7 %, although the removal of nanograss boosted the efficiency up to about 3 %.

3.5. References

1. Hagfeldt, G. Boschloo, L. Sun, L. Kloo, H. Pettersson "Dye-Sensitized Solar Cells" *Chem. Rev.* 110 (2010) 6595.
2. P. Roy, D. Kim, K. Lee, E. Spiecker, P. Schmuki "TiO₂ nanotubes and their application in dye-sensitized solar cells" *Nanoscale* 2 (2010) 45.
3. T. Stergiopoulos, A. Ghicov, V. Likodimos, D. S. Tsoukleris, J. Kunze, P. Schmuki, P. Falaras "Dye-sensitized solar cells based on thick highly ordered TiO₂ nanotubes produced by controlled anodic oxidation in non-aqueous electrolytic media" *Nanotechnology* 19 (2008) 235602.
4. A. Ghicov, S. P. Albu, R. Hahn, D. Kim, T. Stergiopoulos, J. Kunze, C. A. Schiller, P. Falaras, P. Schmuki "TiO₂ nanotubes in dye-sensitized solar cells: critical factors for the conversion efficiency" *Chem. Asian J.* 4 (2009) 520.
5. C. C. Chen, H. W. Chung, C. H. Chen, H. P. Lu, C. M. Lan, S. F. Chen, L. Luo, C. S. Hung, E. W. G. Diau "Fabrication and Characterization of Anodic Titanium Oxide Nanotube Arrays of Controlled Length for Highly Efficient Dye-Sensitized Solar Cells" *J. Phys. Chem. C* 112 (2008) 19151.
6. J. Wang, Z. Lin "Dye-Sensitized TiO₂ Nanotube Solar Cells with Markedly Enhanced Performance via Rational Surface Engineering" *Chem. Mater.* 22 (2010) 579.
7. Y. Y. Song, R. Lynch, D. Kim, P. Roy, P. Schmuki "TiO₂ Nanotubes: Efficient Suppression of Top Etching during Anodic Growth Key to

- Improved High Aspect Ratio Geometries” *Electrochem. Solid-state Lett.* 12 (2009) C17.
8. C. T. Yip, C. S. K. Mak, A. B. Djurisic, Y. F. Hsu, W. K. Chan “Dye-sensitized solar cells based on TiO₂ nanotube/porous layer mixed morphology” *Appl. Phys. A* 92 (2008) 589.
9. D. Kuang, J. Brillet, P. Chen, M. Takara, S. Uchida, H. Miura, K. Sumioka, S. M. Zakeerudin, M. Gratzel “Application of Highly Ordered TiO₂ Nanotube Arrays in Flexible Dye-Sensitized Solar Cells” *ACS Nano* 2 (2008) 1113.
10. T. Stergiopoulos, A. Valota, V. Likodimos, Th. Speliotis, D. Niarchos, P. Skeldon, G. E. Thompson, P. Falaras “Dye-sensitization of self-assembled titania nanotubes prepared by galvanostatic anodization of Ti sputtered on conductive glass” *Nanotechnology* 20 (2009) 365601.
11. K. Yasuda, J. M. Macak, S. Berger, A. Ghicov, P. Schmuki “Mechanistic Aspects of the Self-Organization Process for Oxide Nanotube Formation on Valve Metals” *J. Electrochem. Soc.* 154 (2007) C472.
12. P. Roy, S. A. Albu, P. Schmuki “TiO₂ nanotubes in dye-sensitized solar cells: Higher efficiencies by well-defined tube tops” *Electrochem. Comm.* 12 (2010) 949.
13. D. Kim, A. Ghicov, P. Schmuki “TiO₂ Nanotube arrays: Elimination of disordered top layers (“nanograss”) for improved photoconversion efficiency in dye-sensitized solar cells” *Electrochem. Commun.* 10 (2008) 1835.
14. K. Zhu, T. B. Vinzant, N. R. Neale, A. J. Frank “Removing Structural Disorder from Oriented TiO₂ Nanotube Arrays: Reducing the Dimensionality of Transport and Recombination in Dye-Sensitized Solar Cells” *Nano Lett.* 7 (2007) 3739.
15. C. C. Chen, W. D. Jehgn, L. L. Li, E. D. G. Diao “Enhanced Efficiency of Dye-Sensitized Solar Cells Using Anodic Titanium Oxide Nanotube Arrays” *J. Electrochem. Soc.* 156 (2009) C304.

16. S. P. Albu, P. Schmuki "TiO₂ nanotubes grown in different organic electrolytes: Two-size self-organization, single vs. double-walled tubes, and giant diameters" Phys. Status Solidi - R 4 (2010) 151.
17. G. Zhang, H. Huang, Y. Zhang, H. L. W. Chan, L. Zhou "Highly ordered nanoporous TiO₂ and its photocatalytic properties" Electrochem. Commun. 9 (2007) 2854.

Chapter 4. Annealing effects on self-assembled TiO₂ nanotubes and their behaviour as photoelectrodes in dye-sensitized solar cells

Self-assembled highly ordered TiO₂ nanotube arrays were grown on Ti foils in a NH₄F ethylene glycol electrolyte under mild anodic oxidation conditions. The effect of annealing post-treatment on their structural properties was systematically investigated with respect to their electrical characteristics and photoelectrochemical performance in back-side illuminated dye-sensitized solar cells (DSCs). A variety of parameters were controlled and optimized including the annealing temperature, the heating rate and duration of the thermal treatment. The obtained results confirmed a correlation between the crystalline/structural properties of the TiO₂ nanotubes and their electrical characteristics, thus revealing the close interplay of crystal size, grain boundaries and crystallite interconnectivity with the electron dynamics (transport/recombination) governing the DSC operation and efficiency. The high importance of a barrier layer at the interface between the nanotubes and the Ti foil was also highlighted.

4.1. Introduction

During the last years, self-assembled nanotubular TiO₂ arrays grown by controlled electrochemical anodization have emerged as a versatile, vertically oriented architecture that is being actively investigated for various applications [1] and especially in dye-sensitized solar cells (DSCs) [2]. It is clear that the electrode surface morphology, crystallinity and thickness are the critical parameters that determine the efficiency and performance of the TiO₂ NT photoelectrodes in DSCs.

Proper control of the potentiostatic anodization parameters, including solution chemistry, applied potential and anodization time, can enable tailoring of the tube structure, diameter, length and wall thickness [3-10]. The most appropriate crystal phase of titania for DSC applications is anatase, presenting better electrical properties in comparison to the other TiO_2 polymorphic phases of rutile and brookite [11]. As-grown titania NTs prepared by anodic oxidation are amorphous, thus their conversion into anatase, that is usually achieved with thermal annealing in air, is necessary. Usually, NTs fully crystallize into anatase at 400 °C, while rutile traces begin to appear at 600 °C [12,13]; beyond 600 °C, the tubes' morphology collapses. Annealing effects on NTs for DSCs were studied in detail only by the group of Frank et al. [14]; however these authors have used very thin tubes (2 μm) as model NTs, which are far from being classified as optimum photoelectrodes for back-side illuminated liquid DSCs [15,16].

In this chapter, it has been performed a systematic investigation of annealing effects on the morphology, structure and crystallinity of TiO_2 NTs and their correlation with their performance and electrical characteristics as photoelectrodes in back-side illuminated DSCs including conversion efficiencies, electron transport and recombination, and interfacial resistance. As a model substrate, sufficiently long (16 μm), homogeneous TiO_2 NTs arrays prepared at relatively low anodization potentials (+ 30 V vs. a Pt electrode) were chosen, imposing a moderate electric field at the working electrode/electrolyte interface, during the first stages of the anodization. This prevents typical breakdown problems that affect the morphology and the adherence of the NTs on the Ti substrate, especially after thermal annealing at temperatures above 450 °C. The effect of the annealing temperature, the heating rate and the total duration of the annealing procedure on the structural properties of the TiO_2 NTs and the electron dynamics (transport/recombination)

governing the corresponding DSC operation could be effectively accessed.

4.2. Experimental

4.2.1. TNTs preparation

Ti foils (0.25 mm, 99.7 % purity, Sigma Aldrich), used as substrates for the anodization experiments, were ultrasonicated in acetone, isopropanol and methanol for 10 min and then dried in nitrogen stream. Anodization was carried out in a Teflon electrochemical cell by applying a voltage of +30 V between the anode (Ti foil) and the cathode (Pt mesh) using an Autolab PGSTAT-30 potentiostat (Ecochemie) for 16 h. The electrolyte solution consisted of 0.45 wt % NH_4F (95 %, Janssen Chimica) in ethylene glycol (99.5%, Panreac) and a small amount of de-ionized (DI) water (1 vol %) [17]. The anodized samples were subsequently annealed in air at different temperatures in the range from 400 to 600 °C (step 50 °C), by varying systematically the heating rate from 1 up to 10 °C min⁻¹ and the duration of the annealing from 1 to 6 h.

4.2.2. TNTs and DSCs characterization

The morphology of the crystalline samples was characterized using a PHILIPS Quanta Inspect scanning electron microscope (SEM). The structural properties of the TNTs were characterized by Raman spectroscopy (InVia Renishaw Raman spectrometer) using an Ar⁺ ion laser ($\lambda=514.5$ nm) as excitation source.

After annealing, the TiO₂ NTs films were immersed in N719 dye (Dyesol Ltd.) solution for 1 day. The dye loading was examined by dye desorption experiments in a solution 1/ 1 EtOH/ H₂O with 0.2 M

NaOH. DSCs were constructed by placing a drop of a standard liquid electrolyte with a low iodine content (1 M propyl-methylimidazolium iodide, 0.05 M LiI, 0.015 M I₂, 0.5 M tert-butylpyridine, 0.1 M guanidinium thiocyanate in acetonitrile/valeronitrile) onto the photoelectrode and sandwiching against a highly transparent Pt counter electrode (fabricated by sputtering). J-V characteristics were obtained through linear sweep voltammetry by illuminating the DSCs from the transparent cathode, using solar simulated light (1 sun, AM1.5G, 1000 W m⁻²) from a 300W-Xe source (Oriel). Electrochemical impedance spectra (EIS) were recorded on these cells using the same potentiostat, equipped with a frequency response analyzer (FRA), at V_{oc}, under 1 sun illumination over a frequency range of 100 kHz to 10 mHz. Transport time constants (τ_{trans}) were determined by Intensity Modulated Photocurrent Spectroscopy (IMPS), using the same system (Autolab and FRA). A red light (max at 625 nm) emitting diode was used as the light source for both AC and DC illumination controlled by the FRA module.

4.3. Results

4.3.1. Morphology-structure of the as-grown TiO₂ nanotubes

Three different sets of annealing treatments were conducted: in the first one, hereafter referred as set 1, the annealing temperature was increased, with a step of 50 °C, from 400 to 600 °C, while the annealing time and the heating rate were kept constant at 1 h and 5 °C/min respectively. In the second set (set 2), we kept the annealing temperature (400 °C) and the duration of annealing (1 h) constant and varied the heating rate at 1, 2, 5 and 10 °C/min. Finally (set 3), the annealing temperature and the heating rate were fixed at 400 °C and 5 °C/min, respectively, and the duration of annealing was varied between 1, 2, 3 and 6 h.

Independently of the different annealing conditions, all sets of TiO₂ NT arrays exhibited a similar tubular morphology, in agreement with previous reports [14]. Representative top SEM images of NTs from set 1 **Figure 4-1** (a), showed a clean surface consisting of well separated and regularly arranged tubes (the internal NT diameter was about 60 nm and the wall thickness around 15 nm). Cross-sectional SEM images **Figure 4-1** (b) demonstrated the high degree of vertical orientation of the TiO₂ NT arrays, permitting to estimate the tube length to be ~15 µm, after 16 h of anodization. Moreover, the NT walls were rather smooth with no significant portion of ribs due to the minimum amount of water content in the electrolyte bath (inset of **Figure 4-1** (b)) [18]. At the bottom, the NTs are closed **Figure 4-1** (c), while in the case when the tube caps were removed, the wall thickness near the bottom was found to be three times greater (45 nm) than that at the top, confirming the U-shape of the NTs (inset of **Figure 4-1** (c)) [19]. In **Figure 4-1** (d), a characteristic cross-section image of NTs annealed at 600 °C is presented, where a thick barrier layer of 200 nm was clearly observed between the tubes and the substrate. This layer assures the adherence of the NTs on the Ti foil [1]. The thickness of this barrier layer depends on the annealing conditions [20] however; the identification of this layer is not plausible in cases where it is quite thin.

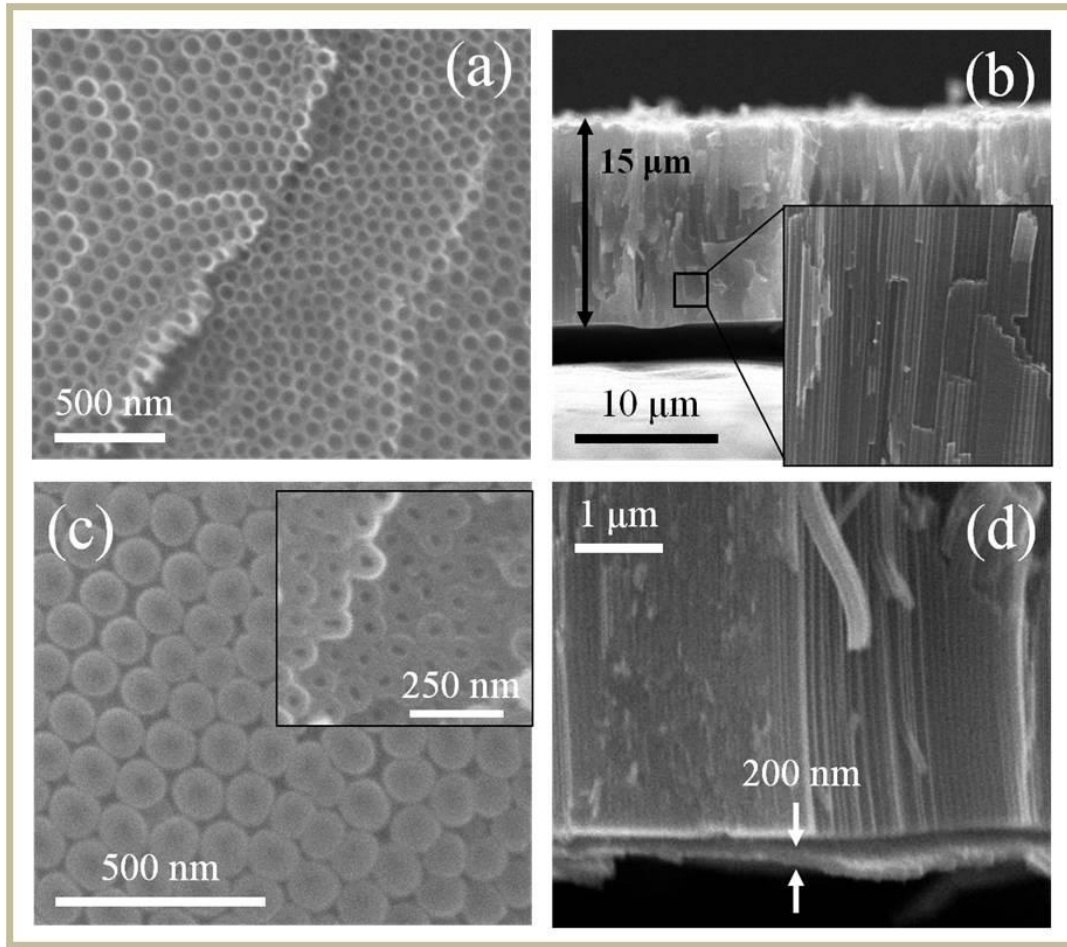


Figure 4-1. (a) clean top surface area (nanotubes with wall thickness of 15 nm), (b) cross section of the nanotubular film with thickness of about 15 μm and in the inset a magnified area of the oriented nanotubes array, (c) the bottom of the nanotubes and in the inset, an area where the caps of the tubes have got off revealing that the wall thickness at the bottom is three times greater (45 nm) than at the top. (d) compact layer with 200 nm thickness, below the nanotubes after the annealing of the as anodized sample at 600 $^{\circ}\text{C}$.

4.3.2. Structural properties

The phase composition and crystallinity of the TiO_2 NTs were investigated by Raman spectroscopy [21]. All the post-annealed TiO_2 NTs were accordingly found to crystallize in the anatase TiO_2 phase, **Figure 4-2** (a). The Raman active modes of the anatase phase at 144 cm^{-1} (E_{g1}), 197 cm^{-1} (E_{g2}), 638 cm^{-1} (E_{g3}), 395 cm^{-1} ($B_{1g(1)}$), 518 cm^{-1} ($B_{1g(2)} + A_{g(1)}$) [22] were invariably identified in the Raman spectra of all TiO_2 NTs, independently of the thermal treatment conditions [23]. Rutile traces of the TiO_2 phase were identified at the bottom of TiO_2

NTs, following annealing temperature of 600 °C. This was confirmed by Raman spectroscopy **Figure 4-3** and is in agreement with the literature data reporting rutile formation at relatively high temperatures [14, 24-27].

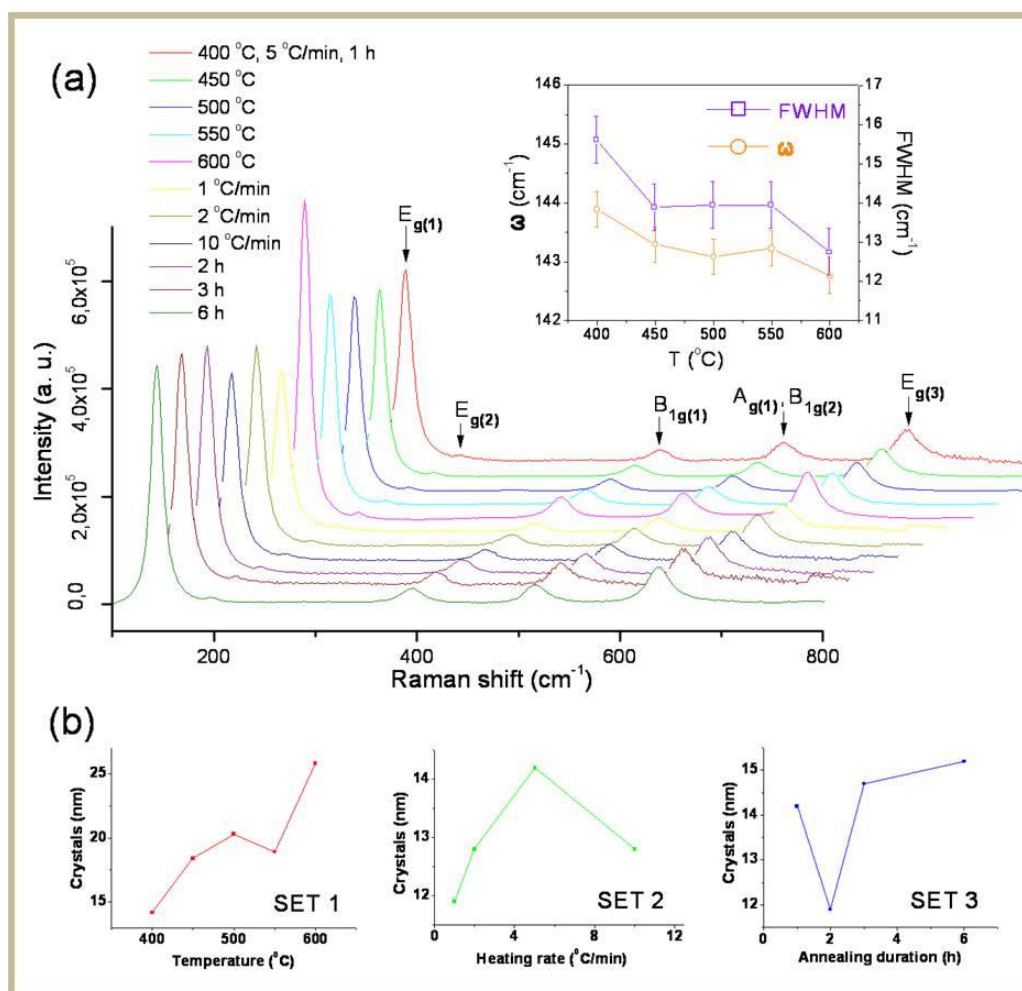


Figure 4-2. (a) Raman spectra of TiO₂ nanotubes under different annealing treatment; inset: variation of the shift (ω) and full width at half maximum (FWHM) of the main anatase mode E_g(1) as a function of the annealing temperature. (b) Crystal size (estimated by micro-Raman spectroscopy) variation under different annealing conditions (set 1: annealing temperature, set 2: heating rate at 400 °C, set 3: annealing duration at 400 °C).

Furthermore, analysis of the TiO₂ NT Raman spectra revealed small but distinct shifts and broadening of the anatase Raman modes following post-thermal treatment, characteristic of size effects arising from optical phonon confinement effect [21]. In order to investigate the size variation of the TiO₂ nanocrystallites as a function of the

annealing conditions, we have employed the lowest frequency and most intense E_g mode, commonly used to model phonon confinement effects in anatase [28,29]. A characteristic example is shown in the inset of **Figure 4-2** (a), where both the peak position (ω) and the full width at half maximum (FWHM) of the E_g anatase mode decrease slightly, though systematically, as the temperature increases. This variation can be explained by the partial release of the optical phonon confinement effect that reflects the progressive growth of the anatase crystallites in the TiO_2 NTs annealed at higher temperatures. **Figure 4-2** (b) displays the relative crystallite size evolution derived from theoretical correlation plots of the E_g frequency vs. crystallite size based on the phonon confinement model [28,29] for the different annealing conditions. The most pronounced size variation was thus obtained for SET 1, confirming that the annealing temperature is the most critical factor for the growth of the anatase crystallites in TiO_2 NTs. At 400 °C (the minimum temperature required for the crystallization of NTs) the anatase crystallites are ~14 nm, matching closely the wall thickness of the tubes (15 nm). The lateral crystal size is thus primarily limited by the NT wall thickness that determines the growth of the crystals perpendicularly to the tube axis, at least at the stage when amorphous titania transforms to the fully crystalline state. This is corroborated by the fact that, by changing the heating rate and/or the annealing duration at 400 °C (SETs 2 and 3), the crystal size remains relatively constant between 12 and 15 nm. As the annealing temperature increases from 400 up to 600 °C, the crystallites increase from 14 up to 25 nm, whereas much less sizable variations (within 2-3 nm) were derived when the heating rate (SET 2) or the duration of annealing (SET 3) were varied at constant temperature of 400 °C.

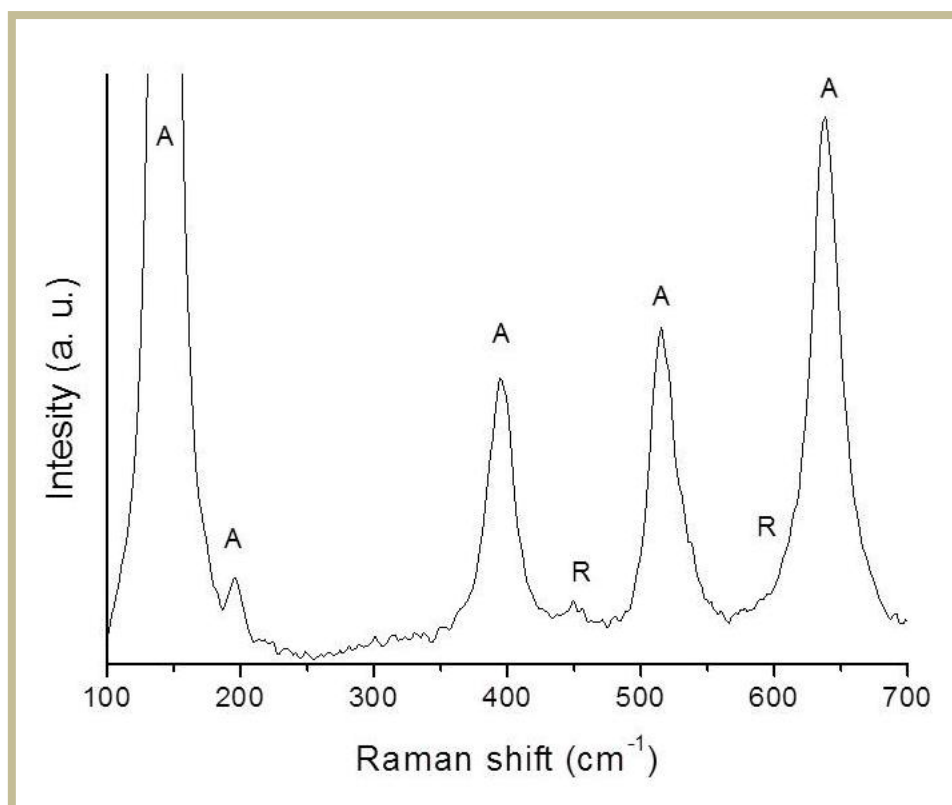


Figure 4-3. Raman spectrum with the Rutile traces which presented at the bottom of the NTs.

4.3.3. Performance-characterization of dye-sensitized solar cells using TiO₂ NT photoelectrodes

The TiO₂ NTs were incorporated as photoelectrodes in DSCs that were evaluated under back side illumination (through the transparent cathode) at 1 sun (1000 W/m²). The corresponding J-V characteristics and the electrical parameters from all sets of cells are summarized in **Table 4-1** and **Figure 4-4** (a)-(c). The obtained efficiencies comply with those recently reported for DSCs employing TiO₂ NT photoelectrodes without TiCl₄ post-treatment [7, 30, 31].

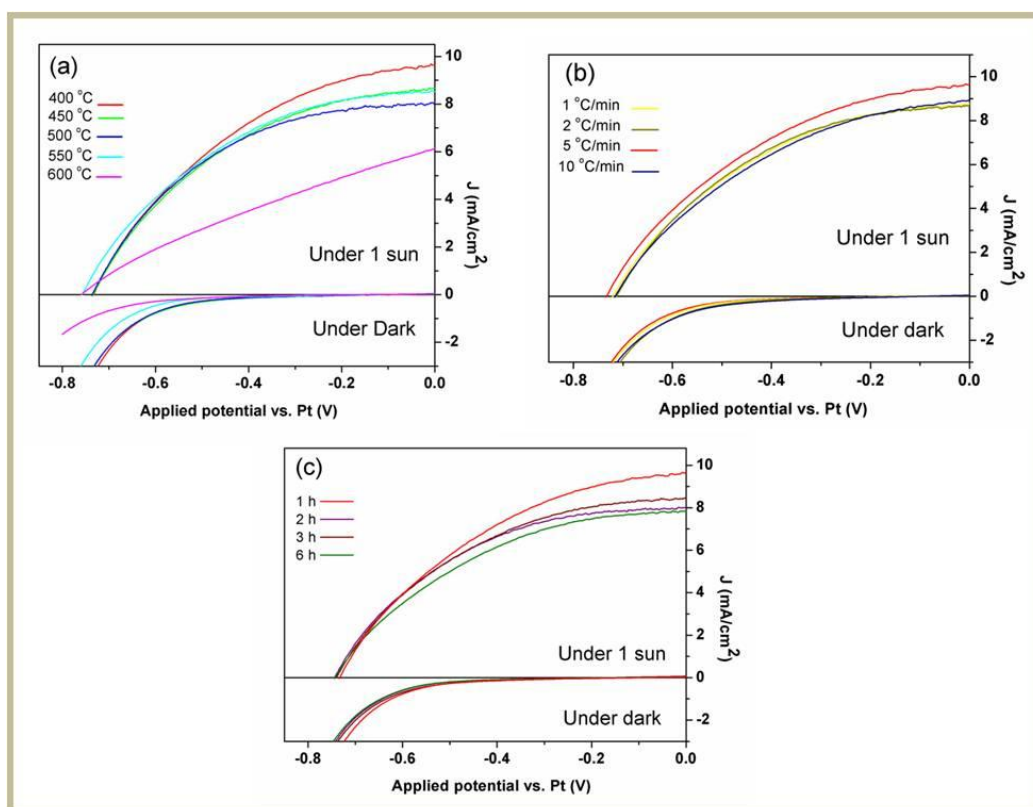


Figure 4-4. Current density-voltage (J-V) characteristics obtained under 1 sun illumination (AM 1.5G) and dark of DSCs using photoelectrodes annealed under (a) different temperatures 400-600 °C, SET 1, (b) using photoelectrodes annealed under heating rate 1-10 °C/min, SET 2 and (c) using photoelectrodes annealed under different durations 1-6 h, SET 3.

Table 4-1. Electrical parameters derived from J-V curves on DSCs based on TiO₂ nanotubes treated under different thermal conditions. It is noted that the samples marked with * (400 °C, 5 °C/min, 1 h) represent the same cell, but they have been added in the table for better comparison.

DSCs characteristics	Thermal treatment												
	SET 1					SET 2				SET 3			
	400	450	500	550	600	1	2	5	10	1	2	3	6
	°C*	°C	°C	°C	°C	°C/min	°C/min	°C/min*	°C/min	h*	h	h	h
J_{sc} (mA/cm ²)	9.65	8.67	8.01	8.53	6.15	8.78	8.67	9.65	8.96	9.65	7.98	8.47	7.83
V_{oc} (mV)	732	733	735	756	759	720	713	732	715	732	744	740	743
FF	0.41	0.43	0.47	0.44	0.30	0.42	0.44	0.41	0.40	0.41	0.46	0.44	0.43
η (%)	2.94	2.77	2.79	2.84	1.41	2.70	2.75	2.94	2.62	2.94	2.77	2.78	2.53

To better understand the photovoltaic performance of the TiO₂ NT photoelectrodes as a function of the annealing conditions and their

structural properties, EIS and IMPS experiments were performed. Specifically, EIS spectra were recorded under illumination at open-circuit conditions, present two prominent semicircles **Figure 4-5**. Fitting of the EIS spectra was performed using a simple equivalent circuit consisted of two RC elements in series with a contact resistance (R_s). The first RC element comprised the charge transfer resistance (R_{Pt+Co}) and capacitance at the counter electrode/electrolyte and/or the TiO_2/Ti interfaces and the second one consisted of a charge recombination resistance at the TiO_2 /electrolyte interface (R_{rec}) and the chemical capacitance (C_μ) that stands for the change of the electron density as a function of the Fermi level of the TiO_2 semiconductor [32]. We should note here that the increase of the R_{Pt+Co} upon altering the annealing conditions (taking into account that the electrolyte/Pt interface is not changed) is certainly related to a modification of the TiO_2/Ti interface (due to variation of the barrier layer upon annealing). The fitted parameters are summarized in **Table 4-2**. Additionally, the recombination lifetimes were derived from the EIS spectra as $\tau_{rec} = (2\pi f_{min})^{-1}$, where f_{min} is the minimum frequency at the minus of the second semicircle.

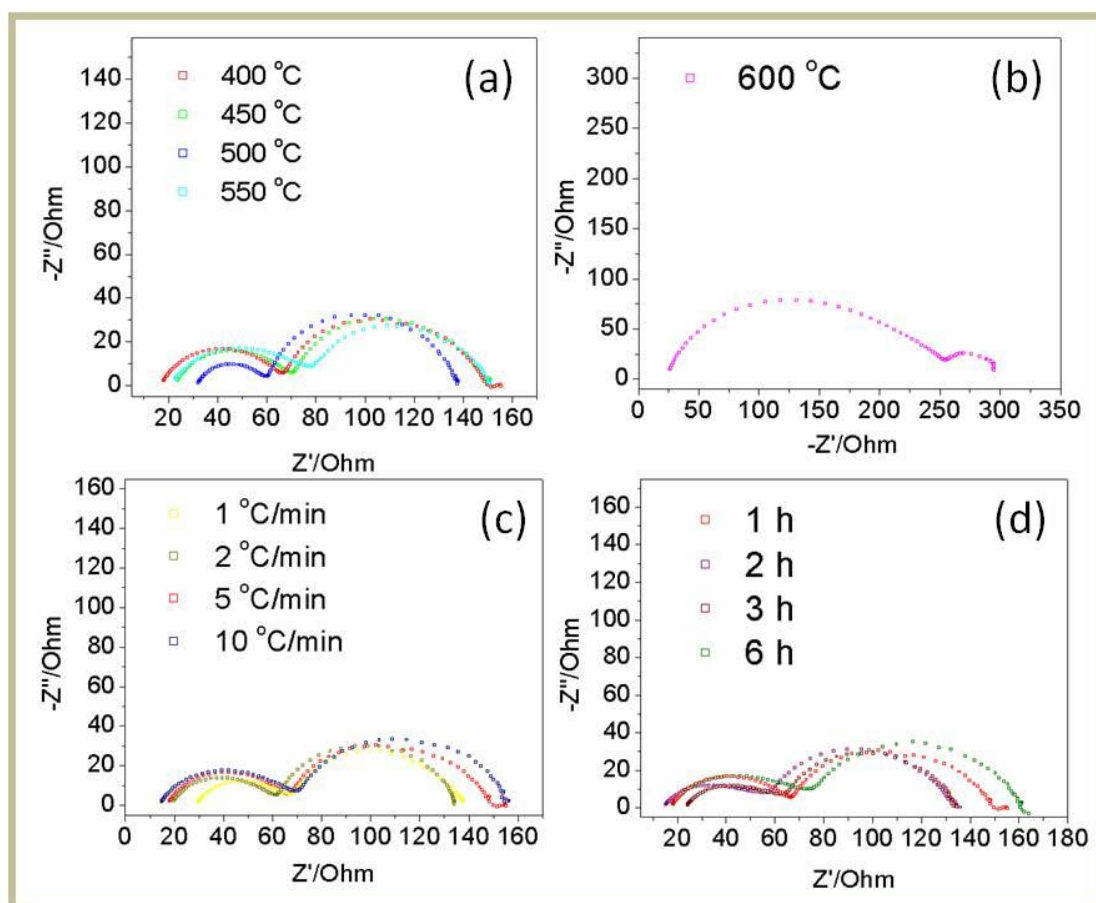


Figure 4-5. EIS spectra under 1 sun illumination (at V_{oc}) for the 3 different experimental SETS. (a) and (b) constant heating rate 5 °C/min and annealing duration at 1 h, varied target temperature from 400 to 600 °C, set 1. (c) Constant annealing duration 1 h and target temperature 400 °C, varied heating rate 1, 2, 5 and 10 °C/min, set 2. (d) Constant heating rate 5 °C/min and target temperature 400 °C, varied annealing duration 1, 2, 3 and 6 h, set 3.

Table 4-2. Electrical parameters derived from the fitting of the EIS spectra using an equivalent circuit of the type: $R_s(R_{Pt+Co}C_1)(R_{rec}C_\mu)$ where constant phase elements (characterized by the parameters Y_o and n) were routinely employed in the equivalent circuit instead of the use of simple capacitances (C_1 or C_μ) for more accurate fitting.

Thermal treatment	R_s (ohm)	R_{Pt+Co} (ohm)	Y_{o1} ($\times 10^{-4} F s^{n-1}$)	n_1	R_{rec} (ohm)	Y_{o2} ($\times 10^{-4} F s^{n-1}$)	n_2
400 °C	17,1	49,2	0,15	0,76	83,4	0,23	0,82
450 °C	22,6	47,2	0,14	0,75	79,6	0,20	0,82
500 °C	31,6	28,6	0,18	0,76	77,1	0,15	0,88
550 °C	21,1	56,6	0,27	0,69	72,7	0,17	0,82
600 °C	21,2	203,0	0,17	0,82	38,0	0,30	0,41
1 °C/min	28,6	38,8	0,26	0,71	69,5	0,21	0,84
2 °C/min	18,4	43,1	0,20	0,73	73,2	0,23	0,86
5 °C/min	17,1	49,2	0,15	0,76	83,4	0,23	0,82
10 °C/min	13,6	55,9	0,24	0,72	86,6	0,27	0,84
1 h	17,1	49,2	0,15	0,76	83,4	0,23	0,82
2 h	13,7	42,5	0,51	0,66	77,2	0,17	0,83
3 h	22,8	40,8	0,48	0,67	70,1	0,20	0,86
6 h	16,6	57,4	0,33	0,69	87,0	0,15	0,84

Likewise, transport time constants under illumination (approximately 0.7-0.8 sun, provided by a powerful red light emitting diode) were derived from the IMPS experiments as $\tau_{trans} = (2\pi f_{min})^{-1}$ where f_{min} is the minimum frequency of the observed semicircle **Figure 4-6** [33]. The obtained dependence of τ_{rec} , τ_{trans} and R_{Pt+Co} with the annealing parameters for the three sets of thermal treatment is plotted in **Figure 4-7**.

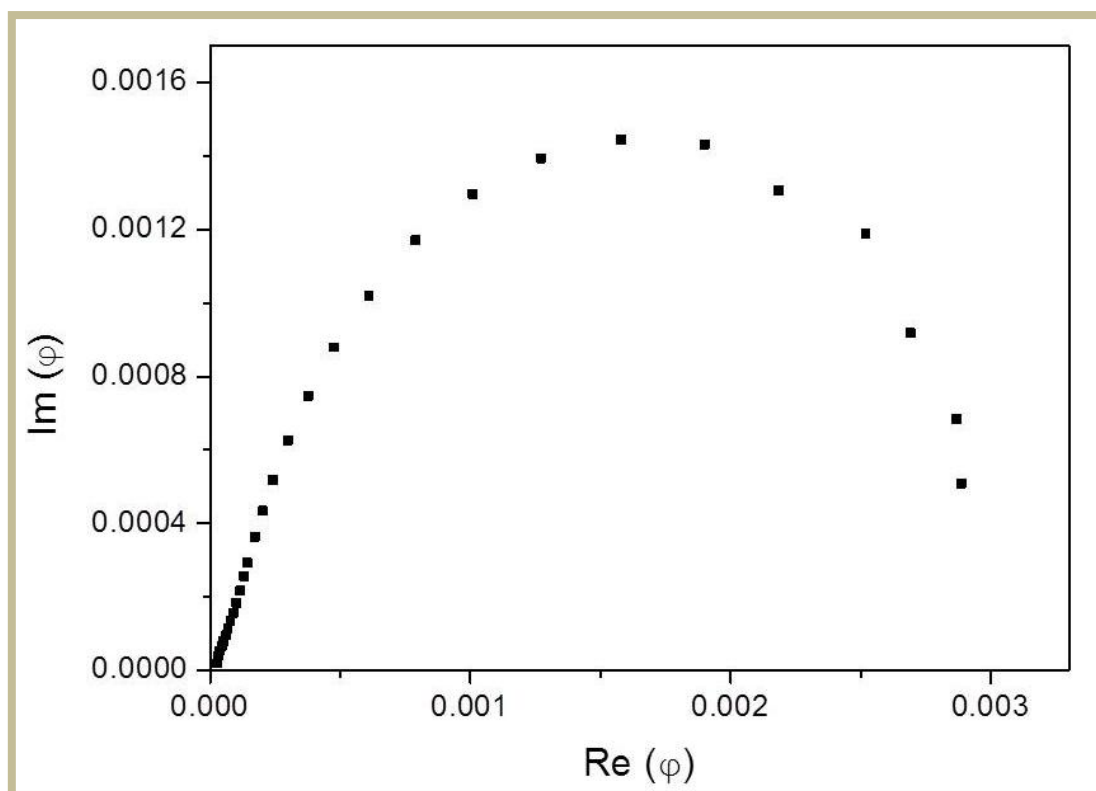


Figure 4-6. Characteristic IMPS Nyquist plot for a DSC based on TiO₂ NTs annealed at 500 °C for 1 h with rate 5 °C/min.

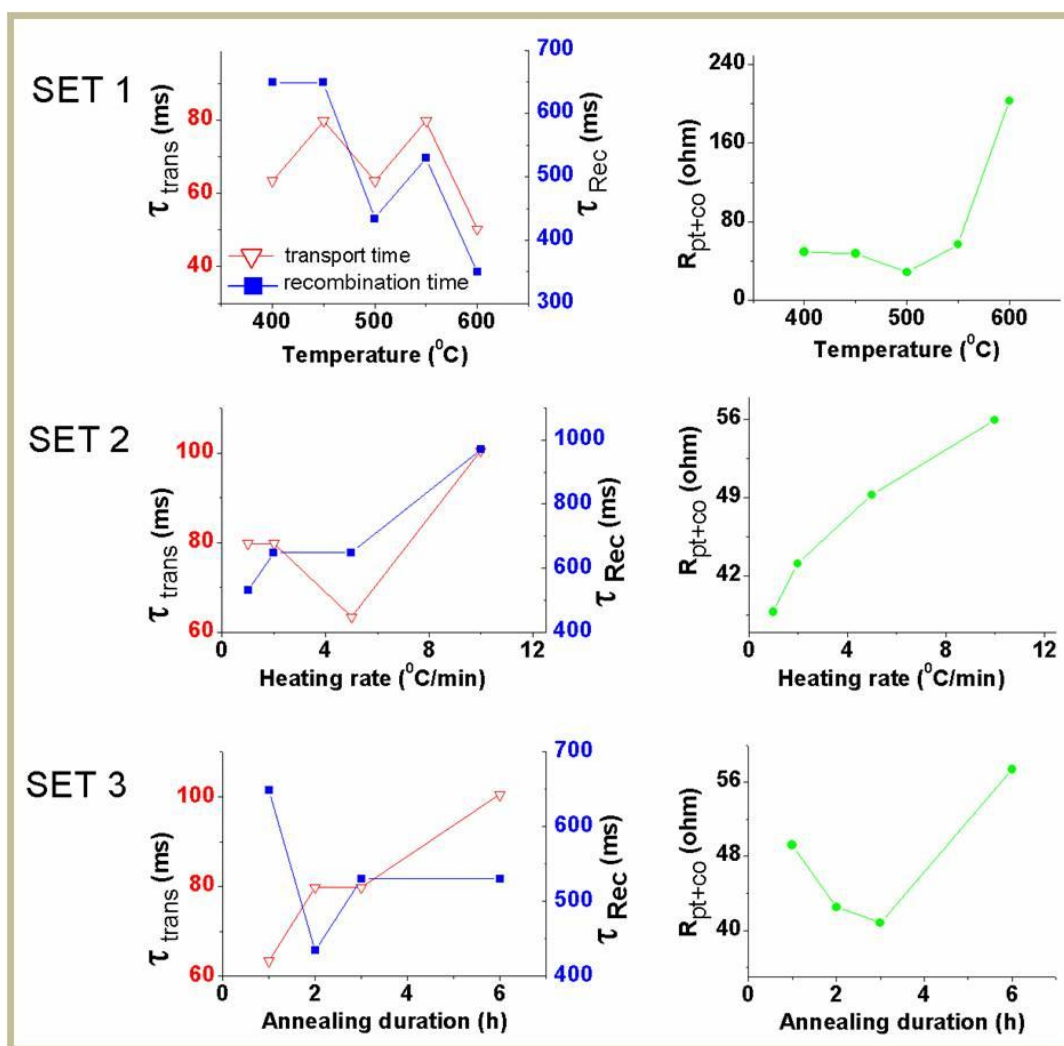


Figure 4-7. (left column) Variation of transport times τ_{trans} (derived from IMPS) and recombination times τ_{rec} (derived from EIS) and (right column) resistances of the Ti-TiO₂ and Pt-electrolyte interfaces R_{Pt+Co} (derived also from EIS), with the annealing conditions (3 different sets of thermal treatment were employed).

Overall, no marked variations were observed for the 3 different SETs of DSCs with the highest efficiency obtained at 400 $^{\circ}C$ (2.9 %), apart from the annealed NTs at 600 $^{\circ}C$ where the efficiency collapsed (1.4 %). A specific trend was observed only in the case of SET 1, where the photocurrent (J_{sc}) generally decreased with the annealing temperature (from 9.65 to 6.15 mA/cm²); surprisingly, **Figure 4-7** shows that there is no clear correlation between electron transport time (τ_{trans}) variation and J_{sc} magnitude. In addition, dye adsorption-desorption experiments permitted the investigation of possible variations of the dye loading capacity for the NTs with increasing

temperature and the concomitant anatase crystallite size growth; the corresponding data summarized in **Table 4-3** show a clear decrease of the dye loading evidenced only for the NTs annealed at 600 °C, where the largest crystallite size has been identified, justifying the sharp decrease of J_{sc} at this temperature. As differences in charge injection are excluded, the J_{sc} decline from 400 to 550 °C can be attributed to decrease of the electron lifetime at short-circuit and thus to corresponding decrease of the electron diffusion length (despite the fact that transport time was not severely affected) upon thermal annealing.

Table 4-3. Dye loading of the NTs per cm² was investigated using UV-Vis spectroscopy by the desorption of the nanotubular samples in a 1/1 H₂O/ EtOH solution which contains 0.2 M NaOH.

Annealing Temperature (°C)	400	450	500	550	600
Adsorbed dye x 10 ⁻⁸ (mol /cm ²)	6.07	6.33	6.28	6.59	5.70

According to the above results, optimal contact and electrical connection between the anatase crystallites is inferred at 400 °C, where their size matches closely the wall thickness of the NTs (15 nm). This is in agreement with previous reports where annealing at slightly higher temperatures (450 °C) resulted in severe cracking at NT walls, while electron transport was faster in NTs annealed at even lower temperatures (350 °C) [20, 34]. Likewise, Frank and co-workers [14] reported that TiO₂ NTs annealed at 400 °C exhibited the largest photocurrent, in line with our observations, whereas annealing at higher temperatures led to a loss of interconnectivity between particles. We should note here that TiO₂ NTs annealed at the highest temperature (600 °C) presented the lowest τ_{trans} , probably due to the very large crystal size [35]; however, fastest transport was accompanied with a very large R_{Pt+Co} (**Figure 4-7**, SET 1) due to the

presence of a very thick barrier layer (**Figure 4-1** (d)) impeding the extraction of electrons through the interface (and thus diminishing J_{sc}). These results demonstrate that besides the desirable single crystalline structure for the NTs [31], good electrical contact among the TiO_2 nanocrystallites, providing a safe path for electron transport along the tube walls, is also an important aspect for high efficiency DSCs.

On the contrary, the V_{oc} presented the opposite trend to that of J_{sc} ; it increased with the temperature increase from 732 up to 759 mV. This behavior was further confirmed by the J-V curves obtained under dark (**Fig. 4-4** (a)), where a significant shift of the dark current towards negative potentials was observed upon increasing the annealing temperature. The V_{oc} increase can not be associated with the reduction of recombination since more rapid recombination kinetics were observed with the temperature increase (see τ_{rec} of SET 1, **Figure 4-7**), similarly to results of K. Zhu et al. [14]. Taking into account the values of the chemical capacitance (see values of Y_{O_2} , **Table 4-2**), we believe that the observed relative decrease from 400 to 500 °C can be attributed to the reduction of trap density (since the material becomes more crystalline), thus augmenting the free electrons density and then V_{oc} . On the other hand, the increase of the chemical capacitance from 500 to 600 °C (meaning more traps) accompanied with the V_{oc} increase, leads us to the conclusion that these are shallow traps (e.g. oxygen vacancies, which have been already shown to act as shallow traps in titanium dioxide [36]) and thus they do not interfere with the recombination process but more likely act as effective density of states to further increase the number of free electrons in the TiO_2 [37]. It appears that thermal treatment at 500 °C is capable of filling up oxygen vacancies in TiO_2 [38], whereas further annealing up to 600 °C does not influence this process. An unusual behavior was again observed for the NTs annealed at 600 °C (presenting the largest V_{oc} despite the highest recombination rate) that

can be ascribed to a Fermi level pinning upon illumination due to the presence of extended surface states at the semiconductor [39].

Although no marked variations were observed on the other two SETs, some specific trends could be clearly identified. In particular, increase of the heating rate from 1 up to 10 °C/min at 400 °C (SET 2), resulted in the decrease of the contact resistance (R_s) (probably due to the creation of a more thin thermal oxide on the contact), while at the same time R_{Pt+Co} increased significantly, leading to a rather low FF. Accordingly, recombination was reduced, whereas the density of states increased, resulting in moderate values of V_{oc} . Similar effects were observed in the case of set 3. However, overall we could conclude that variation of the heating rate and the duration of annealing at 400 °C, did not affect at a large extent the performance of the corresponding DSCs.

4.4. Conclusions

The influence of the annealing treatment conditions (annealing temperature, heating rate and duration) on the structural properties of self-assembled TiO_2 nanotubes grown under prolonged anodization was systematically investigated with respect to their performance and electrical characteristics as photoelectrodes in back-side illuminated DSCs. The annealing temperature was identified as the most critical parameter for controlling and optimizing the structure-performance relationship for TiO_2 NTs. The optimum annealing temperature was 400 °C, where TiO_2 NTs fully crystallize in the anatase phase, with crystallites of the same mean size as the tube walls of the NTs. At this temperature, good electrical connections between the crystallites as well as with the Ti substrate are inferred that promotes electron transport and leads to a maximum J_{sc} in the corresponding DSCs. Despite the enhanced crystallinity of TiO_2 NTs upon annealing at higher temperatures, recombination is accelerated. On the other

hand, a systematic reduction of the effective density of states upon annealing results in an increased V_{oc} , which however can not compensate for the concurrent losses of J_{sc} . Variation of the heating rate and duration of the annealing process at the optimum temperature resulted in slight modifications of the photovoltaic performance of the corresponding DSCs. We can accordingly propose that highly efficient TiO_2 NT photoelectrodes for DSCs can be prepared by post-thermal treatment at 400 °C with a heating rate 5 °C/min for a total time of only 1 h. Further optimization is currently pursued toward the elimination of traps from the TiO_2 NTs that would accelerate the trap-limited diffusion of electrons compared to the standard nanoparticulate DSC photoelectrodes and pave the way for high efficiency DSCs based on TiO_2 NT arrays.

4.5. References

1. P. Roy, D. Kim, K. Lee, E. Spiecker, P. Schmuki "TiO₂ nanotubes and their application in dye-sensitized solar cells" *Nanoscale* 2 (2010) 45.
2. A. Hagfeldt, G. Boschloo, L. Sun, L. Kloo, H. Pettersson "Dye-sensitized solar cells" *Chem. Rev.* 110 (2010) 6595.
3. J. Yan, F. Zhou "TiO₂ nanotubes: Structure optimization for solar cells" *J. Mater. Chem.* 21 (2011) 9406.
4. Y. Liao, W. Que, P. Zhong, J. Zhang, Y. He "A facile method to crystallize amorphous anodized TiO₂ nanotubes at low temperature" *ACS Appl. Mater. Interfaces* 3 (2011) 2800.
5. X. Xiao, K. Ouyang, R. Liu, J. Liang "Anatase type titania nanotube arrays direct fabricated by anodization without annealing" *Appl. Surf. Sci.* 255 (2009) 3659.
6. H. Liu, L. Tao, W.Z. Shen "Optimal self-organized growth of small anodic TiO₂ nanotubes with "micro-annealing" effect under complex

conditions via reaction–diffusion approach” *Electrochim. Acta* 56 (2011) 3905.

7. S. Lee, I. J. Park, D. H. Kim, W. M. Sung, D. W. Kim, G. S. Han, J. Y. Kim, H. S. Jung, K. S. Hong “Crystallographically preferred oriented TiO₂ nanotube arrays for efficient photovoltaic energy conversion” *Energy Environ. Sci.* 5 (2012) 7989.

8. K. Shankar, M. Paulose, G. K. Mor, O. K. Varghese, C. A. Grimes “A study on the spectral photoresponse and photoelectrochemical properties of flame-annealed titania nanotube-arrays” *J. Phys. D: Appl. Phys.* 38 (2005) 3543.

9. N. K. Allam, C. A. Grimes “Effect of rapid infrared annealing on the photoelectrochemical properties of anodically fabricated TiO₂ nanotube arrays” *J. Phys. Chem. C* 113 (2009) 7996.

10. P. Xiao, D. Liu, B. B. Garcia, S. Sepehri, Y. Zhang, G. Cao “Electrochemical and photoelectrical properties of titania nanotube arrays annealed in different gases” *Sensor. Actuat. B* 134 (2008) 367.

11. N. G. Park, V. D. Lagemaat, A. J. Frank “Comparison of Dye-Sensitized Rutile- and Anatase-Based TiO₂ Solar Cells” *J. Phys. Chem. B.* 104 (2000) 8989.

12. B. Yang, C. K. Ng, M. K. Fung, C. C. Ling, A. B. Djurisic, S. Fung “Annealing study of titanium oxide nanotube arrays” *Mater. Chem. Phys.* 130 (2011) 1227.

13. L. Liu, J. Chan, T. K. Sham “Calcination-induced phase transformation and accompanying optical luminescence of TiO₂ nanotubes: an X-ray absorption near-edge structures and X-ray excited optical luminescence study” *J. Phys. Chem. C* 114 (2010) 21353.

14. K. Zhu, N. R. Neale, A. F. Halverson, J. Y. Kim, A. J. Frank “Effects of annealing temperature on the charge-collection and light-harvesting properties of TiO₂ nanotube-based dye-sensitized solar cells” *J. Phys. Chem. C* 114 (2010) 13433.

15. J. Wang, Z. Lin "Dye-sensitized TiO₂ nanotube solar cells with markedly enhanced performance via rational surface engineering" *Chem. Mater.* 22 (2010) 579.
16. K. Shankar, J. Bandara, M. Paulose, H. Wietasch, O. K. Varghese, G. K. Mor, T. J. LaTempa, M. Thelakkat, C. A. Grimes "Highly efficient solar cells using TiO₂ nanotube arrays sensitized with a donor-antenna dye" *Nano Lett.* 8 (2008) 1654.
17. N. Vaenas, T. Stergiopoulos, A. G. Kontos, V. Likodimos, N. Boukos, P. Falaras "Sensitizer activated solar cells based on self-organized TiO₂ nanotubes" *Microelectron Eng* 90 (2012) 62.
18. A. Valota, D.J. LeClere, P. Skeldon, M. Curioni, T. Hashimoto, S. Berger, J. Kunze, P. Schmuki, G.E. Thompson "Influence of water content on nanotubular anodic titania formed in fluoride/glycerol electrolytes" *Electrochim. Acta* 54 (2009) 4321.
19. J. Chen, J. Lin, X. Chen "Self-assembled TiO₂ nanotube arrays with U-shaped profile by controlling anodization temperature" *J. Nanomaterials* (2010) Article ID 753253, 4 pages.
20. S. P. Albu, H. Tsuchiya, S. Fujimoto, P. Schmuki "TiO₂ Nanotubes – Annealing effects on detailed morphology and structure" *Eur. J. Inorg. Chem* 27 (2010) 4351.
21. V. Likodimos, T. Stergiopoulos, P. Falaras "Phase composition, size, orientation, and antenna effects of self-assembled anodized titania nanotube arrays: a polarized micro-Raman investigation" *J. Phys. Chem. C* 112 (2008) 12687.
22. T. Ohsaka, F. Izumi, Y. Fujiki "Raman spectrum of anatase, TiO₂" *J. Raman Spectrosc.* 7 (1978) 321.
23. F. D. Hardcastle, H. Ishihara, R. Sharma, A. S. Biris "Photoelectroactivity and Raman spectroscopy of anodized titania (TiO₂) photoactive water-splitting catalysts as a function of oxygen-annealing temperature" *J. Mater. Chem.* 21 (2011) 6337.

24. D. Fang, Z. Luo, K. Huang, D. C. Lagoudas “Effect of heat treatment on morphology, crystalline structure and photocatalysis properties of TiO₂ nanotubes on Ti substrate and freestanding membrane” *Appl. Surf. Sci.* 257 (2011) 6451.
25. A. Tighineanu, T. Ruff, S. Albu, R. Hahn, P. Schmuki “Conductivity of TiO₂ nanotubes: Influence of annealing time and temperature” *Chem. Phys. Lett.* 494 (2010) 260.
26. C.C. Chen, W. C. Say, S. J. Hsieh, E. W. G. Diau “A mechanism for the formation of annealed compact oxide layers at the interface between anodic titania nanotube arrays and Ti foil” *Appl. Phys. A* 95 (2009) 889.
27. H. Cheng, A. Selloni “Surface and subsurface oxygen vacancies in anatase TiO₂ and differences with rutile” *Phys. Rev. B* 79 (2009) 092101.
28. A. Pottier, S. Cassaignon, C. Chaneac, F. Villain, E. Tronc, J. P. Jolivet “Size tailoring of TiO₂ anatase nanoparticles in aqueous medium and synthesis of nanocomposites. Characterization by Raman spectroscopy” *J. Mater. Chem.* 13 (2003) 877.
29. S. Kelly, F. H. Pollak, M. Tomkiewicz “Raman spectroscopy as a morphological probe for TiO₂ aerogels” *J. Phys. Chem. B* 101 (1997) 2730.
30. D. Kim, P. Roy, K. Lee, P. Schmuki “Dye-sensitized solar cells using anodic TiO₂ mesosponge: Improved efficiency by TiCl₄ treatment” *Electrochem Comm.* 12 (2010) 574.
31. M. H. Jung, M. J. Chu, M. G. Kang “TiO₂ nanotube fabrication with highly exposed (001) facets for enhanced conversion efficiency of solar cells” *Chem. Commun.* 48 (2012) 5016.
32. S. R. Raga, E. M. Barea, F. Fabregat-Santiago “Analysis of the Origin of Open Circuit Voltage in Dye Solar Cells” *J. Phys. Chem. Lett.* 3 (2012) 1629.

33. P. T. Hsiao, Y. J. Liou, H. Teng "Electron transport patterns in TiO₂ nanotube arrays based dye-sensitized solar cells under frontside and backside illuminations" J. Phys. Chem. C 115 (2011) 15018.
34. A. Ghicov, S. P. Albu, R. Hahn, D. Kim, T. Stergiopoulos, J. Kunze, C. A. Schiller, P. Falaras, P. Schmuki "TiO₂ nanotubes in dye-sensitized solar cells: critical factors for the conversion efficiency" Chem. Asian J. 4 (2009) 520.
35. K. Zhu, N. Kopidakis, N. R. Neale, J. van de Lagemaat, A. J. Frank "Influence of surface area on charge transport and recombination in dye-sensitized TiO₂ solar cells" J. Phys. Chem. B 2006, 110 (2006) 25174.
36. S. Duenas, H. Garcia, E. S. Andres, M. T. Luque, I. Martil, G. G. Diaz, K. Kukli, T. Uustare, J. Aarik "A comparative study of the electrical properties of TiO₂ films grown by high-pressure reactive sputtering and atomic layer deposition" Semicond. Sci. Technol. 20 (2005) 1044.
37. T. Stergiopoulos, P. Falaras "Minimizing energy losses in dye-sensitized solar cells using coordination compounds as alternative redox mediators coupled with appropriate organic dyes" Adv. Energy Mater. 2 (2012) 616.
38. J. Bisquert "Theory of the Impedance of Electron Diffusion and Recombination in a Thin Layer" J. Phys. Chem. B 106 (2002) 325.
39. R. Memming "Semiconductor Electrochemistry" Wiley-VCH, Weinheim, Germany, 2001.

Chapter 5. Influence of controlled-charge anodization processes on the morphology of TiO₂ nanotubes and their efficiency in dye-sensitized solar cells

The effect of the electrochemical anodization growth process on the development of self-organized TiO₂ nanotube (NT) films and their efficiency as photoelectrodes in dye sensitized solar cells (DSCs) has been comparatively investigated, by keeping the total anodization charge constant. Slow and rapid potentiostatic anodization processes were accordingly compared to the galvanostatic one, while a two step potentiostatic - galvanostatic technique was applied for the first time for the growth of TiO₂ NT arrays, as a step forward in relation to the existing potentiostatic – potentiostatic (P-P) technique. Scanning electron microscopy and Raman spectroscopy verified the wide diversity in the morphological and structural characteristics of the TiO₂ NTs obtained by the different anodization modes. The novel approach of galvanostatic tube growth on a potentiostatically patterned Ti foil provided the most uniform TiO₂ nanotubular films with clean top surface exempt of nanograss or cracks over extended areas. Evaluation of the TiO₂ NTs performance as photoelectrodes in DSC devices showed distinct differences of their electrical parameters that finely reflected the underlying structure/morphology variations of the different anodic oxidation conditions. Galvanostatic TiO₂ NT films presented the most favorable (open-ordered) structure for DSC photoelectrodes with superior electrical performance, essentially impaired by a relatively low fill factor that requires improvement by appropriate post-treatment. Furthermore, despite the marked differences in morphology, the TiO₂ NT photoelectrodes exhibited comparable overall performance (of the order of 4%), with only exception the P-P samples which presented slightly lower (about 25 %)

photovoltaic efficiency. These results indicate that the anodization charge is a critical factor that effectively controls the nanotubes behavior when they are used as photoelectrodes in DSCs.

5.1. Introduction

Controlled growth of self-organized TiO₂ nanotube (NT) arrays by electrochemical anodization of titanium foils has been established as a versatile synthetic means to a robust, nanotubular architecture that attracts particular attention for various functional applications [1-3] including dye sensitized solar cells (DSCs) [4-15].

Potentiostatic anodization is the most common electrochemical technique for the preparation of self-organized titania nanotube arrays, where control of the processing conditions i.e. duration of anodization [5] and applied potential [16] together with the composition and pH of the electrolyte allow fine tuning of the TiO₂ NTs morphological characteristics (tube length, diameter, wall thickness and roughness, pore size and tube-to-tube spacing) [7,17,18]. Galvanostatic anodization is less common, though it has been demonstrated as an efficient alternative mode for the fabrication of TiO₂ NT arrays [19-22]. Recently, a new approach for the preparation of TiO₂ NTs on a patterned Ti foil has been developed by means of two step anodization process [23]. In the first step, potentiostatic anodization is applied and subsequently the developed TiO₂ NTs are detached from the titanium foil leaving behind a pattern, where the new tubes grow during the second anodization step [24]. Titania nanotubes prepared by the two step potentiostatic – potentiostatic (V–V) method, are organized in a well ordered film, free of surface defects [25,26]. The P-P preparation of TiO₂ NTs has been further exploited for the guided anodization and fabrication of asymmetrical NTs onto patterned Ti foils treated by focused ion beam lithography [27,28].

The aim of the present chapter is to systematically investigate the physicochemical properties of TiO₂ NTs, prepared by different anodization processes and to evaluate their efficiency as photoelectrodes in DSCs. Potentiostatic anodization growth of TiO₂ NTs under slow and rapid rates was compared to the galvanostatic process by keeping the total anodization charge constant, while two step potentiostatic – galvanostatic anodization technique applied for the first time for the preparation of TiO₂ NT arrays, the common method of potentiostatic – potentiostatic formation of NT samples was used as reference. The influence of the anodization mode as well as the ensuing process efficiency on the TiO₂ NT morphological characteristics was thereby analyzed providing a sensitive way for fine tuning their performance as photoelectrodes in DSC devices.

5.2. Experimental

5.2.1. TiO₂ nanotubes preparation

Titanium foil (Sigma Aldrich 99.7 %, 0.25 mm) was used as substrate for the anodization. Prior to the anodization, pieces (2 x 2 cm²) of the Ti foil were ultrasonicated in acetone, isopropanol and methanol for 10 min, then washed with water and dried under nitrogen. Anodization was performed in an appropriate electrochemical cell, made of Teflon, at ambient temperature. The working area was 1.32 cm² and the distance between the anode (Ti foil) and the cathode (Pt mesh) was set at 2 cm. Slow potentiostatic anodization was performed with constant voltage of 30 V for 16 h in an organic, ethylene glycol electrolyte (Merck 99.5 %) containing 1 vol % deionized water and 0.45 wt % of NH₄F (95 %, Janssen Chimica) (samples designated as P30). Rapid potentiostatic anodization (P60 samples, corresponding to an applied voltage of 60 V for 2 h) was carried out in an aged electrolyte containing 2 vol % deionized water

and 0.30 wt % NH_4F . The aged electrolyte was used in order to provide TiO_2 NTs with optimized adherence on the substrate and was prepared by performing a blank anodization step according to [29].

Galvanostatically anodized TiO_2 nanotubes (G samples), were prepared by applying a constant current density of 3.15 mA cm^{-2} for 2 h using the same electrolyte as P60 (electrolyte ageing was found to have no appreciable effect on the TiO_2 NT films in this case). Potentiostatic-galvanostatic (P-G) samples were formed utilizing a combination of the two anodization methods. A concave pattern was initially prepared by long (16 h duration) potentiostatic anodization at 60 V using the same electrolyte as for the preparation of G samples. Then, the samples were ultrasonicated in water for 10 min leading to the detachment of the TiO_2 NTs from the Ti foil (a nanotubular TiO_2 membrane of about $50 \mu\text{m}$ was thereby produced). The patterned Ti foils were re-anodized in the same electrolyte for 2 h; with a constant density current of 3.15 mA cm^{-2} for the P-G samples and with a constant voltage of 60 V for the P-P samples.

At the end of growth, all samples were washed with deionized water (the P30 samples were additionally immersed in EtOH for 1 h and then soaked in ultrasounds for 15 min), in order to remove the surface debris and subsequently dried in nitrogen stream [30]. Finally, all samples were thermally annealed at 450°C for 60 minutes (heating rate of 5°C min^{-1}) in order to induce crystallinity.

5.2.2. Surface modification and cell assembly

After annealing, the TiO_2 NTs films were immersed in 0.3 mM N719 dye (Dyesol Ltd.) solution of EtOH for 3 days. DSCs were constructed by placing a drop of a liquid electrolyte (consisted of 1 M dimethylimidazolium iodide, 0.05 M LiI, 0.015 M I_2 , 0.5 M tert-butylpyridine and 0.1 M guanidine thiocyanate in

acetonitrile/valeronitrile 85/15, v/v) onto the photoelectrode and sandwiching against a Pt transparent counter electrode Pt/FTO.

5.2.3. Characterization

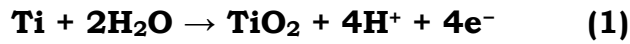
The morphology of the TiO₂ NTs was investigated using a PHILIPS Quanta Inspect Scanning Electron Microscope (SEM). Raman spectra were recorded in backscattering configuration on a Renishaw in Via Reflex microscope using an Ar⁺ ion laser ($\lambda=514.5$ nm) as excitation source. The laser beam was focused onto the samples by means of a 50 \times objective, while the laser power density was kept at low levels (~ 0.1 mW/ μm^2) to avoid local heating of the samples. I-V characteristics were obtained through linear sweep voltammetry under back-side illumination of the DSCs from the transparent counter electrode (CE) side, using solar simulated light (1 sun, 1000 W m⁻²) from a 300W-Xe source operating in combination with AM 1.5G and UV cut-off optical filters (Oriel). Electron lifetime constants (τ) were determined by Intensity Modulated Voltage Spectroscopy (IMVS), using an Autolab potentiostat (Ecochemie) and FRA system. A red diode emitting at 625 nm was used as the light source for both AC and DC illumination, controlled by the FRA module.

5.3. Results and Discussion

5.3.1. TiO₂ NT characteristics

Figure 5-1 shows the anodization curves of the five different samples. At the early stages of the anodization, an abrupt decrease of the current in the potentiostatic mode and increase of the voltage under galvanostatic conditions are commonly observed signaling the formation (and controlling the thickness) of an initial compact TiO₂

layer on the Ti foil [31,32]. As the process continued, this compact layer was dissolved by the fluoride ions of the electrolyte initializing the tubes formation. This point can be hardly traced in the anodization curves for fresh electrolytes, samples P30 and G, but can be clearly identified by a small kink in the anodization curves for the aged electrolytes, samples P60, P-G and P-P [33]. Furthermore, **Figure 5-1** shows that the P60, P-G and P-P samples reach a rather steady state earlier than P30 and G, due to the aged electrolyte which is enriched by plenty of titanium and fluoride ions during the previous anodization [34]. According to the literature [35], the nanotube's growth gradually decreases and finally balances between the oxidation rate of the formed oxide (eq. 1) and the dissolution rate of the oxide (eq. 2).



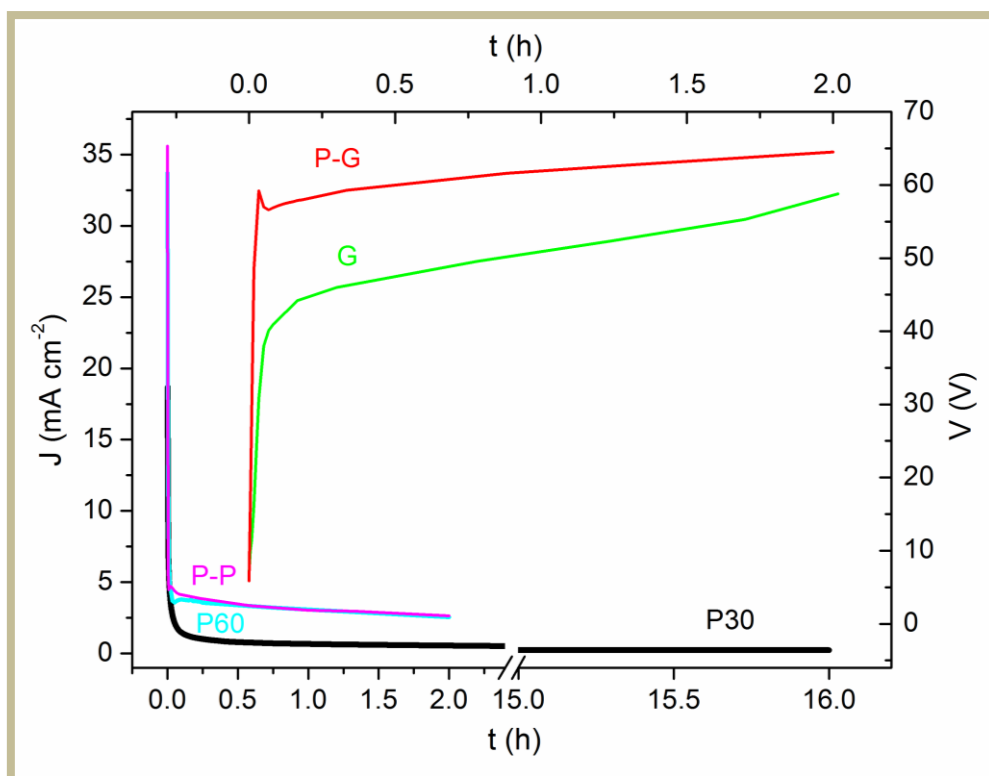


Figure 5-1. Characteristic curves for the different anodization processes: P30, P60 and P-P samples (constant voltage at 30 and 60 V in raw and 60 V in pattern Ti foil). G and P-G samples (constant current at 3.15 mA cm⁻² in raw and pattern Ti foil).

The first and second columns in **Figure 5-2** depict characteristic SEM top images (low and high magnification) of the different TiO₂ NT films, illustrating the pronounced variations on the surface morphology and coherence of the nanotube arrays by the anodization mode. The third column shows the corresponding SEM cross section images. The surface of the P30 (**Figure 5-3** TEM analysis) samples is extensively covered by melt or broken tubes, called nanograss [36]. Nanograss is a consequence of prolonged anodization, which leads to the dissolution of the initial compact layer and the tubes collapse. In addition, some cracks exist, probably deriving from the post annealing treatment [14]. The surface of the TiO₂ NTs was markedly improved under rapid potentiostatic anodization at higher voltage (P 60), where both, nanograss and film cracking, were significantly reduced. Galvanostatically prepared TiO₂ NTs under the same anodization charge for 2 h exhibit an average surface morphology comprising both grassy, porous and clean areas.

This may be attributed to the formation of an initial oxide film with variable thickness as a result of a non-uniform current distribution [37], in combination with the high dissolution rate provided by the fresh electrolyte. Combined potentiostatic-galvanostatic anodization, where tubes grew galvanostatically onto a patterned Ti foil (P-G samples), resulted in highly ordered arrays that were essentially free of grass and cracks over extended scales. A magnification of the P-G TiO₂ NTs top surface is also included, showing the highly uniform self-ordering of the nanotubes in a hexagonal arrangement [23,38]. The only deficiency of these films is that the tubes are welded at the top. It must be noticed that the P-P samples exhibit the most clean (free of debris) surface, which is also constituted of well separated tubes.

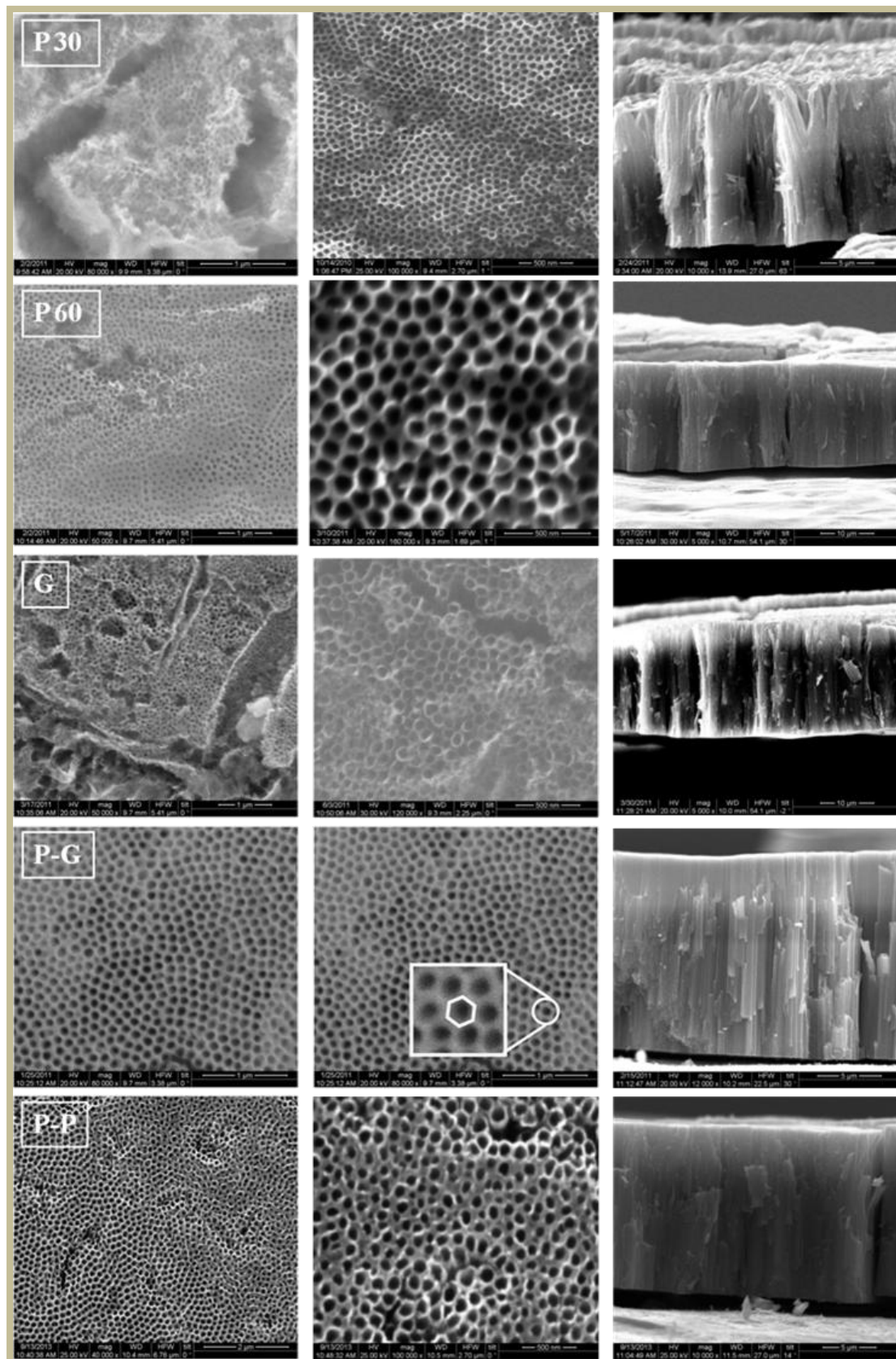


Figure 5-2. SEM images of the various TiO_2 NTs samples: the first column summarizes the characteristic top view SEM images of the different NTs films (P 30, P 60, G, P-G, P-P), the second column shows the high magnification images taken from 'clear' areas and the third one the corresponding cross section SEM images.

For the P-G film, a zoomed area of interest is added (inset).

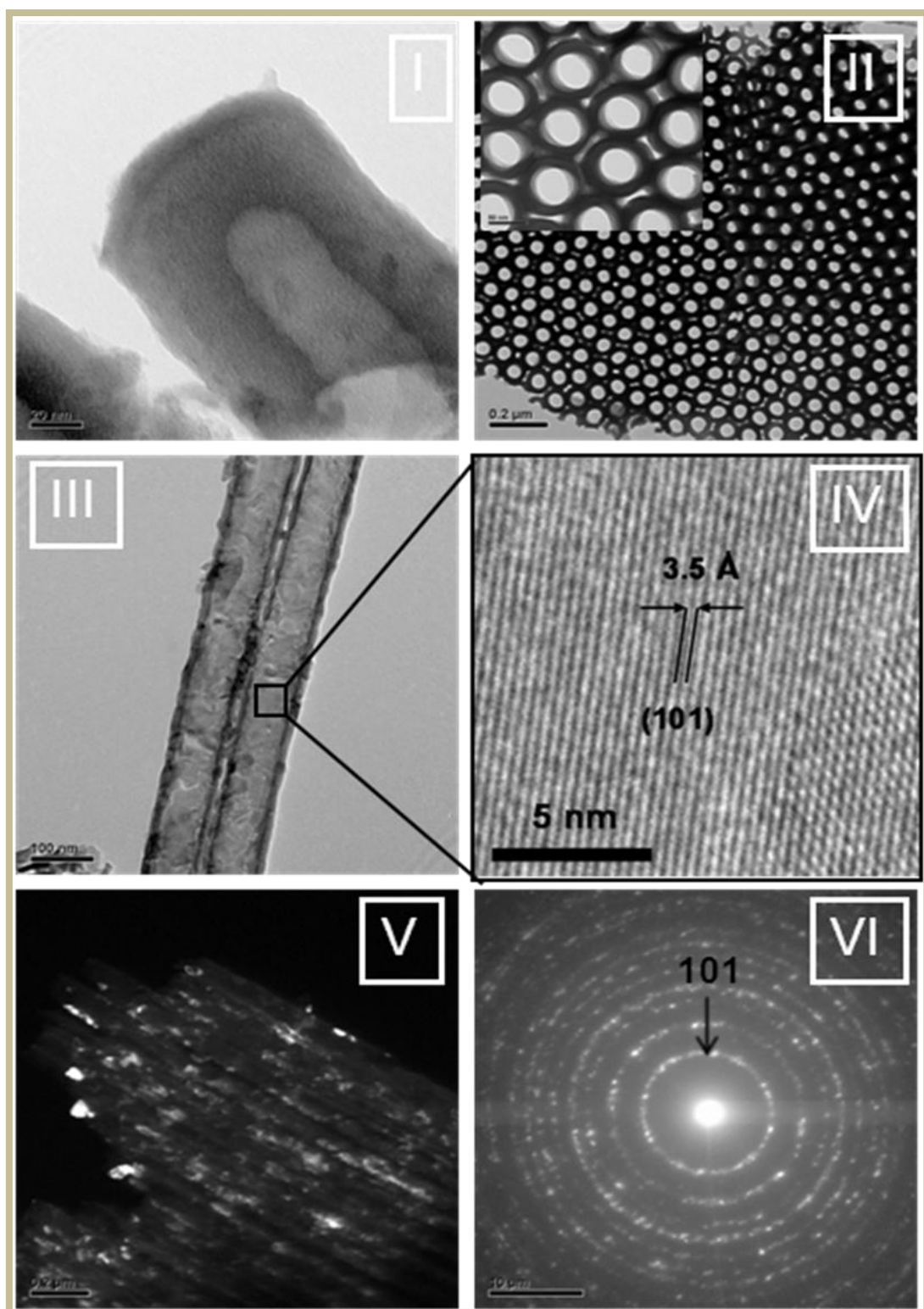


Figure 5-3. TEM images (I, II) of P30 sample before annealing (amorphous) and after thermal treatment when the material is transformed into polycrystalline (III, IV, V and VI). As shown in the (I) and (II) the amorphous NTs of the P 30 sample have a thick barrier layer of about 45 nm; additionally the voids, which exist between the tubes, are well defined. The (III-IV) shows the polycrystalline structure of the nanotubes, after annealing. More specifically, (III and V-dark field) points out a wide distribution of the crystallites size. In (IV) the lattice fringes of the TiO_2 nanocrystals allow the identification of lattice spacings of $\sim 3.5 \text{ \AA}$, reflecting the d-spacing of (1 0 1) crystallographic plane in anatase, which corresponds to the most thermodynamically stable {101} facets. The existence of Debye–Scherrer rings in selected area electron diffraction pattern (SAED) further evidences the formation of anatase crystallites (VI).

Figure 5-4 presents characteristic SEM images of the TiO_2 NT membrane derived from the first step of the P-G and P-P anodizations including the cross section, the bottom of the membrane (barrier layer) and the resulting pattern on the Ti foil after peeling off. It is worth noting that although the TiO_2 NT membrane is a byproduct of the procedure, it can be useful for other applications such as photocatalysis [39].

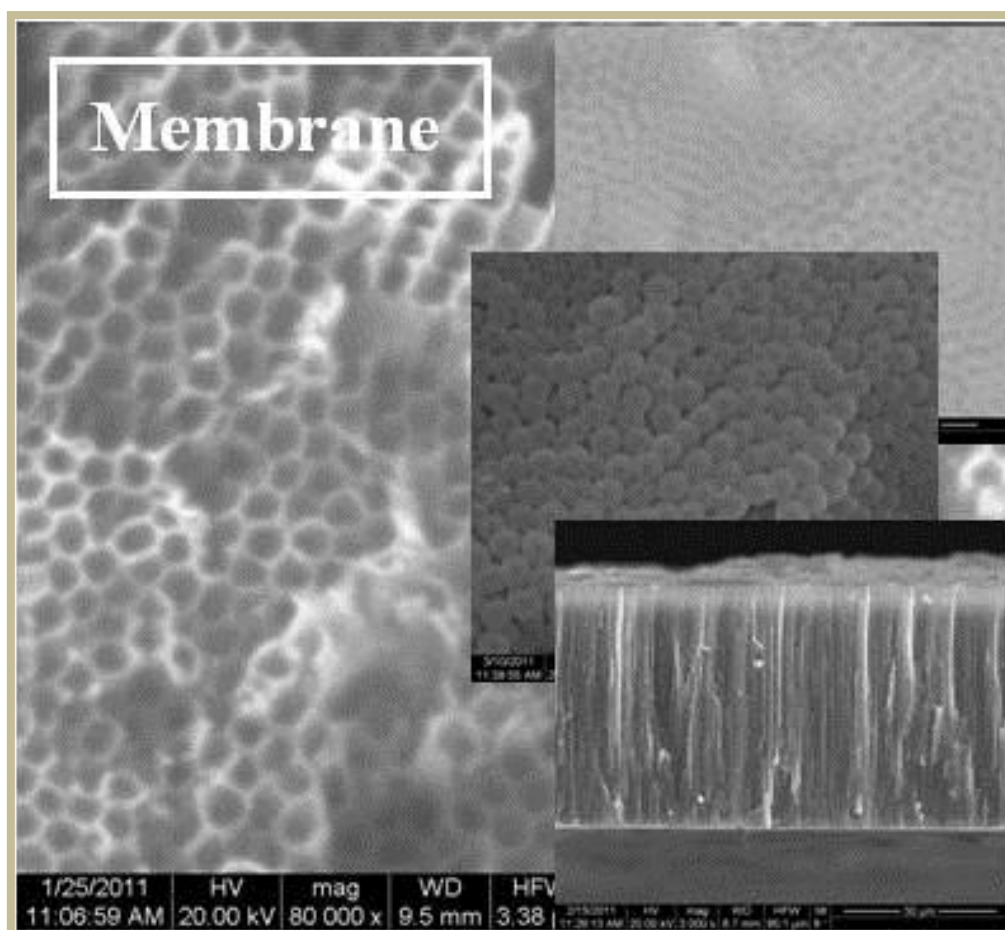


Figure 5-4. Characteristic SEM images of the TiO_2 NT membrane derived from the first step of the P-G anodization including the cross section, the bottom of the membrane (barrier layer) and the resulting pattern on the Ti foil after peeling off.

This method of guided anodization has various advantages. At first, it is an easy alternative way to “flatten” the rough surface of the Ti foil, without hard trials [40] or mechanical polishing. Furthermore, it provides a very efficient route for the fabrication of titania nanotubes of different shapes [27] and high degree of ordering and orientation.

Table 5-1 summarizes the morphological characteristic parameters of the TiO_2 NT arrays determined by the SEM analysis, namely, length (L), internal diameter (D), wall thickness (w) and surface density (ρ) of the tubes, corresponding to the number of tubes per unit area. Accordingly, the P30 sample has the shortest length, impeding significantly its surface area and capability for dye loading, the thinnest wall thickness (10 nm) and the largest surface density

(220 μm^{-2}). Rapid potentiostatic anodization (P60) resulted in the increase of both length and internal diameter as well as wall thickness as a result of the high voltage [32,16]; these morphology variations diminished the surface density down to 64 μm^{-2} . The galvanostatic NT arrays retained the structural advantages of the slow and rapid potentiostatic TiO_2 NTs films. Specifically, the G sample has increased length reaching 19.5 μm , small internal diameter (65 nm) and an average wall thickness (25 nm). On the other hand, P-G anodization was slowed down, resulting in decreased tube length due to the use of the aged electrolyte where the highly hygroscopic ethylene glycol adsorbs a major quantity of water after 16 h of ageing [41] and the directed growth on the patterned Ti foil [42]. It is important to notice that the reference P-P samples exhibited the largest diameter (90 nm) and in combination with the voids between the tubes has had the lowest surface density, just 50 μm^{-2} .

Table 5-1. Morphological characteristics of the different TiO_2 NTs obtained by analysis of the SEM images.

Sample Electrolyte	- Length L (μm)	Internal Diameter D (nm)	Wall Thickness W (nm)	Surface Density ρ (μm^{-2})
P30 - fresh	15.3	60	10	220
P60 - aged	19.5	90	42	64
G - fresh	19.5	65	25	144
P-G - aged	15.6	75	45	68
P-P - aged	15.7	95	20	50

Based on these parameters, the porosity (P) and roughness factor (G) of the TiO_2 NT arrays were subsequently estimated using the geometrical relations [42,43].

$$\mathbf{P = 1 - [2\pi w (w + d) / \sqrt{3} (d + 2w)^2]} \quad \mathbf{(3a)}$$

$$G = [4\pi L(w + d) / \sqrt{3(d + 2w)^2}] + 1 \quad (3b)$$

The P30 and P-P samples presented the highest porosity of 60 and 54 %, which is similar to that found in nanoparticulate TiO₂ films based on commercial Evonik P25 material [44]; such values are also typical for dye-sensitized TiO₂ films. The other samples present approximately half the porosity of P30 due to the increase of their internal diameter and wall thickness. P30 and G samples also outperform in terms of the roughness factor G; this phenomenon can be rationalized in terms of the extended surface film area available for dye sensitization.

Crystal structure and mean crystalline size were further studied by performing Raman scattering analysis of all films prepared by different anodization procedures. As evidenced in **Figure 5-5**, all samples, examined after annealing and sensitization with the N719 dye for further use as DSCs photoelectrodes, were found to be in the crystalline anatase phase with corresponding main Raman peaks at approximately 142, 394, 514 and 635 cm⁻¹ (peaks marked on the figure). The mean crystalline size was obtained by fitting the strongest E_g anatase peak at 142 cm⁻¹ with a Lorentzian line and determining its frequency shift and full width at half-maximum (FWHM), in accordance to the works of A. Pottier et. al and S. Kelly et. al.[45,46] In comparison to the reference peak of nanocrystalline Degussa P25 TiO₂ film (~25 nm), the E_g presents a weak blue shift and broadening. These minor effects indicate rather weak phonon confinement effects for the NT crystallites [47] with mean crystal size of 11.9- 20.3 nm, as shown in **Table 5-2**. It is believed that the factors that affect the TiO₂ NTs crystallinity are the electrolyte composition, the anodization parameters, the thermal treatment and the final wall thickness [48]. Herein, it can be concluded that it is mainly the anodization procedure and the resulting effects on the electrolyte conductivity which determine the growth rate and finally the degree of crystallinity. The samples can be sorted in two groups. The first one concerns the samples which were prepared with fresh electrolyte in one step

anodization, (P30 and G samples). Among them, the P30 materials have the larger crystals (20.3 nm) probably due to very low growth rate (16 h) and low water content. In the second group pertain the P60, P-G, and P-P samples that were developed with aged electrolyte (with increased conductivity) and contain crystals of the same size (~12 nm).

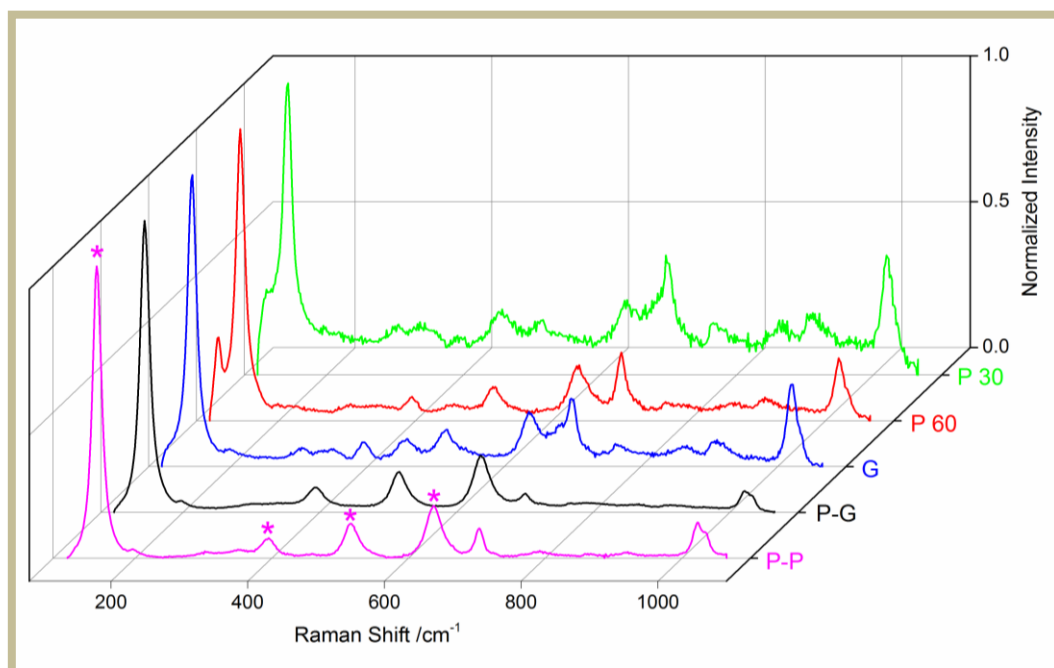


Figure 5-5. Raman spectra of P30, P60, G, P-G and P-P samples after annealing and N719 dye sensitization. TiO₂ modes are marked by stars in order to distinguish them from the N719 dye Raman (vibration) modes.

Table 5-2. Calculated morphological and structural characteristics of the TiO₂ NTs together with experimental and theoretical anodization charge σ and anodization yield. ¹ Calculated from eq. 3a and b. ² Calculated from Raman peak at 142 cm⁻¹. ³ Calculated from eq. 4.

Sample	Roughness ¹ Factor (G)	Porosity ¹ (%)	Crystal ² Size (nm)	σ_{exp} (C cm ⁻²)	σ_{th} ³ (C cm ⁻²)	Anodization Yield (%)
P30	1216	60	20.3	21.5	17.3	80.4
P60	618	33	12.4	22.8	12.1	53.2
G	964	38	17.5	22.6	13.9	61.8
P-G	500	28	11.9	22.6	8.2	36.4
P-P	720	54	12.4	22.7	13.6	59.9

The connecting feature in all those experiments is the same quantity of charge that passed during anodization. This charge was calculated from the corresponding anodization curves (**Figure 5-1**) to be $\sigma_{\text{exp}} = 22 \pm 1$ (C cm⁻²). In order to determine the anodization yield for each process, we calculated the theoretical charge σ_{th} required for the formation of Ti⁴⁺ ions within the TiO₂ NT films, based on the Faraday's law of electrolysis:

$$\sigma_{\text{th}} = m F z / M \quad (4)$$

where $F = 96,485$ C mol⁻¹ is the Faraday constant, M is the atomic mass of titanium, being 47.8671 g mol⁻¹, and $z=4$ is the valence number of Ti⁴⁺. m is the mass (in grams per cm²) of Ti inside the TiO₂ NT films estimated as: $m = (1-P) \times L \times d_{\text{anat}} \times [m_{\text{Ti}}/m_{\text{TiO}_2}]$ by taking into account the porosity P of TiO₂ in the NT films and the tube length L from **Tables 5-1** and **5-2**, the density of anatase, $d_{\text{anat}} = 3.84$ gr cm⁻³ and the fractional mass of Ti in TiO₂, $[M_{\text{Ti}}/M_{\text{TiO}_2}] \sim 0.6$. We have further assumed that all titanium is oxidized to the Ti⁴⁺ state by the anodization process and the content of other ions (F, C and H) is very low. The low voltage anodization P30 was thus found to exhibit the highest efficiency of 80 %, followed by the G, P-P and P60 processes. The most inefficient process is the two step P-G procedure, where a 36 % yield was derived. The deduced values of the process efficiency are in agreement with literature [37]. The main factor for the difference between the charge measured for the oxidation of titanium and the theoretical anodizing charge is possibly the potential drop in the electrolyte [21].

5.3.2. DSC's performance

Sensitized films of the different types of TiO₂ NTs were used for the construction of DSC devices as described in the experimental

section. Efficient sensitization of the TiO₂ NTs with the N719 dye is evidenced by resonance Raman scattering characterization of the sensitized films (shown in **Figure 5-5** and **Figure 5-6, 5-7**). Both the Raman phonon modes of TiO₂ as well as the vibrations of the N719 ruthenium complex are observed. Specifically, distinct changes in the intensity (**Figure 5-5**) of the 1022 cm⁻¹ mode, which is characteristic of the N719 dye [49], confirm differences in the amount of the adsorbed dye onto the NT photoelectrodes. Further evidence of the efficient sensitization is provided by the dye metal-to-ligand charge transfer transition (MLCT) bands of the Ru(II) polypyridyl complex in the absorbance spectra of the sensitized films (**Figure 5-7**). For the sensitized films, the main peak appears at 547 nm with a clear red shift in comparison to the corresponding MCLT band of the N719 dye in solution (535 nm) [50-52].

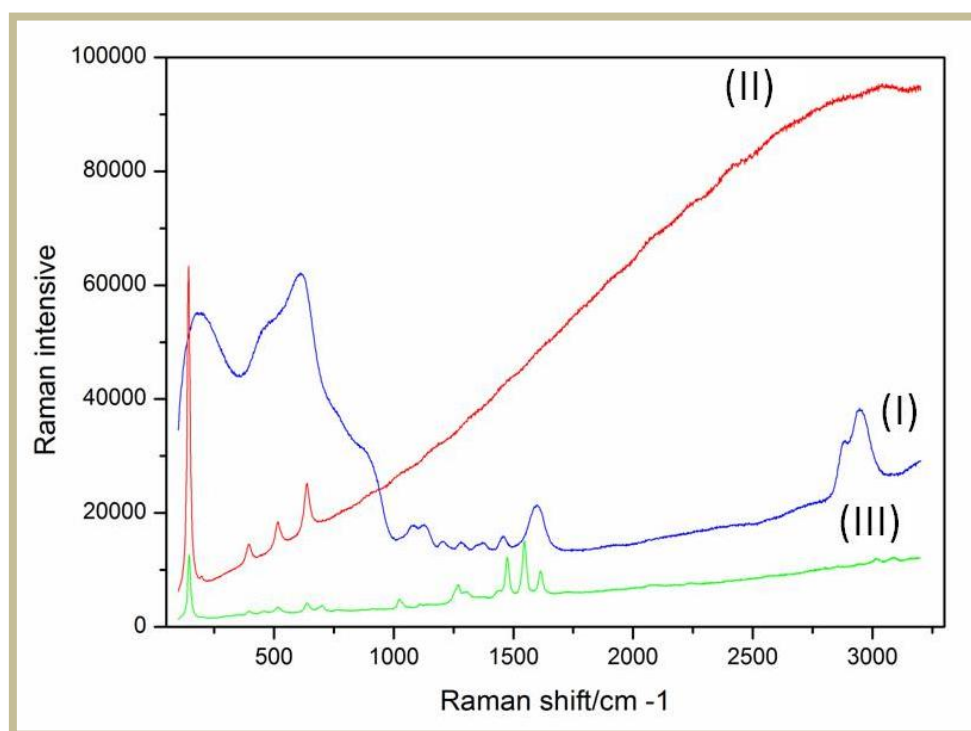


Figure 5-6. Raman spectra of P30 sample as anodized (I), after annealing (II) and after sensitization (III).

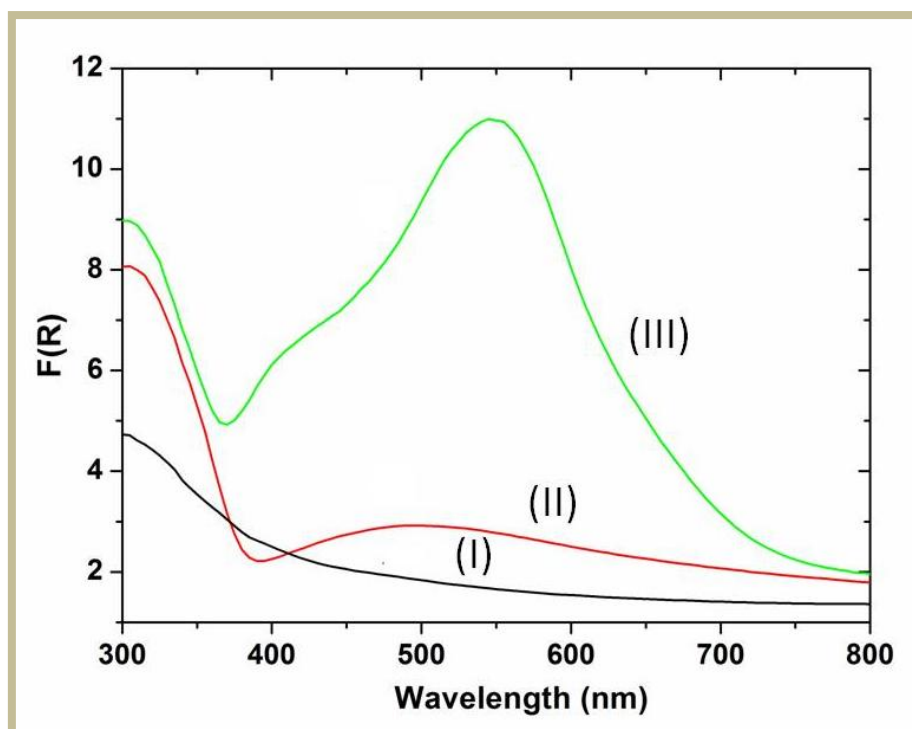


Figure 5-7. UV-Vis absorption spectra (in Kubelka Munk units) of the P30 sample: as anodized (I), after annealing (II) and after sensitization (III).

Figure 5-8 shows the J–V curves of the solar cells prepared with each one of the five anodized TiO₂ NT films and **Table 5-3** summarizes the corresponding electrical characteristics, namely the short circuit photocurrent (J_{sc}), the open circuit voltage (V_{oc}), the fill factor (FF) and the overall power conversion efficiency (η), which give comparable values for all type of cells. Both J_{sc} and V_{oc} are close to those obtained for DSCs based on nanoparticulate films and illuminated via the photoelectrode side [53]. On the contrary, the FF values are rather low as a result of high series and charge transfer resistances of the DCSs devices, due to the formation of a compact layer between the NT films and the TiO₂ foil and probably the decreased reduction rate of the redox electrolyte on the counter electrode (platinum) [54,55]. Close examination of the values in **Table 5-3** shows small, though clear, differences in the electrical parameters of the various cells that can be related to the morphological and structural characteristics of the NT photoelectrodes. In this respect, we can agree that the P30 based cells present increased FF and V_{oc} , in

agreement with Zhu et al. [56], probably due to the larger anatase crystallite size, which is responsible for the decrease of the recombination current. The J_{sc} values are relatively low despite the high values of both roughness and porosity of these films. This can be justified by the compact packing of the NTs (very high ρ) and the very small pore size, especially in the intertubes voids, which do not leave enough space for efficient electrolyte diffusion. The DSCs using the P60 sensitized photoelectrodes present higher J_{sc} compared to the corresponding P30 ones due to their higher thickness and decreased packing density. The cells prepared by the G films show the best J_{sc} among the different DSCs, as a consequence of the increased roughness factor and length, which enhance the dye loading. The P-G based cells attain moderate values of J_{sc} and V_{oc} and the worst FF probably due to the combination of low particle size, roughness and porosity. Lastly, the P-P reference cells present the lowest efficiency. This is due to the NTs large internal diameter and the existence of inter-tubular voids leading to low surface density and increased porosity, which in combination with poor sensitization (decreased mode of 1022 cm^{-1} in **Figure 5-5**) and the small crystals size can justify the lower performance of the corresponding DSCs. Additionally, this is further supported by the electron lifetimes measured for each cell via the IMVS technique [57] and presented in **Figure 5-9**. In fact, a clear correlation comes out highlighting the significance of the choice of the anodization process; the potentiostatically prepared samples at the high voltage of 60 V (P 60 and P-P), have the smallest electron lifetime (or the highest electron recombination) and show similar behavior likewise, the galvanostatically prepared samples (G, P-G) presenting much more extended electron life times values than the potentiostatic samples. On the contrary, the P30 based cells display a moderate recombination time in relation with the P60, P-P and G, P-G cells.

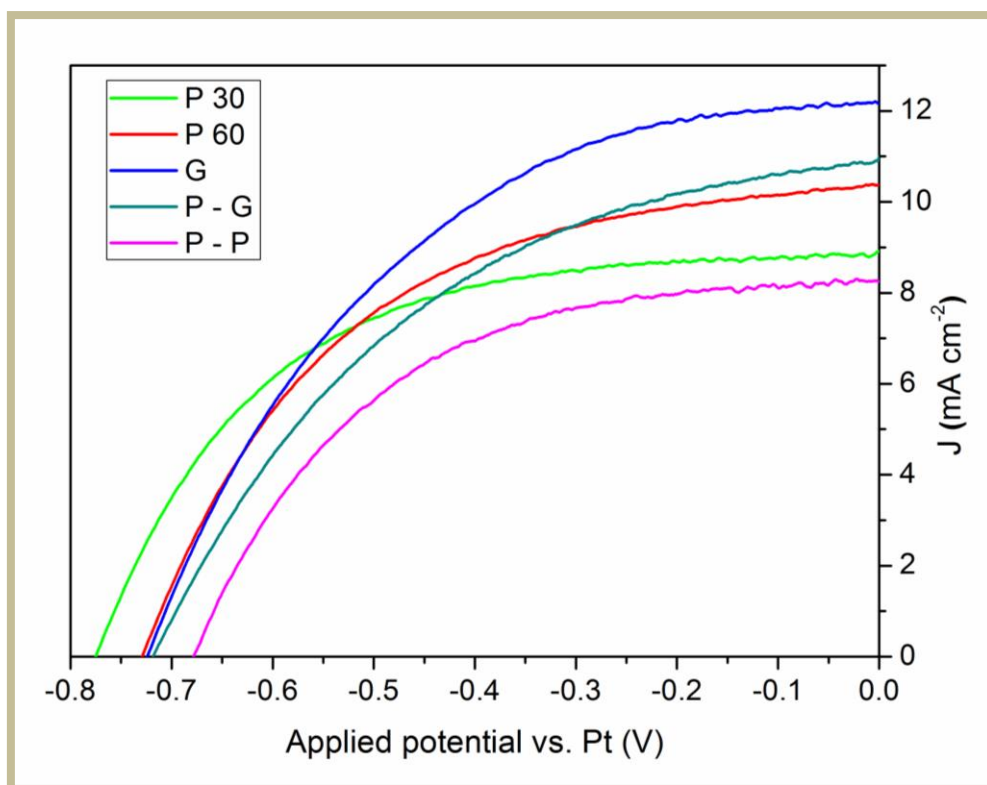


Figure 5-8. J-V characteristic curves of back-illuminated (1 sun, AM1.5G) DSCs, using the prepared nanotubular samples as photoelectrodes.

Table 5-3. Electrical parameters of the DSCs constructed with various anodized NT films.

Sample	J_{sc} (mA cm ⁻²)	V_{oc} (mV)	FF	η (%)
P30	8.92	774	0.55	3.79
P60	10.37	728	0.50	3.78
G	12.15	723	0.46	4.12
P-G	10.67	719	0.43	3.67
P-P	8.24	678	0.52	2.90

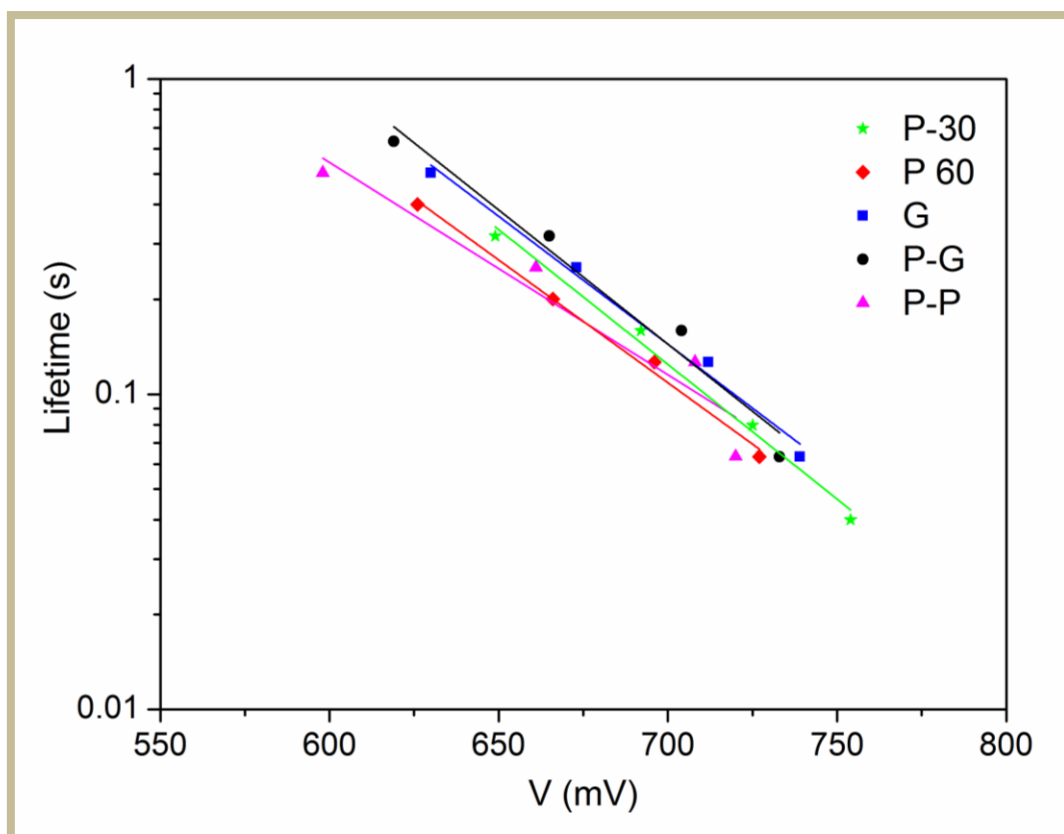


Figure 5-9. Electron lifetimes (τ) of the different DSCs plotted vs. the photovoltage (V), for various light intensities (1 - 0.1 Suns).

Summarizing the performance of the different sensitized films as photoelectrodes in DSCs, we can conclude that they present comparable behavior with small deviations in the overall efficiency. This suggests that the consumed charge during anodization, which is kept constant for all films, may play a decisive role in the efficiency of the corresponding solar cell devices. Among the different films, the galvanostatically prepared ones present the optimum morphology (open structure, highest length) in regard to its function as an effective DSC photoelectrode. Thus, the corresponding cells exhibit superior electrical characteristics J_{sc} , V_{oc} and η . However, the FF remains rather low, a drawback that may be effectively alleviated by appropriate $TiCl_4$ post treatment [58].

5.4. Conclusion

Anodic titania nanotube arrays were prepared with constant charge consumed during anodization by applying five different electrochemical approaches: potentiostatic anodization at 30 V and 60 V, galvanostatic anodization at 3.15 mA/cm², and combined two step potentiostatic – galvanostatic and potentiostatic – potentiostatic methods. The vertically oriented TiO₂ nanotubular films presented distinct differences in their morphology and crystalline structure as a result of the modifications in the applied anodization steps and the control of the electrolyte conductivity by the extensive ageing. Among the different methods, our novel approach of combining galvanostatic NTs growth on a patterned Ti foil, prepared following standar potentiostatic conditions, ensured the best uniformity of the nanotubular films and clean top surface without nanograss or cracks over extended lateral scale. The diverse morphological and structural characteristics of the different TiO₂ NTs were found to sensitively influence their electrical characteristics when used as DSC photoelectrodes; the galvanostatic NTs presenting the most favorable and open structure. However, despite the underlying differences, the TiO₂ NT photoelectrodes exhibited comparable photovoltaic efficiencies. This similarity in the DSCs electrical performance, irrespectively of the TiO₂ NT films used as photoelectrodes, relates well to the constant integrated charge during the anodization process.

5.5. References

1. G. K. Mor, O. K. Varghese, M. Paulose, K. Shankar, C. A. Grimes “A review on highly ordered, vertically oriented TiO₂ nanotube arrays: Fabrication, material properties, and solar energy applications” Sol. Energ. Mat. Sol. C 90 (2006) 2011.
2. J.M. Macak, H. Tsuchiya, A. Ghicov, K. Yasuda, R. Hahn, S. Bauer, P. Schmuki “TiO₂ nanotubes: Self-organized electrochemical

- formation, properties and applications” *Curr. Opin. Solid St. M.* 11 (2007) 3.
3. M. Assefpour-Dezfuly, C. Vlachos, E. H. Andrews “Oxide morphology and adhesive bonding on titanium surfaces” *J. Mater. Sci.* 19 (1984) 3626.
 4. P. Roy, S. P. Albu, P. Schmuki “TiO₂ nanotubes in dye-sensitized solar cells: Higher efficiencies by well-defined tube tops” *Electrochem. Commun.* 12 (2010) 949.
 5. K. Shankar, G. K. Mor, H. E. Prakasam, S. Yoriya, M. Paulose, O. K Varghese, C. A. Grimes “Highly-ordered TiO₂ nanotube arrays up to 220 μ m in length: use in water photoelectrolysis and dye-sensitized solar cells” *Nanotechnology* 18 (2007) 065707.
 6. L. L. Li, C. Y. Tsai, H. P. Wu, C. C. Chen, E. W. G. Diau “Fabrication of long TiO₂ nanotube arrays in a short time using a hybrid anodic method for highly efficient dye-sensitized solar cells” *J. Mater. Chem.* 20 (2010) 2753.
 7. T. Stergiopoulos, V. Likodimos, R. Hahn, P. Schmuki, P. Falaras “Front-side illuminated dye-sensitized solar cells based on bundle shaped titania nanotube membranes” *Phys. Status Solidi. A* 209 (2012) 193.
 8. T. Stergiopoulos, Evangelia Rozi, R. Hahn, P. Schmuki, P. Falaras “Enhanced Open-Circuit Photopotential in Quasi-Solid-State Dye-Sensitized Solar Cells Based on Polymer Redox Electrolytes Filled with Anodic Titania Nanotubes” *Adv. Energy Mater.* 1 (2011) 569.
 9. Q. Zhang, G. Cao “Nanostructured photoelectrodes for dye-sensitized solar cells” *Nano. Today* 6 (2011) 91.
 10. P. Roy, D. Kim, K. Lee, E. Spiecker, P. Schmuki “TiO₂ nanotubes and their application in dye-sensitized solar cells” *Nanoscale* 2 (2010) 45.
 11. L. Sun, S. Zhang, X. Sun, X. He “Effect of the geometry of the anodized titania nanotube array on the performance of dye-sensitized solar cells” *J. Nanosci. Nanotechnol.* 10 (2010) 4551.

12. V. Likodimos, T. Stergiopoulos, P. Falaras, J. Kunze, P. Schmuki "Phase Composition, Size, Orientation, and Antenna Effects of Self-Assembled Anodized Titania Nanotube Arrays: A Polarized Micro-Raman Investigation" *J. Phys. Chem. C* 112 (2008) 12687.
13. J. Y. Kim, J. H. Noh, K. Zhu, A. F. Halverson, N. R. Neale, S. Park, K. S. Hong, J. Frank "General Strategy for Fabricating Transparent TiO₂ Nanotube Arrays for Dye-Sensitized Photoelectrodes: Illumination Geometry and Transport Properties" *ACS Nano* 5 (2011) 2647.
14. C. C. Chen, H. W. Chung, C. H. Chen, H. P. Lu, C. M. Lan, S. F. Chen, L. Luo, C. S. Hung, E. W. G. Diau "Fabrication and Characterization of Anodic Titanium Oxide Nanotube Arrays of Controlled Length for Highly Efficient Dye-Sensitized Solar Cells" *J. Phys. Chem. C* 112 (2008) 19151.
15. Q. Zheng, H. Kang, J. Yun, J. Lee, J. H. Park, S. Baik "Hierarchical construction of self-standing anodized titania nanotube arrays and nanoparticles for efficient and cost-effective front-illuminated dye-sensitized solar cells" *ACS Nano* 5 (2011) 5088.
16. A. Valota, M. Curioni, D. J. Leclerc, P. Skeldon, P. Falaras, G. E. Thompson "Influence of applied potential on titanium oxide nanotube growth" *J. Electrochem. Soc.* 157 (2010) K243.
17. J. Yan, F. Zhou "TiO₂ nanotubes: Structure optimization for solar cells" *J. Mater. Chem.* 21 (2011) 9406.
18. A. Ghicov, S. A. Albu, R. Hahn, D. Kim, T. Stergiopoulos, J. Kunze, C. A. Schiller, P. Falaras, P. Schmuki "TiO₂ Nanotubes in Dye-Sensitized Solar Cells: Critical Factors for the Conversion Efficiency" *Chem. Asian J.* 4 (2009) 520.
19. L. V. Taveira, J. M. Macak, K. Sirotna, L. F. P. Dick, P. Schmuki "Voltage Oscillations and Morphology during the Galvanostatic Formation of Self-Organized TiO₂ Nanotubes" *J. Electrochem. Soc.* 153 (2006) B137.
20. H. Habazaki, Y. Konno, Y. Aoki, P. Skeldon, G. E. Thompson "Galvanostatic Growth of Nanoporous Anodic Films on Iron in

Ammonium Fluoride–Ethylene Glycol Electrolytes with Different Water Contents” *J. Phys. Chem. C* 114 (2010) 18853.

21. T. Stergiopoulos, A. Valota, V. Likodimos, T. Speliotis, D. Niarchos, P. Skeldon, G. E. Thompson, P. Falaras “Dye-sensitization of self-assembled titania nanotubes prepared by galvanostatic anodization of Ti sputtered on conductive glass” *Nanotechnology* 20 (2009) 365601.

22. V. Galstyan, A. Vomiero, E. Comini, G. Faglia, G. Sberveglieri “TiO₂ nanotubular and nanoporous arrays by electrochemical anodization on different substrates” *RSC Adv.* 1 (2011) 1038.

23. S. Li, G. Zhang, D. Guo, L. Yu, W. Zhang “Anodization Fabrication of Highly Ordered TiO₂ Nanotubes” *J. Phys. Chem. C* 113 (2009) 12759.

24. Y. Shin, S. Lee “Self-Organized Regular Arrays of Anodic TiO₂ Nanotubes” *Nano Lett.* 8 (2008) 3171.

25. D. Wang, B. Yu, C. Wang, F. Zhou, W. Liu “A Novel Protocol Toward Perfect Alignment of Anodized TiO₂ Nanotubes” *Adv. Mater.* 21 (2009) 1964.

26. D. Li, P. C. Chang, C. J. Chien, J. G. Lu “Applications of Tunable TiO₂ Nanotubes as Nanotemplate and Photovoltaic Device” *Chem. Mater.* 22 (2010) 5707.

27. B. Chen, K. Lu, J. A. Geldmeier “Highly ordered titania nanotube arrays with square, triangular, and sunflower structures” *Chem. Commun.* 47 (2011) 10085.

28. B. Chen, K. Lu “Influence of Patterned Concave Depth and Surface Curvature on Anodization of Titania Nanotubes and Alumina Nanopores” *Langmuir* 27 (2011) 12179.

29. W. Zhu, X. Liu, H. Liu, D. Tong, J. Yang, J. Peng “An efficient approach to control the morphology and the adhesion properties of anodized TiO₂ nanotube arrays for improved photoconversion efficiency” *Electrochim. Acta* 56 (2011) 2618.

30. N. Vaenas, T. Stergiopoulos , A. G. Kontos, V. Likodimos, N. Boukos, P. Falaras “Sensitizer activated solar cells based on self-organized TiO₂ nanotubes” *Microelectronic Engineering* 90 (2012) 62.
31. K. Yasuda, J. M. Macak, S. Berger, A. Ghicov, P. Schmuki “Mechanistic Aspects of the Self-Organization Process for Oxide Nanotube Formation on Valve Metals” *J. Electrochem. Soc.* 154 (2007) C472.
32. J.M. Macak, H. Hildebrand, U. M. Jahns, P. Schmuki “Mechanistic aspects and growth of large diameter self-organized TiO₂ nanotubes” *J. Electroanal. Chem.* 621 (2008) 254.
33. S. P. Albu, D. Kim, P. Schmuki “Growth of Aligned TiO₂ Bamboo-Type Nanotubes and Highly Ordered Nanolace” *Angew. Chem. Int. Ed.* 47 (2008) 1916.
34. P. Roy, D. Kim, I. Paramasivam, P. Schmuki “Improved efficiency of TiO₂ nanotubes in dye sensitized solar cells by decoration with TiO₂ nanoparticles” *Electrochem. Commun.* 11 (2009) 1001.
35. R. S. Tovar, I. Paramasivam, K. Lee, P. Schmuki “Influence of hydrodynamic conditions on growth and geometry of anodic TiO₂ nanotubes and their use towards optimized DSSCs” *J. Mater. Chem.* 22 (2012) 12792.
36. D. Kim, A. Ghicov, P. Schmuki “TiO₂ Nanotube arrays: Elimination of disordered top layers (“nanograss”) for improved photoconversion efficiency in dye-sensitized solar cells” *Electrochem. Comm.* 10 (2008) 1835.
37. A. Valota, D. J. LeClere, T. Hashimoto, P. Skeldon, G. E. Thompson¹, S. Berger, J. Kunze, P. Schmuki “The efficiency of nanotube formation on titanium anodized under voltage and current control in fluoride/glycerol electrolyte” *Nanotechnology* 19 (2008) 355701.
38. J. M. Macak, S. P. Albu, P. Schmuki “Towards ideal hexagonal self-ordering of TiO₂ nanotubes” *Phys. Stat. Sol. (RRL)* 1, 5 (2007) 181.
39. S. P. Albu, A. Ghicov, J. M. Macak, R. Hahn, P. Schmuki, *Nano Lett.* 7 (2007) 1286.

40. K. Lu, Z. Tian, J. A. Geldmeier "Polishing effect on anodic titania nanotube formation" *Electrochim. Acta* 56 (2011) 6014.
41. A. Valota, D.J. LeClere, P. Skeldon, M. Curioni, T. Hashimoto, S. Berger, J. Kunze, P. Schmuki, G.E. Thompson "Influence of water content on nanotubular anodic titania formed in fluoride/glycerol electrolytes" *Electrochim. Acta* 54 (2009) 4321.
42. K. Zhu, N. R. Neale, A. Miedane, J. Frank "Enhanced Charge-Collection Efficiencies and Light Scattering in Dye-Sensitized Solar Cells Using Oriented TiO₂ Nanotubes Arrays" *Nano Lett.* 7 (2007) 69.
43. A.G. Kontos, A. Katsanaki, T. Maggos, V. Likodimos, A. Ghicov, D. Kim, J. Kunze, C. Vasilakos, P. Schmuki, P. Falaras "Photocatalytic degradation of gas pollutants on self-assembled titania nanotubes" *Chem Phys. Lett.* 490 (2010) 58.
44. H. Lindstrom, E. Magnusson, A. Holmberg, S. Sodergren, S. E. Lindquist, A. Hagfeldt "A new method for manufacturing nanostructured electrodes on glass substrates" *Sol. Energ. Mat. Sol.* 73 (2002) 91.
45. A. Pottier, S. Cassaignon, C. Chaneac, F. Villain, E. Tronc, J. P. Jolivet "Size tailoring of TiO₂ anatase nanoparticles in aqueous medium and synthesis of nanocomposites. Characterization by Raman spectroscopy" *J. Mater. Chem.* 13 (2003) 877.
46. S. Kelly, F. H. Pollak, M. Tomkiewicz "Raman Spectroscopy as a Morphological Probe for TiO₂ Aerogels" *J. Phys. Chem. B* 101 (1997) 2730.
47. D. Fang, Z. Luo, K. Huang, D. C. Lagoudas "Effect of heat treatment on morphology, crystalline structure and photocatalysis properties of TiO₂ nanotubes on Ti substrate and freestanding membrane" *Appl Surf Sci.* 257 (2011) 6451.
48. K. Zhu, N. R. Neale, A. F. Halverson, J. Y. Kim, A. J. Frank "Effects of Annealing Temperature on the Charge-Collection and Light-Harvesting Properties of TiO₂ Nanotube-Based Dye-Sensitized Solar Cells" *J. Phys. Chem. C* 114 (2010) 13433.

49. V. Likodimos, T. Stergiopoulos, P. Falaras, R. Harikisun, J. Desilvestro, G. Tulloch "Prolonged Light and Thermal Stress Effects on Industrial Dye-Sensitized Solar Cells: A Micro-Raman Investigation on the Long-Term Stability of Aged Cells" *J. Phys. Chem. C* 113 (2009) 9412.
50. N. Hirata, J. J. Lagref, E. J. Palomares, J.R. Durrant, M.K. Nazeeruddin, M. Gratzel, D. D. Censo "Supramolecular Control of Charge-Transfer Dynamics on Dye-sensitized Nanocrystalline TiO₂ Films" *Chem. Eur. J.* 10 (2004) 595.
51. G. Konti, E. Chatzivasiloglou, V. Likodimos, G. Kantonis, A.G. Kontos, A.I. Philippopoulos, P. Falaras "Influence of pyridine ligand nature and the corresponding ruthenium(II) dye molecular structure on the performance of dye-sensitized solar cells" *Photochem. Photobiol. Sci.* 8 (2009) 726.
52. C. Bauer, G. Boschloo, E. Mukhtar, A. Hagfeldt "Interfacial Electron-Transfer Dynamics in Ru(tcterpy)(NCS)₃-Sensitized TiO₂ Nanocrystalline Solar Cells" *J. Phys. Chem. B* 106 (2002) 12693.
53. T. Stergiopoulos, A. G. Kontos, V. Likodimos, D. Perganti, P. Falaras "Solvent Effects at the Photoelectrode/Electrolyte Interface of a DSC: A Combined Spectroscopic and Photoelectrochemical Study" *J. Phys. Chem. C* 115 (2011) 10236.
54. A. Tighineanu, T. Ruff, S. Albu, R. Hahn, P. Schmuki "Conductivity of TiO₂ nanotubes: Influence of annealing time and temperature" *Chem. Phys. Lett.* 494 (2010) 260.
55. C. C. Chen, W. C. Say, S. J. Hsien, E. W. G. Diau "A mechanism for the formation of annealed compact oxide layers at the interface between anodic titania nanotube arrays and Ti foil" *Appl. Phys. A* 95 (2009) 889.
56. K. Zhu, N. Kopidakis, N. R. Neale, J. Lagemaat, A. J. Frank "Influence of surface area on charge transport and recombination in dye-sensitized TiO₂ solar cells" *J. Phys. Chem. B* 110 (2006) 25174.

57. K. Zhu, N. T. Neale, A. Miedaner, A. J. Frank "Enhanced Charge-Collection Efficiencies and Light Scattering in Dye-Sensitized Solar Cells Using Oriented TiO₂ Nanotubes Arrays" Nano Lett. 7 (2007) 69
58. M. Ye, X. Xin, C. Lin, Z. Lin "High Efficiency Dye-Sensitized Solar Cells Based on Hierarchically Structured Nanotubes" NanoLett. 11 (2011) 3214.

Chapter 6. TiO₂ nanotubes-based dye solar cells employing a Co²⁺/Co³⁺ electrolyte: understanding charge recombination and interfacial energetics

Alternative redox shuttles with more positive (than standard I⁻/I³⁻ couple) Nernst electrochemical potential such as Co²⁺/Co³⁺ have been recently applied in dye solar cells (DSCs) delivering significantly enhanced open-circuit photovoltages (V_{oc}), the main impediment for these systems to achieve overall breakthrough conversion efficiencies are mass transport limitations due to the large molecular size of cobalt complexes. In this work, we employed the cobalt redox shuttle in combination with titania nanotube arrays as a highly porous photoelectrode to facilitate electrolyte diffusion and a surface-blocking triphenylamine-based dye D35 to replace standard ruthenium complexes such as the Z907 dye. Therefore, while Z907-based solar cells delivered V_{oc} values of about 0.6 V, an open-circuit photovoltage higher than 0.8 V was attained by the use of D35 dye, exploiting the actual potential of the cobalt-based couple. Extensive comparative investigations of the electrical characteristics of the DSCs, especially by Electrochemical Impedance Spectroscopy (EIS), were realized in order to understand the mechanism behind the different photovoltaic behavior of the above cells; DSCs based on the I⁻/I³⁻ couple were also investigated as a reference. An upward TiO₂ conduction band-edge shift related to the D35 dipole moment orientation together with significantly reduced recombination were identified to underlie the V_{oc} increase, while non-linear recombination was found to be the most dominant parameter affecting V_{oc} and fill factor of the solar cells based on the TiO₂ nanotubes and the Co²⁺/Co³⁺ redox mediator.

6.1. Introduction

Dye solar cells (DSCs) [1] as third generation photovoltaics (PVs) represent a good alternative to the well-established crystalline silicon devices or the highly efficient thin-film solar cells (such as GaAs) [2] as they are solution processable, and thus ideal to incorporate into roll-to-roll production lines, promising low cost and relative ease of fabrication [3].

From the first pioneering publication by Grätzel and O'Regan in 1991 [4] until very recently, the highest DSC's efficiencies [5] have been achieved by using the I^-/I_3^- redox couple that permits fast regeneration of the dye, good diffusivity in the TiO_2 mesopores and most importantly low charge recombination [6]. Nevertheless, the dye regeneration process consumes more than 0.5 V as a driving force, something which restricts the photovoltage at an upper threshold of about 0.75-0.80 V [7]. Moreover, the increased light absorption (yellow colour) and corrosive nature of the iodide/triiodide (I^-/I_3^-) redox couple provide additional disadvantages for its efficient use in DSCs [8]. In order to deal with these issues, new electron redox mediators have been recently developed [9-12], the most prominent alternative being the Co^{2+}/Co^{3+} redox shuttle. This mediator presents reduced absorbance in the visible light, non corrosive behavior towards the metallic counter electrode and it also has a more positive standard redox potential of about 200 mV than that of the I^-/I_3^- redox couple [13], partially alleviating the potential mismatch between the dye and the redox couple that limits the open circuit voltage of DSCs based on iodide/triiodide mediators.

Very recently, a record efficiency of 12.3 % was reported on mesoscopic solar cells using a donor- π -bridge-acceptor zinc porphyrin dye (designated YD2-*o*-C8) with another organic dye as sensitizers (co-sensitization) that incorporate a Co^{2+}/Co^{3+} tris(bipyridyl)-based redox electrolyte [14]. Since then, great effort has been devoted by scientists

involved in the field in order, first, to understand regeneration and recombination kinetics [15,16] and then to ameliorate the current state-of-the-art performance by controlling the molecular engineering of dyes [17-19], incorporating different co-adsorbents or additives to minimize recombination processes [20-23] or employing alternative effective cathodes with minimum overpotential for Co^{3+} reduction [24,25]. Quite lately, work on the stability of the above system has also been carried out [26-28].

Nevertheless, the cobalt-based electrolytes encounter serious diffusivity problems, due to their large size and heavier mass [29]. In order to overcome this drawback, some attempts have been recently devoted to enhance and tune the mesoporous characteristics of the TiO_2 photoanode [30]. For instance, J. Y. Kim et al. [31] have tried to improve the infiltration of the cobalt redox electrolyte into the photoelectrode by replacing the TiO_2 nanoparticulate film with nanotube arrays. Apart from the enlarged pore size and porosity, this “open” morphology may afford a direct path for fast electron transport [32], reduced charge recombination [33] and effective light scattering properties [34-36]. The use of the Ru^{2+} -based N719 dye in back-side illuminated DSCs lead to relatively low photovoltage values (no more than 0.6 V), despite the highly positive Nernst potential of the cobalt redox couple. However, since N719 dye is not compatible with cobalt-based electrolytes like pure organic [37] or cyclometalated Ru^{2+} dyes [38], the obtained conclusions drawn from this work could not apply for a system which works sufficiently well.

To this end, this chapter is focused on highly porous photoelectrodes consisting of vertically aligned anodic titania nanotubes permitting easier penetration of cobalt electrolyte [39], but now in combination with a state-of-the-art triphenylamine-based organic dye (namely D35, **Figure 6-1**). This donor- π -acceptor dye, besides high absorption coefficients (more than $30000 \text{ M}^{-1} \text{ cm}^{-1}$ at 445 nm) may produce very large open-circuit photopotentials (V_{oc}) due to the insulating properties of the butoxy chains through steric

hindrance [37], when suitably combined with a cobalt mediator in front-side illuminated DSCs [40]. However, D35 was never investigated in conjunction with a substrate that could potentially exclude mass transport limitations for the cobalt shuttle. In this work, in order to profoundly understand charge recombination and interfacial energetics, the properties of D35-based DSCs were directly compared with those employing standard ruthenium complexes such as the commercially available Z907 (**Figure 6-1**) as well as with similar cells using the reference I⁻/I₃⁻ shuttle. It was thus found that while Z907 dyes-based solar cells with liquid [Co(bpy)₃]^{2+/3+} electrolyte (**Figure 6-1**) delivered moderate V_{oc} values (not higher than 0.6 V), an open-circuit photovoltage higher than 0.8 V was attained for D35, taking real advantage of the highly positive redox potential of the cobalt-based couple. In fact, despite its insulating properties, the D35 alone could not provide a high V_{oc} when combined with the standard I⁻/I₃⁻ shuttle. Detailed comparative analysis of the DSC electrical characteristics investigated by Electrochemical Impedance Spectroscopy (EIS) revealed that positive TiO₂ conduction band-edge shift and reduced recombination are at the origin of the higher photovoltage gained by the D35 dye combined with the Co²⁺/Co³⁺ couple, confirming in parallel that non-linear recombination dynamics are the most dominant parameter affecting V_{oc} and FF of the solar cells.

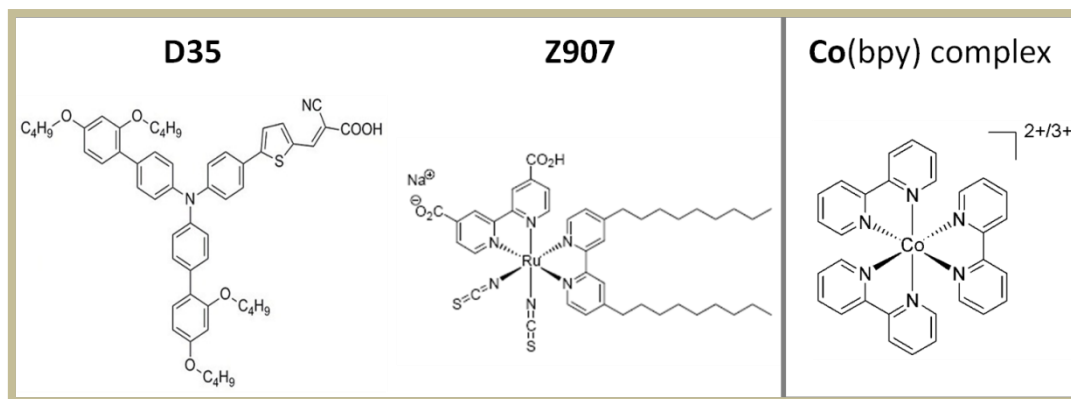


Figure 6-1. Molecular structures of the D35 and Z907 dyes as well as of the cobalt(II)/(III) tris(2,2'-bipyridine) complex, utilized in the present study.

6.2. Experimental

6.2.1. Materials

Titanium foils were purchased from Sigma Aldrich (0.25 mm, 99.7 % purity). The D35 organic dye and the cobalt-based electrolyte were purchased from Dyenamo AB (Sweden) while the Z907 and N719 dyes were obtained from Dyesol Ltd. The cobalt-based electrolyte accordingly contains 0.22 M $[\text{Co}(\text{bpy})_3(\text{PF}_6)_2]$, 0.033 M $[\text{Co}(\text{bpy})_3(\text{PF}_6)_3]$ where bpy stands for tris(2,2'-bipyridine), 0.1 M LiClO_4 and 0.2 M 4-tert-butylpyridine (TBP) dissolved in 3-methoxypropionitrile (MPN). As a reference, a highly efficient iodide/triiodide based electrolyte was prepared containing 1 M dimethylimidazolium iodide, 0.05 M LiI , 0.015 M I_2 , 0.5 M TBP and 0.1 M guanidinium thiocyanate in acetonitrile/valeronitrile 85:15 (v/v).

6.2.2. TiO_2 nanotubes development

Titanium foils (2 cm x 2 cm in size) with a working area of 1.32 cm^2 were used as substrates for the experiments. First, the Ti foils were ultrasonicated in acetone, isopropanol and methanol for 10 min,

then washed with deionized (D.I.) water and dried under nitrogen stream. Anodization was carried out in a Teflon electrochemical cell by applying a constant density current of 3 mA cm^{-2} between the anode (Ti foil) and a Pt mesh cathode, the distance between the electrodes set up at 2 cm. The duration of the galvanostatic oxidation was fixed at 2 h and all the experiments took place at room temperature. The electrolyte solution consisted of 0.3 wt % NH_4F (95 %, Janssen Chimica) in ethylene glycol (99.5%, Merck) and a small amount (2 vol %) of D.I. water. The anodized films were rinsed with D.I. water and left to dry in air. After anodization, the samples were annealed at 450°C for 1 h, with a heating rate of 5°C min^{-1} in order to crystallize into the anatase phase.

6.2.3. Solar cell assembly

The annealed TiO_2 NTs films were immersed in D35 (0.2 mM in ethanolic solution) for 1 day. As a reference, TiO_2 nanotubes were also sensitized by the Z907 or N719 dye (0.3 mM in acetonitrile/tert-butanol 1/1 solution). DSCs were constructed by casting a drop of cobalt or iodine-based electrolyte onto the photoelectrode and sandwiching against a highly transparent Pt counter electrode (fabricated by sputtering). All DSCs had an active area of 0.25 cm^2 . Cells are denoted as D35/Co, Z907/Co, D35/I and Z907/I with respect to the combination of the dye-electrolyte used.

6.2.4. Instrumentation

The absorbance (UV-vis) spectra of the sensitized nanotubular films were determined by recording the corresponding diffuse reflectance spectra on a Hitachi 3010 spectrophotometer, equipped with a 60 mm integrating sphere. The morphology of the NT samples

was characterized using a PHILIPS Quanta Inspect scanning electron microscope (SEM), while their phase composition was investigated by micro-Raman spectroscopy on a Renishaw in Via Reflex spectrometer using an Ar⁺ ion laser ($\lambda=514.5$ nm) as excitation source. Current density-voltage (J-V) measurements were recorded by illuminating the DSCs under simulated solar light (1 sun, 1000 W m⁻²) from a 300 W Xe source in combination with AM 1.5G optical filters (Oriel). The illuminated area of the DSCs was set at 0.15 cm², using a large black mask in front of the cells. The J-V characteristics (under dark and light conditions) were recorded using linear sweep voltammetry on the Autolab potentiostat working in a 2-electrode mode at a scan rate of 50 mV s⁻¹. Electrochemical impedance (EIS) measurements were performed under dark in a potential window from -0.3 to -0.8 V, while electron lifetimes at variable light intensities were determined by Intensity-Modulated Photovoltage Spectroscopy (IMVS) using the same system (Autolab). For this purpose a sinusoidally modulated light beam of a red (625 nm) light emitting diode was used.

6.3. Results and Discussion

6.3.1. Morphology-structure and sensitization of the TiO₂ nanotubes

Figure 6-2 (a) shows characteristic SEM images of the as-grown NTs; some unintentionally formed debris, appeared at the surface, and obviously remained after the anodization process [41]. The length of the tubes was controlled by the anodization duration and was selected to be close to the optimum thickness (20 ± 5 μm as shown in inset of **Figure 6-2** (a)) for nanotubular photoelectrodes of highly efficient DSCs [42]. The growth rate under the applied current density of 3 mA cm⁻² has been estimated at 10 μm per h. The second inset,

depicting a magnification of the top area, clearly shows the presence of tube arrays, interconnected with a distinct intertube spacing, having a mean internal pore diameter of 60 nm with a wall thickness of 25 nm (estimating the NT's external diameter to be at about 110 nm). The tubes are parallel to each other and vertically oriented to the metal substrate, creating a potentially ideal pathway for electrolyte diffusion **Figure 6-2** (b); on the contrary, we could hypothesize that the structure of standard nanoparticulate films may hinder electrolyte infiltration, especially when the contained redox couple consists of massive species with large ionic radius like the $[\text{Co}(\text{bpy})_3]^{2+/3+}$ complexes.

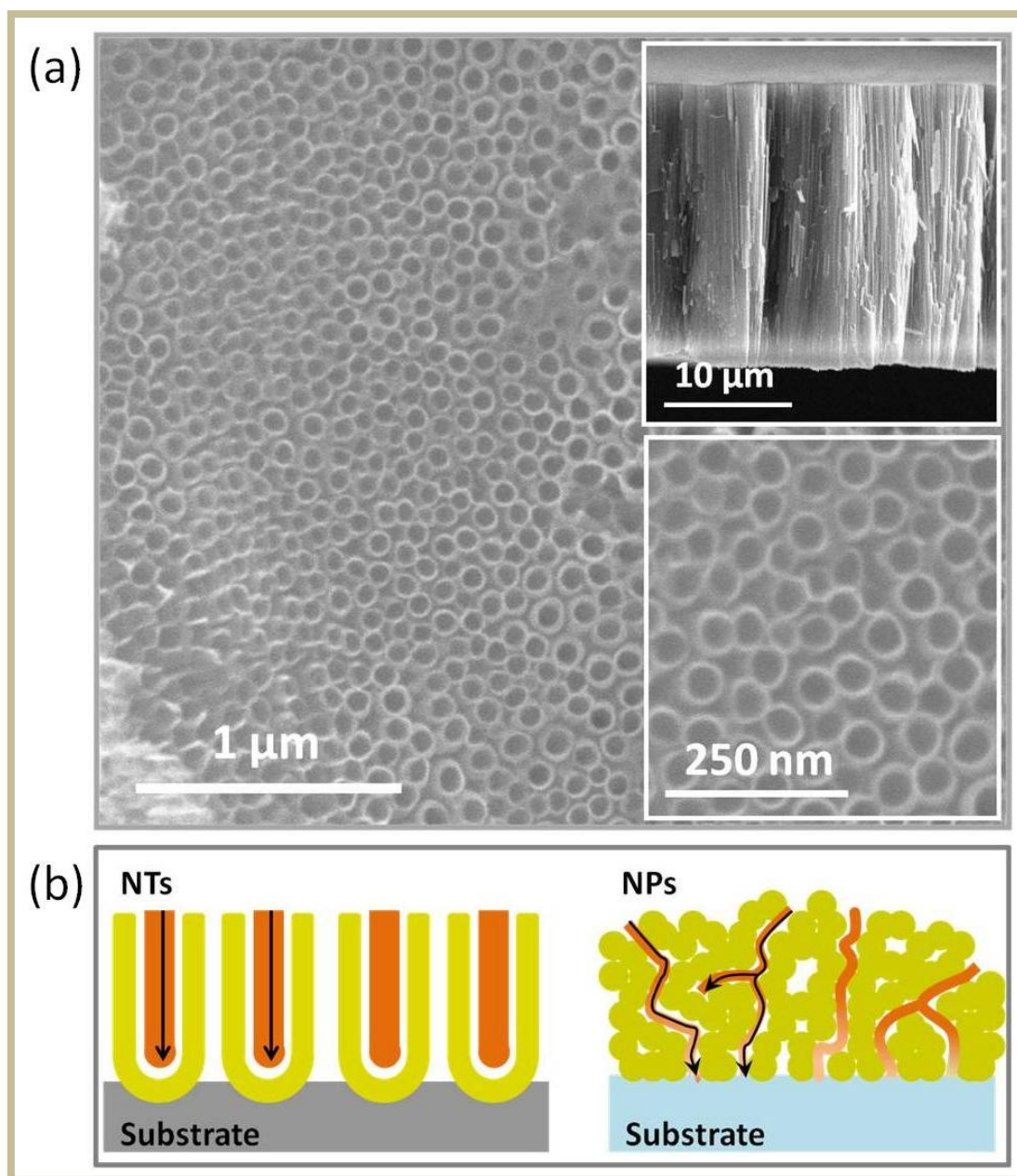


Figure 6-2. (a) Characteristic SEM images of the nanotubular film top surface. In the inset, a magnified top image and a cross section of the film are shown; (b) Graphical representation of the probable unrestricted electrolyte diffusion through the nanotubular film (left figure) and the problematic infiltration into the nanoparticulate film (right).

Micro-Raman measurements showed that after annealing at 450 °C for 1 h the as-grown NTs crystallized into the anatase TiO_2 phase, while some rutile traces were identified at the interface between the metal substrate and the tubes' bottom (**Figure 6-3**). Then, the electrodes were sensitized by the organic D35 and the Ru^{2+} -based Z907 dyes. The normalized absorption spectra of the sensitized

nanotubes (**Figure 6-4**) verified the different optical density of the two dyes. In particular, the Z907 sensitized TiO₂ NTs presented extended absorbance in the NIR range compared with the D35 one, and thus a higher photocurrent by the Z907 is anticipated.

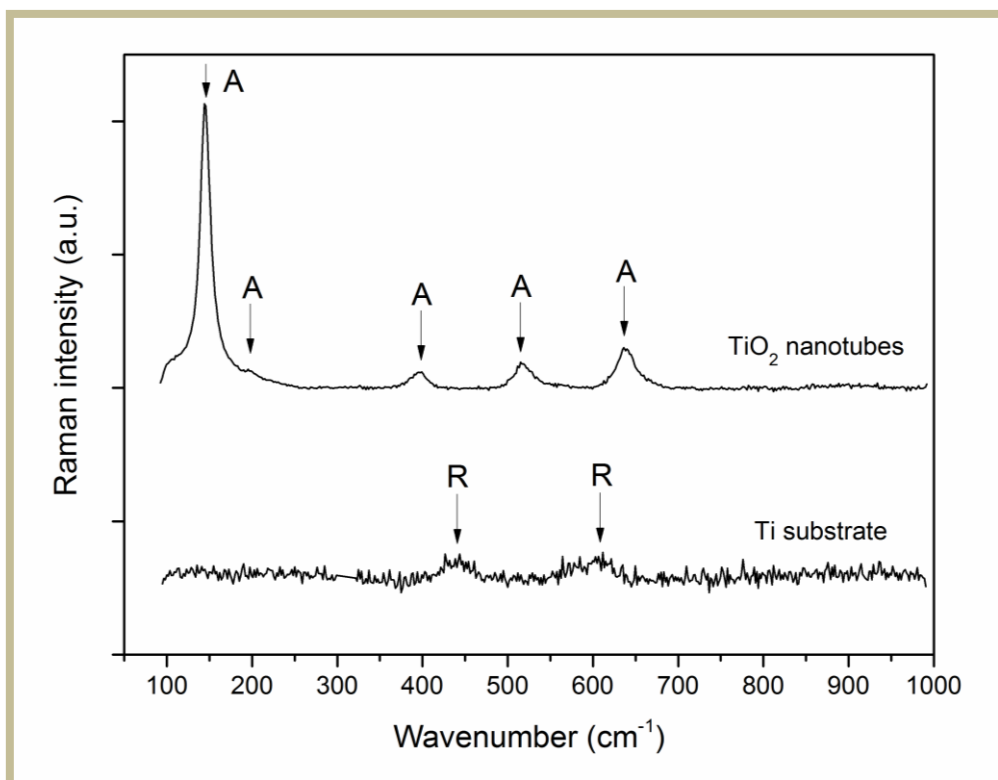


Figure 6-3. The Raman investigation reveals the anatase form of the NT films after their crystallization and the rutile traces which exist at the interface between the substrate and the tubes' bottom.

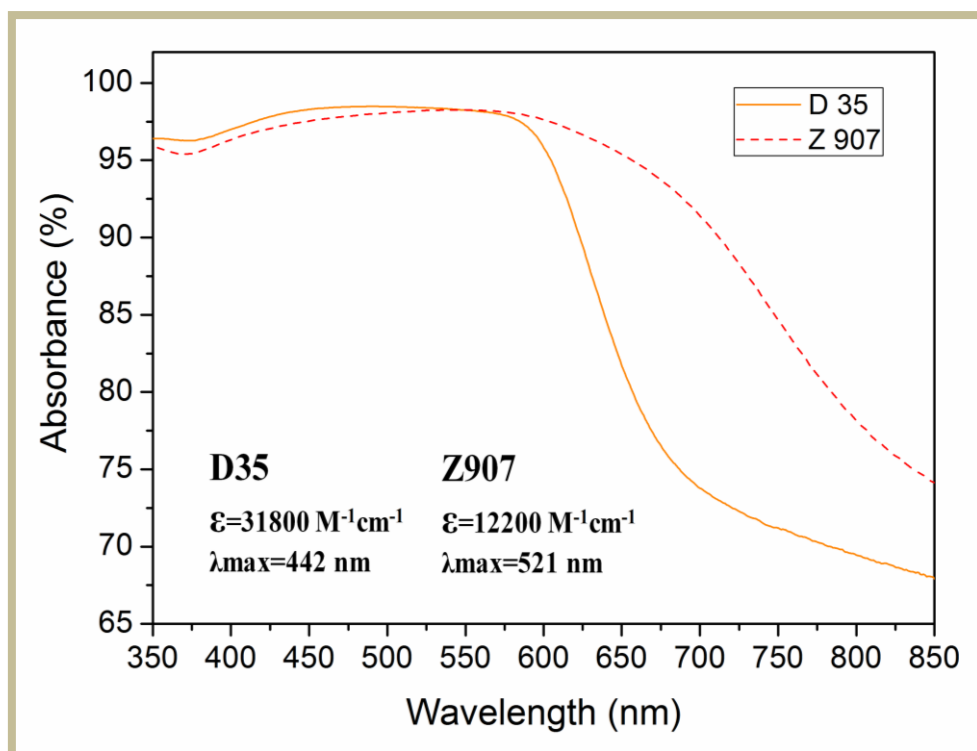


Figure 6-4. Absorbance spectra of the sensitized TNTs photoelectrodes with the Z907 (dash line) and the D35 (solid line) dyes. Absorption coefficients at maximum wavelength λ_{max} of the dyes are also given.

6.3.2. J-V characterization of NT-based DSCs under 1 sun AM1.5G illumination

Following solar cell fabrication, the J-V curves under 1 sun illumination and dark conditions were recorded, as shown in **Figure 6-5** (a) and (b), respectively. Illumination took place from the back-side (through the transparent Pt cathode) due to the use of Ti foil as back-contact; Ti foil is a flexible, rugged (non-breakable) and light-weight substrate [43,44] (also able to sustain the high temperatures needed to crystallize the tubes) with better mechanical properties than conducting glass, planned to be used in DSCs, which will serve for specific applications such as charge portable batteries carried by the army [45].

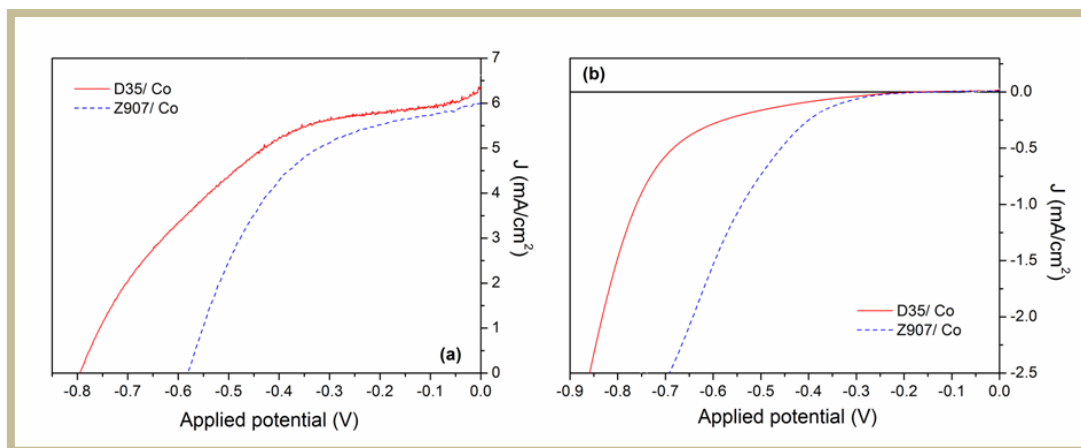


Figure 6-5. J–V characteristics of the various types of cells (a) under 1 sun illumination, (b) under dark.

Both cells delivered similar values of photocurrent (J_{sc}), approximately 6 mA cm^{-2} , despite the higher light harvesting efficiency of the Z907-TiO₂ NTs in comparison with that of the D35-TiO₂ NTs, indicating that serious issues limit J_{sc} for Z907 dye; J_{sc} limitations were recently observed for DSCs combining Z907 and the $\text{Co}(\text{bpy})^{2+/3+}$ mediator [21]. However, the most prominent feature of the photovoltaic behaviour, **Figure 6-5** (a), was the marked increase of the photovoltage by more than 0.2 V (from about 0.6 V up to more than 0.8 V) when replacing Z907 with the D35 dye. This large V_{oc} increase could be attributed to both TiO₂ conduction band-edge shift and reduction of the recombination rate due to the steric bulk properties of D35 [3,46]. These issues were subsequently explored using Electrochemical Impedance Spectroscopy (EIS) and will be discussed in the following paragraphs. Moreover, in excellent accordance with the observed differences of the V_{oc} values, the dark current (**Figure 6-5** (b)) shifted toward more negative potentials by about 0.2 V for the D35/Co system in comparison with the Z907/Co cell.

Overall, the conversion efficiency of the D35/Co cell reached 2.3%, appreciably higher than that of the Z907/Co cell (1.8%). Quite notably, much lower efficiencies (0.5%) were produced by the N719/Co system, [31]) despite the improved regeneration kinetics in comparison with Z907 dye (**Table 6-1**) [47], implying that cobalt-based

electrolytes are not compatible with the N719, in accordance with [21]. The efficiency of the D35/Co cell is relatively high, if we take into account that the electrolyte is based on a solvent with relatively high viscosity (MPN) when compared with acetonitrile, which is a typical solvent for high efficiency DSCs [20]. Additionally, the relatively low magnitude of J_{sc} is caused by the restricted absorption of D35 at high wavelengths (above 650 nm, **Figure 6-3**). Finally, the V_{oc} , even if it is as high as 0.81 V, it is still lower than that attained by front-side illuminated DSCs based on nanoparticulate titania films (0.9 V) [40]; such a V_{oc} increase was also confirmed by us in D35/Co cells using 10 μm nanoparticulate titania films (data not shown). However, the main limitation of the DSCs is the rather low fill factor (FF), being under 0.5 which can be attributed to the thick barrier layer between the nanotubes and the Ti foil [48], impeding electron collection at the back-contact.

Comparative measurements were also performed on the corresponding DSCs employing the conventional I^-/I_3^- redox mediator, **Table 6-1**. Low FF was also observed in the above DSCs **Figure 6-6**, indicating that this detrimental effect is directly related to the interfacial properties of the nanotube/substrate contact, regardless of the electrolyte used. The D35/I cell produced an identical efficiency to that gained by D35/Co. On the other hand, the Z907/I and N719/I cells provided power conversion efficiencies of c.a. 3.6 %, which compare well with those of front-illuminated DSCs, if one takes into account that illumination through the Pt cathode substantially moderates light absorption by the dye [49].

Table 6-1. Electrical parameters of nanotubular photoelectrodes which are sensitized by D35, Z907 and N719 dyes, comprising cobalt-based and iodine-based electrolytes.

Illumination					
Intensity (Sun)	DSCs	J_{sc} (mA/cm ²)	V_{oc} (V)	FF	η (%)
1	D 35/ I	6.1 ± 0.6	0.68 ± 0.04	0.55 ± 0.01	2.3 ± 0.3
0.5	D 35/ I	3.1 ± 0.4	0.64 ± 0.04	0.54 ± 0.05	2.1 ± 0.4
0.23	D 35/ I	1.5 ± 0.2	0.60 ± 0.04	0.51 ± 0.04	2.0 ± 0.3
0.1	D 35/ I	0.7 ± 0.1	0.52 ± 0.05	0.47 ± 0.06	1.7 ± 0.3
1	Z 907/ I	11.1 ± 1.6	0.70 ± 0.04	0.47 ± 0.06	3.6 ± 0.5
0.5	Z 907/ I	5.6 ± 0.8	0.67 ± 0.02	0.50 ± 0.02	3.9 ± 0.3
0.23	Z 907/ I	2.8 ± 0.4	0.64 ± 0.02	0.51 ± 0.02	4.0 ± 0.4
0.1	Z 907/ I	1.3 ± 0.2	0.58 ± 0.03	0.47 ± 0.02	3.6 ± 0.5
1	N719/ I	11.1	0.69	0.49	3.7
1	N719/ Co	2.2	0.45	0.52	0.5

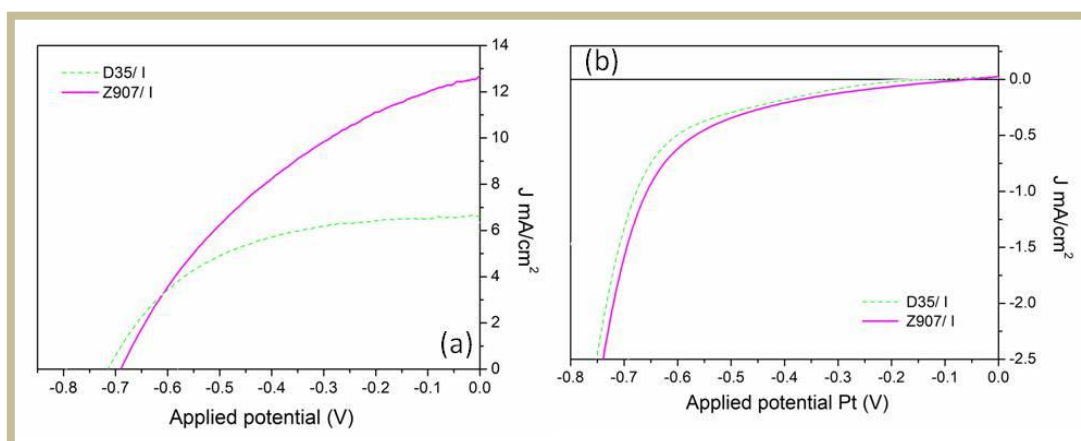


Figure 6-6. J-V characteristics (a) under 1 sun and (b) dark, of the nanotubular D35/ I and Z907/ I DSCs.

6.3.3. Photovoltaic performance of NT-based DSCs under different levels of light illumination

To better understand the photovoltaic behaviour of the D35/Co and Z907/Co DSCs, J-V curves were also recorded under different levels of illumination and the results are summarized in **Table 6-2**; accordingly, the J_{sc} was plotted against the incident light power density (P_{in}) in **Figure 6-7**. Clearly, linearity was not preserved for both cells, indicative of photocurrent limitations under conditions of strong light illumination. On the contrary, a perfect linearity was observed for the D35/I and Z907/I cells in **Figure 6-8**, due to the high diffusion coefficient of triiodide, which effectively diminishes charge transfer limitations [50]. Comparison between the D35/Co and Z907/Co cells show that charge transfer limitations were significantly reduced for the former DSCs (the actual deviations of J_{sc} vs. P_{in} from linearity occur only at maximum light power density of 1 sun for the D35/Co cells), implying that the combination of D35 with the nanotubular porous photoelectrodes provide a favorable substrate for the efficient operation of the Co^{2+}/Co^{3+} redox mediator [29]. On the contrary the Z907/Co cells, despite their higher light harvesting efficiency, could not produce high J_{sc} probably due to considerably higher impediments in charge transfer above 0.5 sun. In the linear regime, under low light illumination conditions, the D35/Co cells accordingly afforded a record efficiency of 2.7%, while the Z907/Co cells attained a maximum efficiency of 2.2% under the same conditions.

Table 6-2. Electrical parameters derived from J-V curves on DSCs, under different levels of light illumination.

Illumination					
Intensity (Sun)	DSCs	J_{sc} (mA/cm ²)	V_{oc} (V)	FF	η (%)
1	D 35/ Co	6.1 ± 0.2	0.81 ± 0.02	0.45 ± 0.03	2.3 ± 0.1
0.5	D 35/ Co	3.5 ± 0.1	0.74 ± 0.02	0.48 ± 0.01	2.5 ± 0.1
0.23	D 35/ Co	1.8 ± 0.1	0.69 ± 0.03	0.49 ± 0.01	2.7 ± 0.1
0.1	D 35/ Co	0.8 ± 0.1	0.62 ± 0.03	0.49 ± 0.02	2.6 ± 0.1
1	Z 907/ Co	6.0 ± 0.5	0.61 ± 0.05	0.49 ± 0.01	1.8 ± 0.0
0.5	Z 907/ Co	3.5 ± 0.3	0.53 ± 0.02	0.55 ± 0.04	2.1 ± 0.1
0.23	Z 907/ Co	1.7 ± 0.3	0.49 ± 0.07	0.58 ± 0.02	2.2 ± 0.1
0.1	Z 907/ Co	0.9 ± 0.1	0.45 ± 0.01	0.58 ± 0.01	2.3 ± 0.2

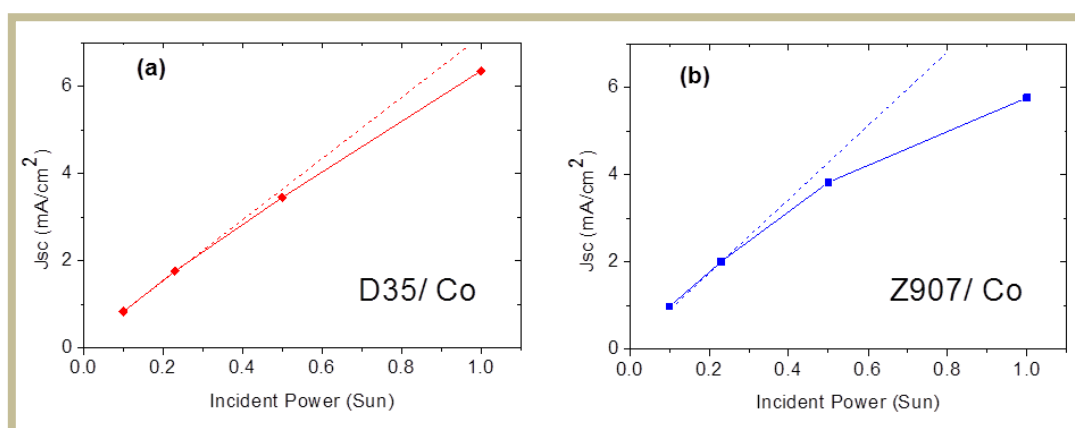


Figure 6-7. Photocurrent as a function of the incident light power density, for the different DSCs. The dotted lines, representing the ideal linear behaviour, only serve as a guide to the eye.

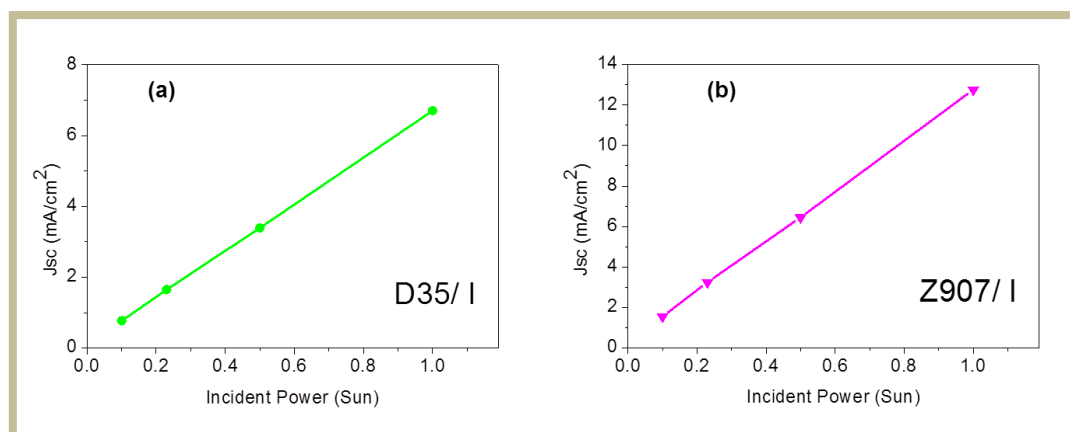


Figure 6-8. Photocurrent as a function of the incident power, for the D35/I and Z907/I cells, a perfect linearity was observed.

Photocurrent limitations could be due to slow regeneration kinetics, fast recombination kinetics and/or mass transport (diffusion) problems [51,52]. Diffusion limitations cannot be a major factor, since the D35/Co cells presented similar behavior under very strong light illumination conditions. Regeneration problems could not also justify the J_{sc} decrease at 1 sun, as previous studies have shown that the dye regeneration efficiency by 0.2 M $[\text{Co}(\text{bpy})_3]^{2+}$ is very similar (95% at short-circuit) for both D35 and Z907 [46]. Fast recombination could be accordingly inferred as the main factor underlying the observed J_{sc} limitations, in agreement with very recently published studies where distinct differences of the recombination mechanisms were identified for Co-based solar cells between a pure organic dye (Y123, being a triphenylamine dye with very similar structure to D35) and the Z907 ruthenium complex [53].

6.3.4. Non-linear recombination in NT-based DSCs

Different recombination dynamics may also (at least partially) underlie the observed differences in V_{oc} . To further explore this aspect, we plotted V_{oc} against the light power density for the D35/Co and Z907/Co cells **Figure 6-9**. A linear dependence of V_{oc} with the logarithm of light intensity was observed [54]. According to theory

[55], a slope equal to $2.303nKT/q$, where kT/q is the thermal voltage of ~ 26 mV (q is the electric charge, k is the Boltzmann's constant and T is the absolute temperature) and n is the ideality diode factor, is predicted with n values between 1 and 2 [56]. The ideality factors derived in the present cells were unexpectedly high, reaching 3.27 and 2.71 for the D35/Co and Z907/Co cells, respectively (similar n values were determined when plotting V_{oc} vs. the photocurrent). On the other hand, the Z907/I cells gave an n value of 2 (**Figure 6-10**), in excellent agreement with the values previously estimated for standard iodine-based DSCs using the Z907 dye with TiO_2 NT photoelectrodes [57]; however D35/I cells presented values of n as high as 2.71. In fact, n values in DSCs usually deviate from ideality and this was frequently attributed to non-linear recombination through surface states [58,59]. These results indicate that different recombination mechanisms dictate the V_{oc} variation whenever a different (organic or ruthenium-based) dye and/or different (cobalt or iodine-based) electrolyte is used.

Severe recombination through the exposed back-contact [60] can be excluded, since the V_{oc} response was linear for both the Z907/Co and D35/Co cells [61]. On the contrary, Z907/I and D35/I cells seem to suffer from recombination through uncovered Ti regions, since the V_{oc} does not scale linearly with the log of P_{in} (**Figure 6-10**). This would further indicate that the barrier layer formed between the tubes and the back-contact is effective for recombination suppression only in the case of the cobalt-based electrolytes (probably due to diffusion restrictions of the cobalt electrolyte).

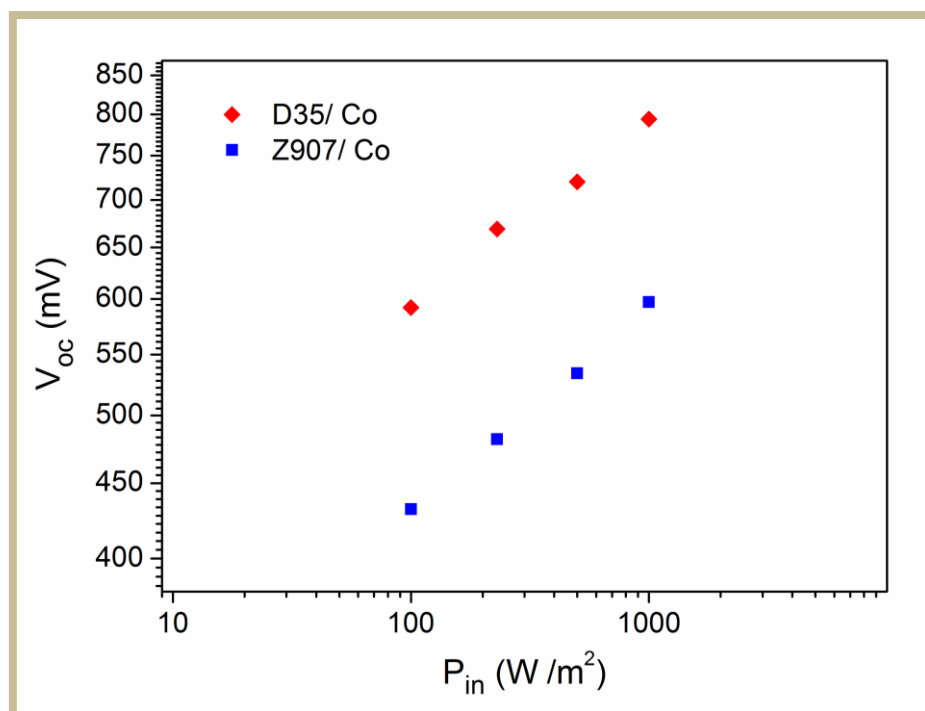


Figure 6-9. Log-log plot of photovoltage against the incident light power density, for the D35/Co and Z907/Co solar cells.

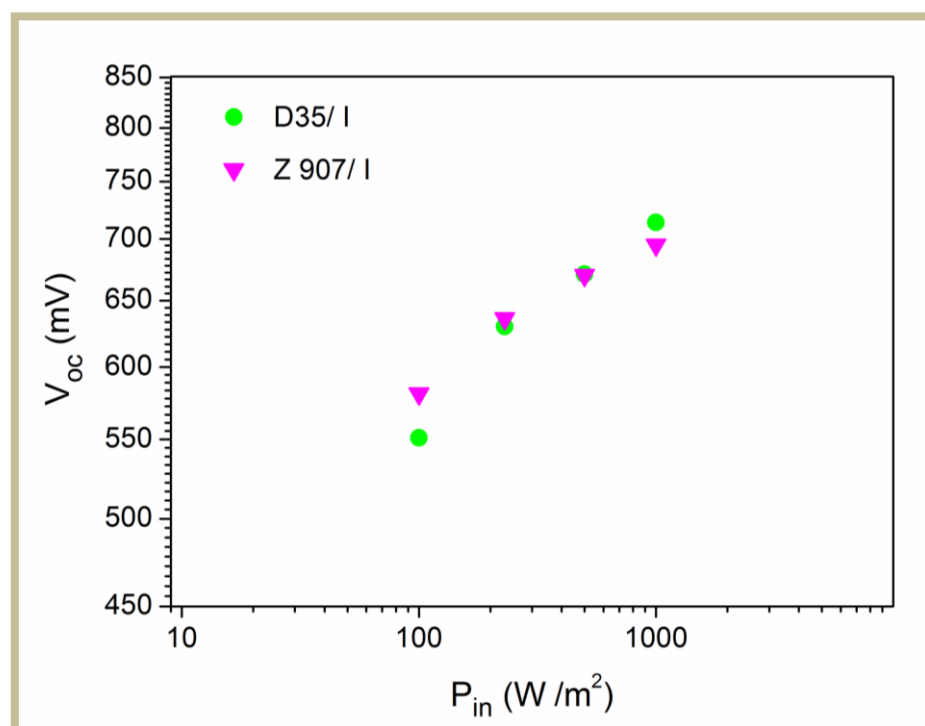


Figure 6-10. Log-log plot of photovoltage against the incident power density, for the D35/I and Z907/I solar cells.

To further investigate this effect, we re-plotted the dark current vs voltage, using the actual voltage drop at the photoelectrode

(denoted as V_F) after correcting the applied voltage for the series resistance (**Figure 6-11**) determined by EIS measurements (see the following paragraph). The resulting I - V_F curves could be well fitted to the non-ideal diode equation: $I_{\text{dark}} = I_0 \cdot \exp[(qV_F/nKT) - 1]$, where I_0 is the dark saturation current, yielding identical (to previous ones) values of n (3.3 and 2.7 for D35/Co and Z907/Co, respectively) using quite similar values of I_0 (for both cells) [62] This further confirmed that non-linear recombination is responsible for the observed non-ideality. Since recombination seems to be the major parameter for this behavior, the recombination order (b) [63] could be obtained as the inverse of n . Thus, b values of 0.31 and 0.37 were estimated for the D35/Co and Z907/Co solar cells, respectively, close to the b values previously estimated by Liu et al. for the Y123/Co system [53]. The differences in the n values between the D35/Co and Z907/Co cells can be explained by different recombination mechanisms, as proposed in the following paragraph based on the EIS analysis. Furthermore, significant deviations from linearity imply that our cells are not good rectifying devices, which is the reason why they suffer from such low values of FF (FF describes the quality of the diode behaviour of the solar cell) [58].

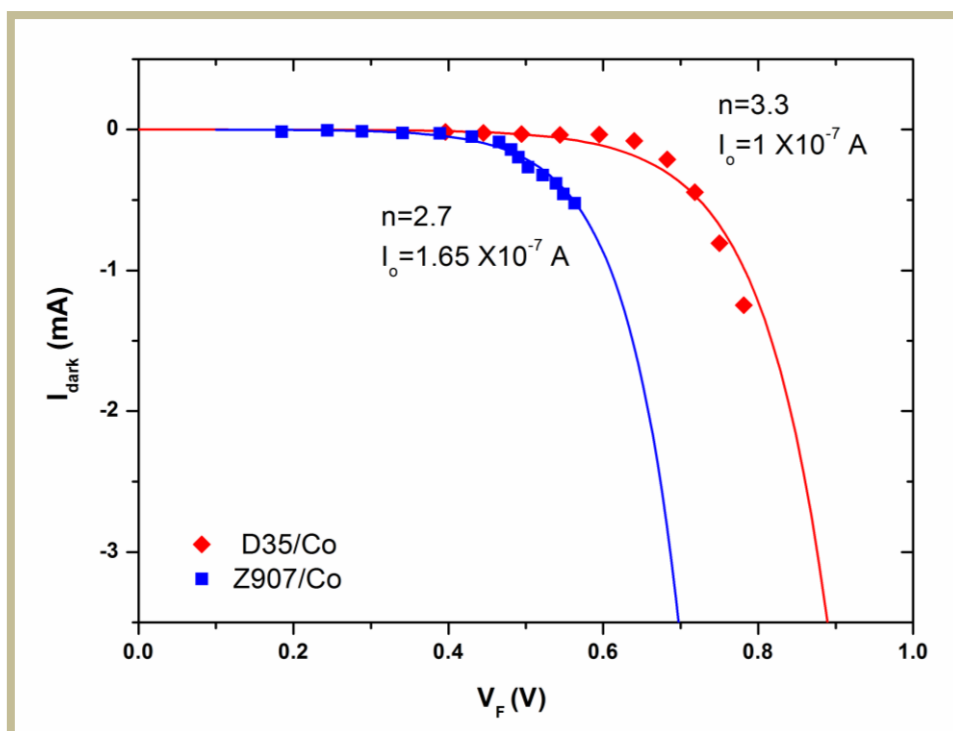


Figure 6-11. Plot of the dark current with the actual voltage drop at the photoelectrode (denoted as V_F) after the correction of the applied voltage for the series resistance. The I - V_F curves were fitted to the non-ideal diode equation, resulting in fitting parameter values of n and I_0 .

6.3.5. Electrical features of the solar cells

To further elucidate and understand the observed V_{oc} differences between the D35/Co and Z907/Co solar cells performance, EIS experiments were conducted under dark at different potentials along the I - V curve. The spectra (not shown) at potentials near V_{oc} , where TiO_2 is sufficiently conductive and transport resistance is negligible [64], typically exhibited three prominent semicircles, characteristic of DSCs employing the I^-/I_3^- redox couple [65]. The equivalent circuit used to fit the spectra was a simplified form of the transmission line model introduced by the group of Juan Bisquert [66] and previously used by our group to fit the EIS spectra of D35/Co -based cells [26].

Taking a first look at the Ohmic or pseudo-Ohmic resistances of the cells, we derived similar values for both the series resistance and the resistance at the Pt/electrolyte interface (17-22 and 11-16 Ohm,

respectively) for both D35/Co and Z907/Co DSCs as expected by the use of identical photoelectrodes, cathodes and electrolytes) [67]. This is in qualitative agreement with the similar FF values (0.45-0.49 at 1 sun) further corroborating that the low FFs result from the presence of severe non-linear recombination and not from electron transfer limitations at the interfaces.

Then, we determined the values for the charge recombination resistance (R_{rec}) as well as the respective capacitance at the TiO_2 /electrolyte interface, which is primarily determined by the chemical (or differential) capacitance (C_μ) standing for the variation of the electron density as a function of the Fermi level [68]. A comparative plot of the measured capacitances against the actual voltage drop at the photoelectrode (denoted as V_F) is shown in **Figure 6-12** (a) for the D35/Co and Z907/Co cells. The chemical capacitance followed an exponential behaviour (at least at the limited range of potentials studied in this work), confirming the exponential trap energy distribution below the TiO_2 conduction band edge according to

$$C_\mu = C_0 \exp\left[\frac{qV_F}{kT_0}\right], \text{ where } T_0 \text{ stands for a parameter with temperature}$$

units determining the depth of the trap distribution tail under the conduction band. The parameter C_0 is given by

$$C_0 = \frac{(1-p)Lq^2N_L}{kT_0} \exp\left[\frac{q(E_{F0}-E_c)}{kT_0}\right], \text{ where } p \text{ and } L \text{ are the porosity and}$$

thickness of the TiO_2 film, respectively, N_L stands for the total electron trap density and $E_{F0}-E_c$ is the difference between the dark Fermi level and the TiO_2 conduction band edge energy [69]. A clear shift could be thus identified between the D35/Co and Z907/Co cells at the same capacitance values, which can be attributed to a shift of the TiO_2 conduction band edge, considering that both cells have identical trap density and distribution (since they use the same TiO_2 working electrode-verified by the similar slopes of the exponential curves) [70]. An upward shift of 106 mV of E_c was thus determined for the D35/Co cell when compared with the Z907/Co system, whose origin can be

associated with the outward orientation of the D35 dipole moment with respect to the TiO_2 surface [71]. We should note here that this upward shift does not reduce the effective driving force for electron injection, since D35 has already a significantly high position of the excited state (the energy of the D35 dye's excited state lies at about -1.4 V vs. NHE [37] while common ruthenium dyes have an equivalent potential less than -1.0 V vs NHE [72]).

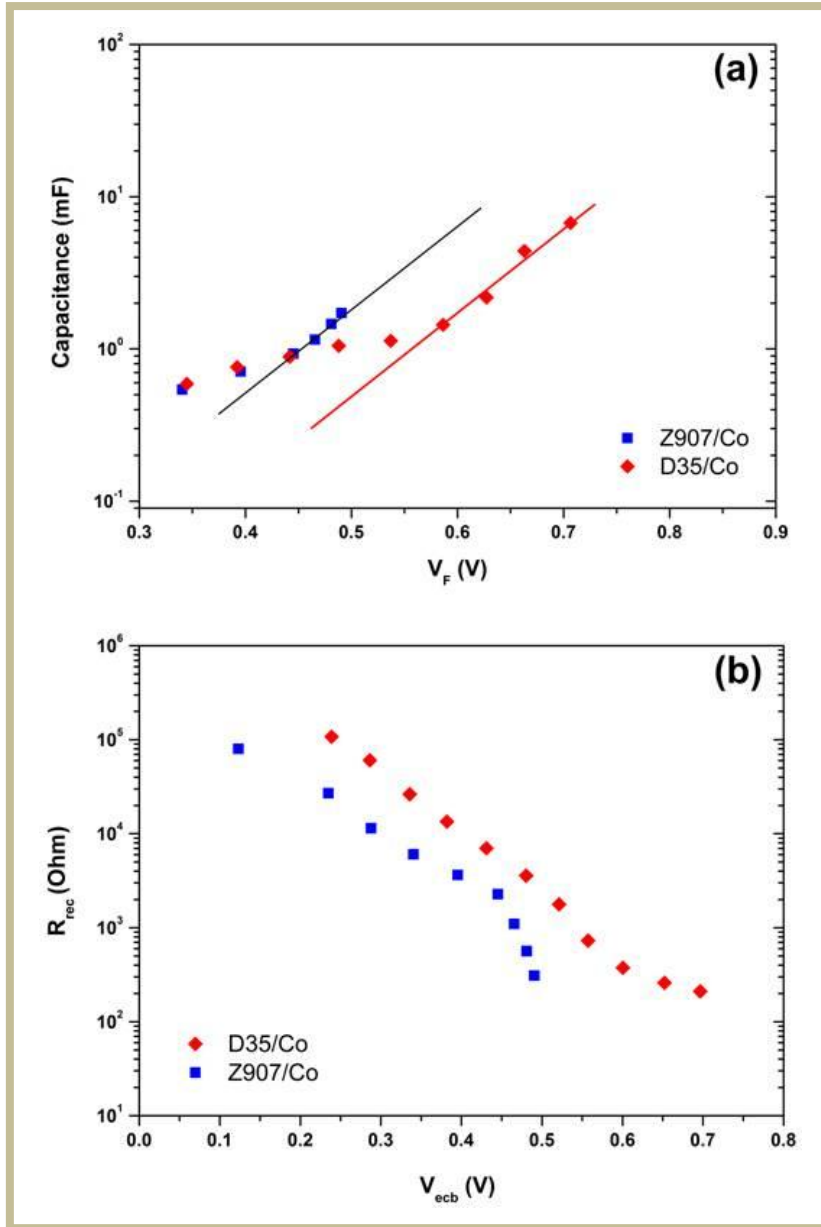


Figure 6-12. (a) Capacitance at the TiO_2 /electrolyte interface plotted against the actual potential of the photoelectrode V_F (b) Recombination resistance (R_{rec}) plotted against the voltage at the equivalent band position V_{ecb} . Results refer to D35/Co and Z907/Co solar cells- see the text inside for details.

In order to further explore the non-linear dynamics of the Co-based cells, R_{rec} was plotted against V_F (**Figure 6-13**) according to

$$R_{rec} = R_0 \exp\left[\frac{bqV_F}{kT_0}\right], \text{ where } b \text{ is the recombination order (previously}$$

estimated as the inverse of the ideality factor) and R_0 is the pre-exponential factor [68]. The obtained curves could not be fitted with a single exponential function, since regions with different recombination

dynamics were identified. Nevertheless, both curves could be adequately fitted to an exponential function near V_{oc} , when constant values of b were used (previously estimated by **Figure 6-9**); this provided further evidence that non-linearity is due to the non-linear recombination process through extended surface states in the energy distribution tail below the conduction band [68]. However, the question why the two systems (D35/Co and Z907/Co) present different values of b and R_0 remains. Taking into consideration the model recently developed by the group of Qing Wang to account for the differences in recombination dynamics between Y123/Co and Z907/Co systems [53] as well as the thorough work by Juan Anta and co-workers about non-linear recombination in DSCs [73], we could argue that recombination through relatively shallow states takes place in the case of the D35/Co system, while recombination through deeper bandgap states (far below the quasi-Fermi level) is realized in the case of the Z907/Co cell, which augments recombination. Liu et al. reported that the difference in the recombination mechanism between the organic Y123 and the ruthenium-based Z907 dye, can be related to the different ability of the two dyes to attenuate electronic coupling between $Co[(bpy)_3]^{3+}$ and TiO_2 states by the variation of their steric properties. Similar phenomena could take place in the present case, since D35 and Y123 are structurally similar triphenylamine-based organic molecules.

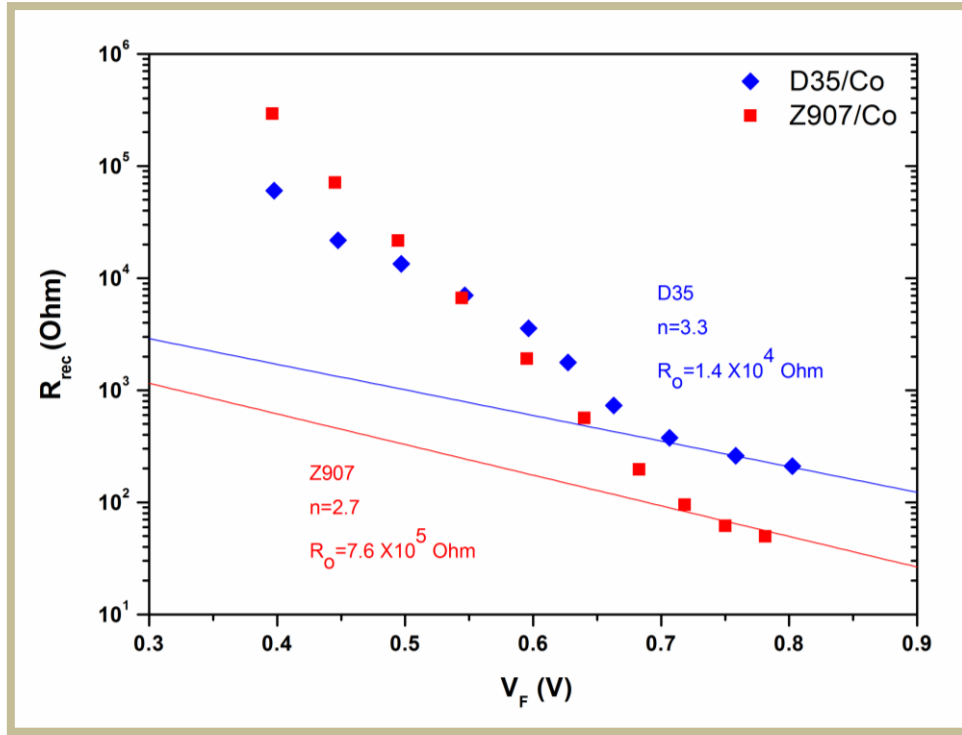


Figure 6-13. Plot of R_{rec} against V_F (voltage drop in the photoelectrode); The R_{rec} - V_F curves were fitted (close to open-circuit) to a single exponential function

$$(R_{rec} = R_0 \exp \left[\frac{bqV_F}{kT_0} \right]), \text{ determining } n \text{ and } R_0 \text{ as fitting parameters.}$$

In order to explore the actual recombination dynamics of the cells independently of the conduction band edge position, we plotted R_{rec} against V_{ecb} , which is the common equivalent conduction band potential [69], as shown in **Figure 6-12** (b). A marked suppression of recombination could be thus observed when employing the D35 dye instead of the Z907 ruthenium-based complex, providing direct evidence for the blocking character of the D35 dye. In that case, the bulky ligands in the dyes' molecular structure induce a perfect insulating monolayer on top of the TiO_2 surface thus impeding back-reactions. This was further corroborated by the variation of the electron lifetimes for the different DSCs measured under illumination by IMVS spectroscopy (**Figure 6-14**).

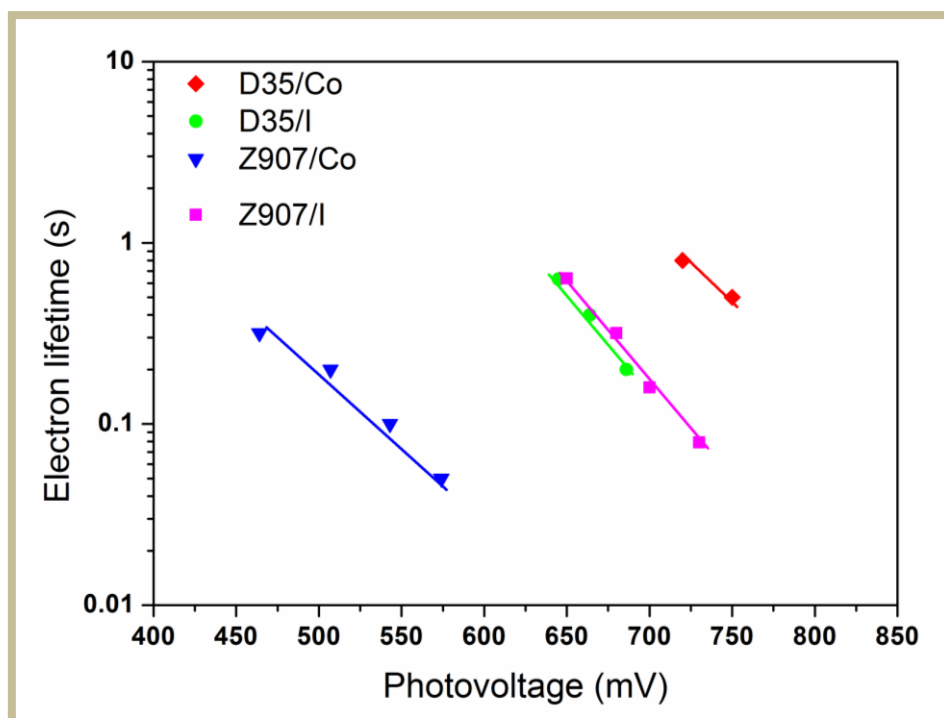


Figure 6-14. Electron lifetimes at different photovoltages (the plot was constructed by estimating lifetimes under different levels of illumination using IMVS spectroscopy).

6.4. Conclusions

Back-side illuminated DSCs were fabricated using self-assembled titania nanotubes as photoelectrodes and the novel $\text{Co}^{2+}/\text{Co}^{3+}$ redox couple as electrolyte; a standard ruthenium complex and a pure organic dye were used as effective sensitizers. The DSCs based on the Z907 dye gave an efficiency of 1.8% under 1 sun illumination accompanied with a low V_{oc} of only 0.6V, while a higher efficiency (2.3%) was gained with the D35 dye due to the significant enhancement of the photovoltage up to more than 0.8 V. Two different effects were identified that contributed to the V_{oc} increase: firstly the conduction band-edge of TiO_2 shifted towards higher potentials due to the high dipole moment of the D35 dye and secondly the recombination was reduced due to the blocking character of the latter dye. Recombination was found to be the most crucial parameter rendering these solar cells to significantly depart from ideality (i.e. this

kind of DSC does not behave as ideal diodes) both under open and short-circuit conditions. Non-ideal recombination dynamics were different for the D35 or Z907 dyes; we argued that recombination takes place through shallow states in the case of the D35/Co system, while recombination through deeper bandgap states is realized in the case of the Z907/Co cell. Besides V_{oc} , non-linear recombination is believed to limit also the FF of these DSCs, since no restrictions for electron transfer at the interfaces (and especially at the thick rutile barrier layer between the tubes and the back-contact) were detected. Finding ways to reduce the cell non-linearity will definitely lead to significantly higher efficiencies for the near future. Nevertheless, despite the relatively low efficiencies, if we take into account that the Co^{2+}/Co^{3+} redox couple diffuses well inside the periodic porous nanotubular structure and reduces charge recombination due to the steric hindrance effect of the D35 dye, the proposed DSC structure becomes a prominent candidate for specific applications, such as indoor modules sensible to diffuse light or flexible PVs.

6.5. References

1. A. Hagfeldt, M. Gratzel, "Light-Induced Redox Reactions in Nanocrystalline Systems" *Chem. Rev.* 95 (1995) 49.
2. B. M. Kayes, H. Nie, R. Twist, S. G. Spruytte, F. Reinhardt, I. C. Kizilyalli, G. S. Higashi "27.6% conversion efficiency, a new record for single-junction solar cells under 1 sun illumination" 37th IEEE Photovoltaic Specialist Conference, Seattle, June 2011.
3. A. Hagfeldt, G. Boschloo, L. Sun, L. Kloo, H. Pettersson "Dye-Sensitized Solar Cells" *Chem. Rev.* 10 (2010) 6595.
4. B. O'Regan, M. Grätzel "A low-cost, high-efficiency solar cell based on dye-sensitized colloidal TiO_2 films" *Nature* 353 (1991) 737.
5. C. Y. Chen, M. Wang, J. Y. Li, N. Pootrakulcote, L. Alibabaei, C. Ngoc-le, J. D. Decoppet, J. H. Tsai, J. H.; C. Grätzel, C. G. Wu, S. M.

- Zakeeruddin, M. Grätzel "Highly Efficient Light-Harvesting Ruthenium Sensitizer for Thin-Film Dye-Sensitized Solar Cells" *ACS Nano* 3 (2009) 3103.
6. S. Nakade, T. Kanzaki, W. Kubo, T. Kitamura, Y Wada, S. Yanagida, "Role of electrolytes on charge recombination in dye-sensitized TiO₂ solar cell (1): the case of solar cells using the I⁻/I₃⁻ redox couple" *J. Phys. Chem. B* 109 (2005) 3480.
 7. G. Boschloo, A. Hagfeldt "Characteristics of the Iodide/Triiodide Redox Mediator in Dye-Sensitized Solar Cells" *Acc. Chem. Res.* 42 (2009) 1819.
 8. S. Cazzani, S. Caramori, R. Argazzi, M. C. Elliott, C. A. Bignozzi "Efficient Non-corrosive Electron-Transfer Mediator Mixtures for Dye-Sensitized Solar Cells" *J. Am. Chem. Soc.* 128 (2006) 9996.
 9. Y. Bai, Q. Yu, N. Cai, Y. Wang, M. Zhang, P. Wang "High-efficiency organic dye-sensitized mesoscopic solar cells with a copper redox shuttle" *Chem. Commun.* 47 (2011) 4376.
 10. T. Daeneke, T. H. Kwon, A. B. Homes, N. W. Uffey, U. Bach, L. Spiccia "High-efficiency dye-sensitized solar cells with ferrocene-based electrolytes" *Nat. Chem.* 3 (2011) 213.
 11. K. Kakiage, T. Tokutome, S. Iwamoto, T. Kyomen, M. Hanaya "Fabrication of a dye-sensitized solar cell containing a Mg-doped TiO₂ electrode and a Br₃⁻/Br⁻ redox mediator with a high open-circuit photovoltage of 1.21 V" *Chem. Commun.* 49 (2013) 179.
 12. T. Stergiopoulos, P. Falaras "Minimizing Energy Losses in Dye-Sensitized Solar Cells Using Coordination Compounds as Alternative Redox Mediators Coupled with Appropriate Organic Dyes" *Adv. Energy Mater.* 2 (2012) 616.
 13. M. J. DeVries, M. J. Pellin, J. T. Hupp "Dye-Sensitized Solar Cells: Driving-Force Effects on Electron Recombination Dynamics with Cobalt-Based Shuttles" *Langmuir* 26 (2010) 9082.
 14. A. Yella, H. W. Lee, H. N. Tsao, C. Yi, A. K. Chandiran, M. K. Nazeeruddin, E. W. G. Diau, C. Y. Yeh, S. M. Zakeeruddin M. Grätzel

“Porphyrin-Sensitized Solar Cells with Cobalt (II/III)–Based Redox Electrolyte Exceed 12 Percent Efficiency” *Science* 334 (2011) 629.

15. M. S. Feldt, W. P. Lohse, F. Kessler, K. M. Nazeeruddin, M. Gratzel, G. Boschloo, A. Hagfeldt “Regeneration and recombination kinetics in cobalt polypyridine based dye-sensitized solar cells, explained using Marcus theory” *Phys. Chem. Chem. Phys.* 15 (2013) 7087.

16. H. Wang, G. P. Nicholson, L. Peter, M. S. Zakeeruddin, M. Gratzel “Transport and Interfacial Transfer of Electrons in Dye-Sensitized Solar Cells Utilizing a Co(dbbp)₂ Redox Shuttle” *J. Phys. Chem. C* 114 (2010) 14300.

17. L. E. Polander, A. Yella, B. F. E. Curchod, N. A. Astani, J. Teuscher, R. Scopelliti, P. Gao, S. Mathew, J. E. Moser, I. Tavarnelli, U. Rothlisberger, M. Gratzel, M. K. Nazeeruddin, J. Frey “Towards Compatibility between Ruthenium Sensitizers and Cobalt Electrolytes in Dye-Sensitized Solar Cells” *Angew. Chem. Int. Ed.* 52 (2013) 8731.

18. J. L. Yum, W. T. Holcombe, Y. Kim, K. Rakstys, T. Moehl, J. Teuscher, H. J. Delcamp, K. M. Nazeeruddin, M. Gratzel “Blue-Coloured Highly Efficient Dye-Sensitized Solar Cells by Implementing the Diketopyrrolopyrrole Chromophore” *Sci. Rep.* doi:10.1038/srep02446.

19. K. Lim, J. M. Ju, J. Na, H. Choi, Y. M. Song, B. Kim, K. Song, S. J. Yu, E. Kim, J. Ko “Molecular Engineering of Organic Sensitizers with Planar Bridging Units for Efficient Dye-Sensitized Solar Cells” *Chem. Eur. J.* 19 (2013) 9442.

20. Y. Liu, R. J. Jennigs, X. Wang, Q. Wang “Significant performance improvement in dye-sensitized solar cells employing cobalt(III/II) tris-bipyridyl redox mediators by co-grafting alkyl phosphonic acids with a ruthenium sensitizer” *Phys. Chem. Chem. Phys.* 15 (2013) 6170.

21. P. Salvatori, G. Marotta, A. Cinti, C. Anselmi, E. Mosconi, F. De Angelis “Supramolecular Interactions of Chenodeoxycholic Acid Increase the Efficiency of Dye-Sensitized Solar Cells Based on a Cobalt Electrolyte” *J. Phys. Chem. C* 117 (2013) 3874.

22. M. T. Koh, K. Nonomura, N. Mathews, A. Hagfeldt, M. Grätzel, G. S. Mhaisalkar, C. A. Grimsdale "Influence of 4-tert-Butylpyridine in DSCs with CoII/III Redox Mediator" *J. Phys. Chem. C* 117 (2013) 15515.
23. M. Zhang, J. Zhang, Y. Fan, L. Yang, Y. Wang, R. Li, P. Wang "Judicious selection of a pinhole defect filler to generally enhance the performance of organic dye-sensitized solar cells" *Energy Environ. Sci.* 6 (2013) 2939.
24. K. Miettunen, T. Saukkonen, X. Li, H. C. Law, K. Y. Sheng, J. Halme, A. Tiihonen, R. F. P. Barnes, T. Ghaddar, I. Asgar, P. Lund, B. O'Regan "Do Counter Electrodes on Metal Substrates Work with Cobalt Complex Based Electrolyte in Dye Sensitized Solar Cells?" *J. Electrochem. Soc.* 160 (2013) H132.
25. D. L. Roy-Mayhew, G. Boscloo, A. Hagfeldt, A. Aksay, A. A. Ihan "Functionalized Graphene Sheets as a Versatile Replacement for Platinum in Dye-Sensitized Solar Cells" *Appl. Mater. Interfaces* 4 (2012) 2794.
26. T. Stergiopoulos, M. Bidikoudi, V. Likodimos, P. Falaras "Dye-sensitized solar cells incorporating novel Co(II/III) based-redox electrolytes solidified by silica nanoparticles" *J. Mater. Chem.* 22 (2012) 24430.
27. B. M. Achari, V. Elumalai, N. Vlachopoulos, M. Safdari, J. Gao, M. J. Gardner, L. Kloo "A quasi-liquid polymer-based cobalt redox mediator electrolyte for dye-sensitized solar cells" *Phys. Chem. Chem. Phys.* 15 (2013) 17419.
28. W. Xiang, W. Huang, U. Bach, L. Spiccia "Stable high efficiency dye-sensitized solar cells based on a cobalt polymer gel electrolyte" *Chem. Comm.* 49 (2013) 8997.
29. H. S. Kim, S. B. Ko, I. H. Jang, N. G. Park "Improvement of mass transport of the [Co(bpy)₃]^{II/III} redox couple by controlling nanostructure of TiO₂ films in dye-sensitized solar cells" *Chem. Commun* 47 (2011) 12637.

30. H. N.Tsao, P. Comte, S. Yi, M. Grätzel “Avoiding Diffusion Limitations in Cobalt(III/II)-Tris(2,2'-Bipyridine)-Based Dye-Sensitized Solar Cells by Tuning the Mesoporous TiO₂ Film Properties” *Chem. Phys. Chem.* 13 (2012) 2976.
31. Y. J. Kim, J. K. Lee, H. S. Kang, J. Shin, E. Y. Sung “Enhanced Photovoltaic Properties of a Cobalt Bipyridyl Redox Electrolyte in Dye-Sensitized Solar Cells Employing Vertically Aligned TiO₂ Nanotube Electrodes” *J. Phys. Chem. C* 115 (2011) 19979.
32. P. J. Gonzalez-Vazquez, V. Morales-Flórez, J. A. Anta “How Important is Working with an Ordered Electrode to Improve the Charge Collection Efficiency in Nanostructured Solar Cells?” *J. Phys. Chem. Lett.* 3 (2012) 386.
33. K. Zhu, T. B. Vinzant, N. R. Neale, A. J. Frank “Removing Structural Disorder from Oriented TiO₂ Nanotube Arrays: Reducing the Dimensionality of Transport and Recombination in Dye-Sensitized Solar Cells” *Nanolett.* 7 (2007) 3739.
34. P. Roy, D. Kim, K. Lee, E. Spieckerb, P. Schmuki “TiO₂ nanotubes and their application in dye-sensitized solar cells” *Nanoscale* 2 (2010) 45.
35. G. K. Mor, O. K. Varghese, M. Paulose, K. Shankar, C. A. Grimes “A review on highly ordered, vertically oriented TiO₂ nanotube arrays: Fabrication, material properties, and solar energy applications” *Sol. Energ. Mat. Sol. C* 90 (2006) 2011.
36. T. P. Hsiao, J. Y. Liou, H. Teng “Electron Transport Patterns in TiO₂ Nanotube Arrays Based Dye-Sensitized Solar Cells under Frontside and Backside Illuminations” *J. Phys. Chem. C* 115 (2011) 15018.
37. D. P. Hagberg, X. Jiang, E. Gabrielsson, M. Linder, T. Marinado, T. Brinck, A. Hagfeldt, L. Sun “Symmetric and unsymmetric donor functionalization. comparing structural and spectral benefits of chromophores for dye-sensitized solar cells” *J. Mater. Chem.* 19 (2009) 7232.

38. K. C. D. Robson, K. Hu, J. G. Meyer, P. C. Berlinguette "Atomic Level Resolution of Dye Regeneration in the Dye-Sensitized Solar Cell" *J. Am. Chem. Soc.* 135 (2013) 1961.
39. N. Vaenas, T. Stergiopoulos, A. G. Kontos, V. Likodimos, N. Boukos, P. Falaras "Sensitizer activated solar cells based on self-organized TiO₂ nanotubes" *Microelectronic Eng.* 90 (2012) 62.
40. S. M. Feldt, E. A. Gibson, E. Gabrielsson, L. Sun, G. Boschloo, A. Hagfeldt "Design of Organic Dyes and Cobalt Polypyridine Redox Mediators for High-Efficiency Dye-Sensitized Solar Cells" *J. Am. Chem. Soc.* 132 (2010) 16714.
41. M. J. Macak, H. Hildebrand, U. Marten-Jahns, P. Schmuki "Mechanistic aspects and growth of large diameter self-organized TiO₂ nanotubes" *J Electroanal. Chem.* 621 (2008) 254.
42. J. Wang, Z. Lin "Dye-Sensitized TiO₂ Nanotube Solar Cells with Markedly Enhanced Performance via Rational Surface Engineering" *Chem. Mater.* 22 (2010) 579.
43. S. Ito, N. L. C. Ha, G. Rothenberg, P. Liska, P. Comte, M. Zakeeruddin, P. Pechy, M. Khaja, K. Nazueruddin, M. Gratzel "High-efficiency (7.2%) flexible dye-sensitized solar cells with Ti-metal substrate for nanocrystalline-TiO₂ photoanode" *Chem. Commun.* (2006) 4004.
44. J. An, W. Guo, T. Ma "Enhanced Photoconversion Efficiency of All-Flexible Dye-Sensitized Solar Cells Based on a Ti Substrate with TiO₂ Nanoforest Underlayer" *Small* 8 (2012) 3427.
45. H. Desilvestro, "Dye solar cells-Towards commercialization" 4th International Conference on the Industrialisation of DSC DSC-IC 10 01-04 November 2010 Colorado Springs, CO, USA.
46. S. M. Feldt, G. Wang, G. Boschloo, A. Hagfeldt "Effects of Driving Forces for Recombination and Regeneration on the Photovoltaic Performance of Dye-Sensitized Solar Cells using Cobalt Polypyridine Redox Couples" *J. Phys. Chem. C* 115 (2011) 21500.
47. E. Mosconi, J. H. Yum, F. Kessler, C. J. Gómez García, C. Zuccaccia, A. Cinti, M. K. Nazeeruddin, M. Grätzel, F. De Angelis

- “Cobalt Electrolyte/Dye Interactions in Dye-Sensitized Solar Cells: A Combined Computational and Experimental Study” *J. Am. Chem. Soc.* 134 (2012) 19438.
48. S. H. Kang, J. Y. Kim, Y. Kim, H. S. Kim, Y. E. Sung “Surface Modification of Stretched TiO₂ Nanotubes for Solid-State Dye-Sensitized Solar Cells” *J. Phys. Chem. C* 111 (2007) 9614.
49. Y. J. Kim, J. H. Noh, K. Zhu, A. F. Halverson, N. R. Neale, S. Park, K. S. Hong, J. Frank “General Strategy for Fabricating Transparent TiO₂ Nanotube Arrays for Dye-Sensitized Photoelectrodes: Illumination Geometry and Transport Properties” *ACS Nano* 5 (2011) 2647.
50. Z. Yu, M. Gorlov, J. Nissfolk, G. Boschloo, L. Kloo “Investigation of Iodine Concentration Effects in Electrolytes for Dye-Sensitized Solar Cells” *J. Phys. Chem. C* 114 (2010) 10612.
51. A. Y. Anderson, P. R. F. Barnes, J. R. Durrant, B. O'Rega “Quantifying Regeneration in Dye-Sensitized Solar Cells” *J. Phys. Chem. C* 115 (2011) 2439.
52. H. Paulsson, L. Kloo, A. Hagfeldt, G. Boschloo “Electron transport and recombination in dye-sensitized solar cells with ionic liquid electrolytes” *J. Electroanal. Chem.* 586 (2006) 56.
53. Y. Liu, J. R. Jennings, S. M. Zakeeruddin, M. Grätzel, Q. Wang “Heterogeneous Electron Transfer from Dye-sensitized Nanocrystalline TiO₂ to [Co(bpy)₃]³⁺: Insights Gained from Impedance Spectroscopy” *J. Am. Chem. Soc.* 135 (2013) 3939.
54. J. Nelson, *The Physics of Solar Cells*, 2003 Imperial College Press, London WC2H 9HE.
55. L. J. A. Koster, V. D. Mihaileti, R. Ramaker, P. W. M. Blom “Light intensity dependence of open-circuit voltage of polymer:fullerene solar cells” *Appl. Phys. Lett.* 86 (2005) 123509.
56. Z. Sun, R. K. Zhang, H. H. Xie, H. Wang, M. Liang, S. Xue “Nonideal Charge Recombination and Conduction Band Edge Shifts in Dye-Sensitized Solar Cells Based on Adsorbent Doped Poly(ethylene oxide) Electrolytes” *J. Phys. Chem. C* 117 (2013) 4364.

57. J. R. Jennings, A. Ghicov, L. M. Peter, P. Schmuki A. B. Walker "Dye-Sensitized Solar Cells Based on Oriented TiO₂ Nanotube Arrays: Transport, Trapping, and Transfer of Electrons" *J. Am. Chem. Soc.* 130 (2008) 13364.
58. J. Bisquert I. Mora-Sero "Simulation of Steady-State Characteristics of Dye-Sensitized Solar Cells and the Interpretation of the Diffusion Length" *J. Phys. Chem. Lett.* 1 (2010) 450.
59. A. B. Walker, L. M. Peter, K. Lobato, P. J. Cameron "Analysis of Photovoltage Decay Transients in Dye-Sensitized Solar Cells" *J. Phys. Chem. B* 110 (2006) 25504.
60. J. R. Jennings, Y. Liu, Q. Wang, S. M. Zakeeruddin, M. Grätzel "The influence of dye structure on charge recombination in dye-sensitized solar cells" *Phys. Chem. Chem. Phys.* 13 (2011) 6637.
61. E. Guillén, L. M. Peter, J. A. Anta "Electron Transport and Recombination in ZnO-Based Dye-Sensitized Solar Cells" *J. Phys. Chem. C* 115 (2011) 22622.
62. D. W. Park, Y. Jeong, J. Lee, J. Lee, S. H. Moon "Interfacial Charge-Transfer Loss in Dye-Sensitized Solar Cells" *J. Phys. Chem. C* 117 (2013) 2734.
63. P R. F. Barnes, K. Miettunen, X. Li, A. Y. Anderson, T. Bessho, M. Grätzel, B. O'Regan "Interpretation of Optoelectronic Transient and Charge Extraction Measurements in Dye-Sensitized Solar Cells" *Adv. Mater.* 25 (2013) 1881.
64. F. Fabregat-Santiago, J. Bisquert, G. Garcia-Belmonte, G. Boschloo, A. Hagfeldt "Influence of electrolyte in transport and recombination in dye-sensitized solar cells studied by impedance spectroscopy" *Sol. Energy Mater. Sol. Cells* 87 (2005) 117.
65. Q. Wang, S. Ito, M. Grätzel, F. Fabregat-Santiago, I. Mora-Seró, J. Bisquert, T. Bessho, H. Imai "Characteristics of High Efficiency Dye-Sensitized Solar Cells" *J. Phys. Chem. B* 110 (2006) 25210.
66. J. Bisquert "Chemical capacitance of nanostructured semiconductors: its origin and significance for nanocomposite solar cells" *Phys. Chem. Chem. Phys.* 5 (2003) 5360.

67. Y. H. Chen, K. C. Huang, J. G. Chen, R. Vittal, K. C. Ho "Titanium flexible photoanode consisting of an array of TiO₂ nanotubes filled with a nanocomposite of TiO₂ and graphite for dye-sensitized solar cells" *Electrochim. Acta* 56 (2011) 7999.
68. S. R. Raga, F. Fabregat-Santiago "Temperature effects in dye-sensitized solar cells" *Phys. Chem. Chem. Phys.* 15 (2013) 2328.
69. F. Fabregat-Santiago, G. Garcia-Belmonte, I. Mora-Seró J. Bisquert "Characterization of nanostructured hybrid and organic solar cells by impedance spectroscopy" *Phys. Chem. Chem. Phys.* 13 (2011) 9083.
70. V. Pedro-González, X. Xu, I. Mora-Seró, J. Bisquert "Modeling High-Efficiency Quantum Dot Sensitized Solar Cells" *ACS Nano* 4 (2010) 5783.
71. P. Chen, J. H. Yum, F. De Angelis, E. Mosconi, S. Fantacci, S. J. Moon, R. H. Baker, J. Ko, M. K. Nazeeruddin, M. Grätzel "High Open-Circuit Voltage Solid-State Dye-Sensitized Solar Cells with Organic Dye" *Nano Lett.* 9 (2009) 2487.
72. S. Kim, J. K. Lee, S. O. Kang, J. Ko, J. H. Yum, S. Fantacci, F. De Angelis, D. Di Censo, M. K. Nazeeruddin, M. Grätzel "Molecular Engineering of Organic Sensitizers for Solar Cell Applications" *J. Am. Chem. Soc.* 128 (2006) 16701.
73. J. P. Gonzalez Vazquez, G. Oscan, J. A. Anta "Origin of Nonlinear Recombination in Dye-Sensitized Solar Cells: Interplay between Charge Transport and Charge Transfer" *J. Phys. Chem. C* 116 (2012) 22687.

Chapter 7. Conclusions

7.1. Evaluation and contribution

Summarizing the key findings of the present thesis, it should be noted that the initial targets for the preparation, the assessment and the energy application (DSCs) of the titania nanotubes have been accomplished. Also, some very important results have arisen through the findings of this thesis.

- The electrochemical oxidation of the titanium foil is a powerful technique that permits both, the formation and the precise control of a variety of nanotubular morphologies (appendix).
- In order to ensure the reproducibility of the samples all the experimental conditions (especially the temperature and the humidity) have to remain stable.
- The top surface of the nanotube film should be clean of debris (molten tubes) in order to facilitate the free entrance into them.
- The annealing conditions strongly influence the crystallinity of the TiO_2 nanotubes and affect the power conversion efficiency of the corresponding DSCs.
- The morphological features of the nanotubes play a crucial role in the efficiency of the pvotovoltaics.
- The titania nanotube arrays as a highly porous photoelectrode can facilitate the diffusion of the electrolytes that experience mass transport limitations due to their large molecular size (cobalt shuttles).
- The TiO_2 nanotubes can serve as an excellent alternative photoelectrode to the classic nanoparticulate one; at the same time the nanotubular photoelectrodes endow the DSCs with flexibility and sufficiently high efficiency (especially for indoor applications).

- Despite the open structure and the oriented morphology, the nanotubular DSCs haven't succeeded yet in achieving really enhanced efficiencies. The reasons for that, are based upon the inherent defects that originate from the fabrication procedure (§ 2.2.2). Annealing and other post treatments (introducing new elements or by tube-wall decoration) seems to be the best way in order to control the defects and to raise the cells' performance.

In the frame of this dissertation an appreciable contribution to the scientific knowledge has been realized, due to the innovative outcomes.

- For a first time, a two step potentiostatic - galvanostatic technique for the growth of TiO₂ NT arrays has been developed (chapter 5).
- It is the only work in the literature that examines in depth the interactions of the cobalt redox shuttle in combination with titania nanotube arrays, sensitized by the organic dye D35 (chapter 6).
- With the variety of the nanotubular morphologies that have been developed it has been proven that, the specific structure is multifunctional and multipurpose (appendix).

7.2. Perspectives for future work

The working experience and the knowledge that have been obtained from this thesis can be used in order to take a further step in the development of solar cells, with the utilization of the NTs. Some pioneer ideas are quoted below.

- Combination of annealing with other post treatments techniques with a view, to develop the electrical characteristics into the band gap of the semiconducting TiO₂ nanotubes and finally to increase the DSCs' efficiency [1,2].
- Thin nanotubular layers-membranes (500-1000 nm) can serve as an excellent scaffold, compact layer and electron conductor in the

construction of the state of the art perovskite (organic-inorganic) solar cells [3-5].

- Solid state solar cells could be fabricated with nanotubular photoelectrodes sensitized by quantum dots absorbers and employing, instead of the redox electrolytes, the inorganic hole transport perovskites [6-8].
- TNTs can serve as an excellent substrate for emerging electroapplications such as: self-driven solar water splitting [9,10], visible photocatalysis [11] and tandem cells [12].

7.3. References

1. P. Roy, D. Kim, K. Lee, E. Spiecker, P. Schmuki "TiO₂ nanotubes and their application in dye-sensitized solar cells" *Nanoscale* 2 (2010) 45.
2. P. Roy, S. Berger, P. Schmuki "TiO₂ Nanotubes: Synthesis and Applications" *Angew. Chem. Int. Ed.* 50 (2011) 2904.
3. E. Mosconi, A. Amat, M.. K. Nazeeruddin, M. Gratzel, F. De Angelis "First-Principles Modeling of Mixed Halide Organometal Perovskites for Photovoltaic Applications" *J. Phys. Chem. C* 117 (2013) 13902.
4. M. M. Lee, J. Teuscher, T. Miyasaka, T. N. Murakami, H. J. Snaith "Efficient Hybrid Solar Cells Based on Meso-Superstructured Organometal Halide Perovskites" *Science* 338 (2012) 643.
5. H-S. Kim, J-W. Lee, N. Yantara, P. P. Boix, S. A. Kulkarni, S. Mhaisalkar, M. Gratzel, N-G. Park "High Efficiency Solid-State Sensitized Solar Cell-Based on Submicrometer Rutile TiO₂ Nanorod and CH₃NH₃PbI₃ Perovskite Sensitizer" *Nano Lett.* 13 (2013) 2412.
6. Q. Shen, A. Yamada, S. Tamura, T. Toyoda "CdSe quantum dot-sensitized solar cell employing TiO₂ nanotube working-electrode and Cu₂S counter-electrode" *Appl. Phys. Lett.* 97 (2010) 123107.

7. I. Chung, B. Lee, J. He, R. P. H. Chang, M. G. Kanatzidis "All-solid-state dye-sensitized solar cells with high efficiency" *Nature* 485 (2012) 486.
8. Y. Zhou, H. F. Garces, B. S. Senturk, A. L. Ortiz, N. P. Padture "Room temperature "one-pot" solution synthesis of nanoscale CsSnI₃ orthorhombic perovskite thin films and particles" *Mater. Lett.* 110 (2013) 127.
9. Z. Zhang, P. Wang, "Boosting TiO₂ nanotube array based photocatalysis efficiency for energy conversion" Spring 2013 New Orleans ACS National Meeting 245 (2013) Meeting Abstract: 275-ENVR.
10. C.W. Lai, S. Sreekantan "Study of WO₃ incorporated C-TiO₂ nanotubes for efficient visible light driven water splitting performance" *J. Alloy. Compd.* 547 (2013) 43.
11. P. Xiang, F. Jijiang, Z. Xuming, L. Yong, H. Meng, H. Kaifu, C. K. Paul "Carbon-Doped TiO₂ Nanotube Array Platform for Visible Photocatalysis" *Nanosci. Nanotechnol. Lett.* 5 (2013) 1251.
12. W. Guo, X. Xue, S. Wang, C. Lin, Z. L. Wang "An Integrated Power Pack of Dye-Sensitized Solar Cell and Li Battery Based on Double-Sided TiO₂ Nanotube Arrays" *Nano Lett.* 12 (2012) 2520.

Appendix. Electrochemical nano-engineering

Morphology manipulation

Electrochemistry has been proven to be one of the most powerful tools in the hands of the experimental researchers. Also, if the investigators respect the method's basics principles, in order to ensure reproducibility, they are able to benefit of its advantages and to create extraordinary structures.

In this chapter, all the impressive nanotubular morphologies that have been manufactured by the titanium anodic oxidation, during the implementation of the present thesis are quoted.

The **Figure A-1** shows nanotubes with different pore diameters and wall thicknesses. The determinative factors that govern the nanotubes' diameter are the applied potential (or current density) and the water content (**Table 2-1**) [1,2]. The specific samples have been prepared in Ethylene glycol based electrolytes with the same amount of NH_4F (0.3 % wt) as follows: 2 % vol H_2O and 0.75 mA/cm² applied current density (a), 1 % vol H_2O and 30 V applied potential (b), 10 % vol H_2O and 60 V applied potential (c).

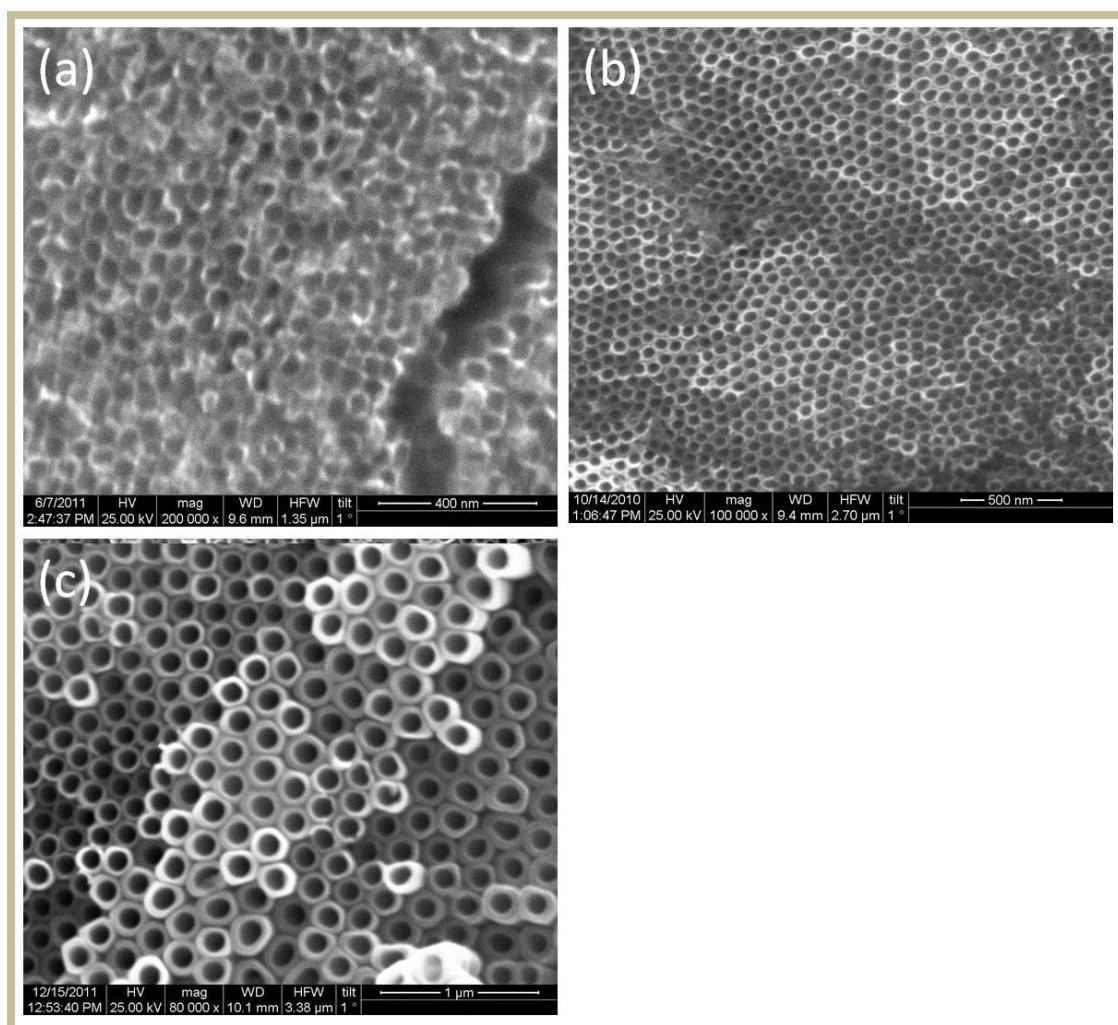


Figure A-1. NTs with different internal diameters (D_{in}) and wall thickness (W): $D_{in}=30$ nm, $W=10$ nm (a), $D_{in}=60$ nm, $W=25$ nm (b), $D_{in}=120$ nm, $W=50$ nm (c).

A further morphological manipulation of the top surface can take place, depending on the electrolyte composition and the pre-treatment of the titanium foil. In **Figure A-2** (a), the NTs are presenting a disoriented and clogged top surface, as a result of the increased dissolution rate (**Table 2-1**) in the Formamide based electrolyte [3]. On the other hand in **Figure A-2** (b), an oriented and clean film of well separated nanotubes has been developed by configuration of low growth rate, with an Ethylene glycol based electrolyte containing increased water content (10 % vol) [4]. The pretreatment of the Ti foils with a first anodization and detachment of the nanotube films (with ultrasonication **Figure A-7**) ensures both,

the growth of the new nanotubes in predefined spots and their good orientation, **Figure A-2** (c) [5].

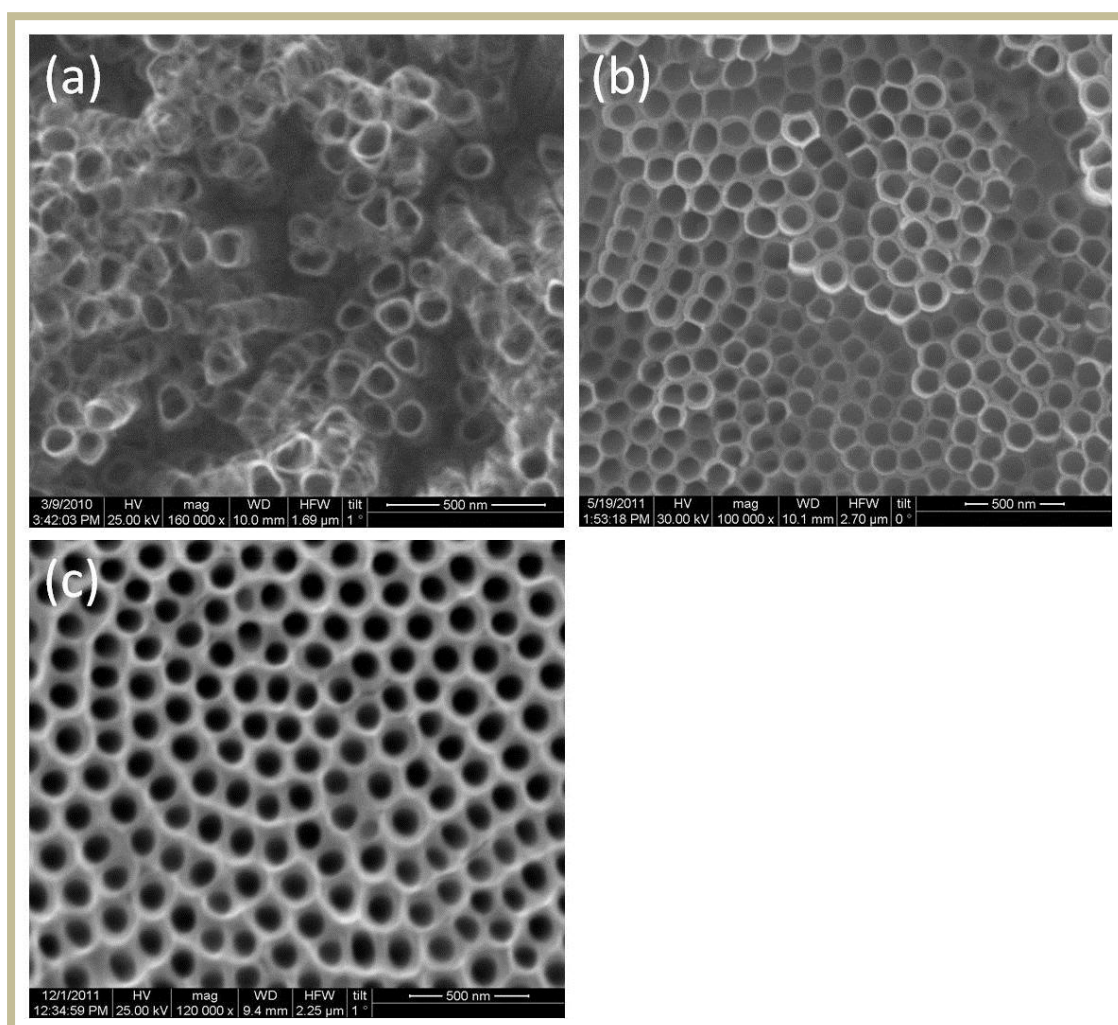


Figure A-2. NTs with a variety of top surface morphologies: semi-clean and disoriented (a), clean, oriented and with separated walls (b), stuck and developed on predefined spots (c).

The “fractal like” top surface morphologies of the **Figure A-3** (a-c), can play the role of photonic crystals in environmental applications [6]. Their surface configuration is the outcome of a two-step anodization, in the first step the pattern (large concaves) was prepared by anodizing in elevated voltage of 60 V (and subsequent detachment of the nanotube films **Figure A-7**), in the second step lower potentials or currents were applied and depending on them, a specific number of internal pores (into the concaves) were evolved.

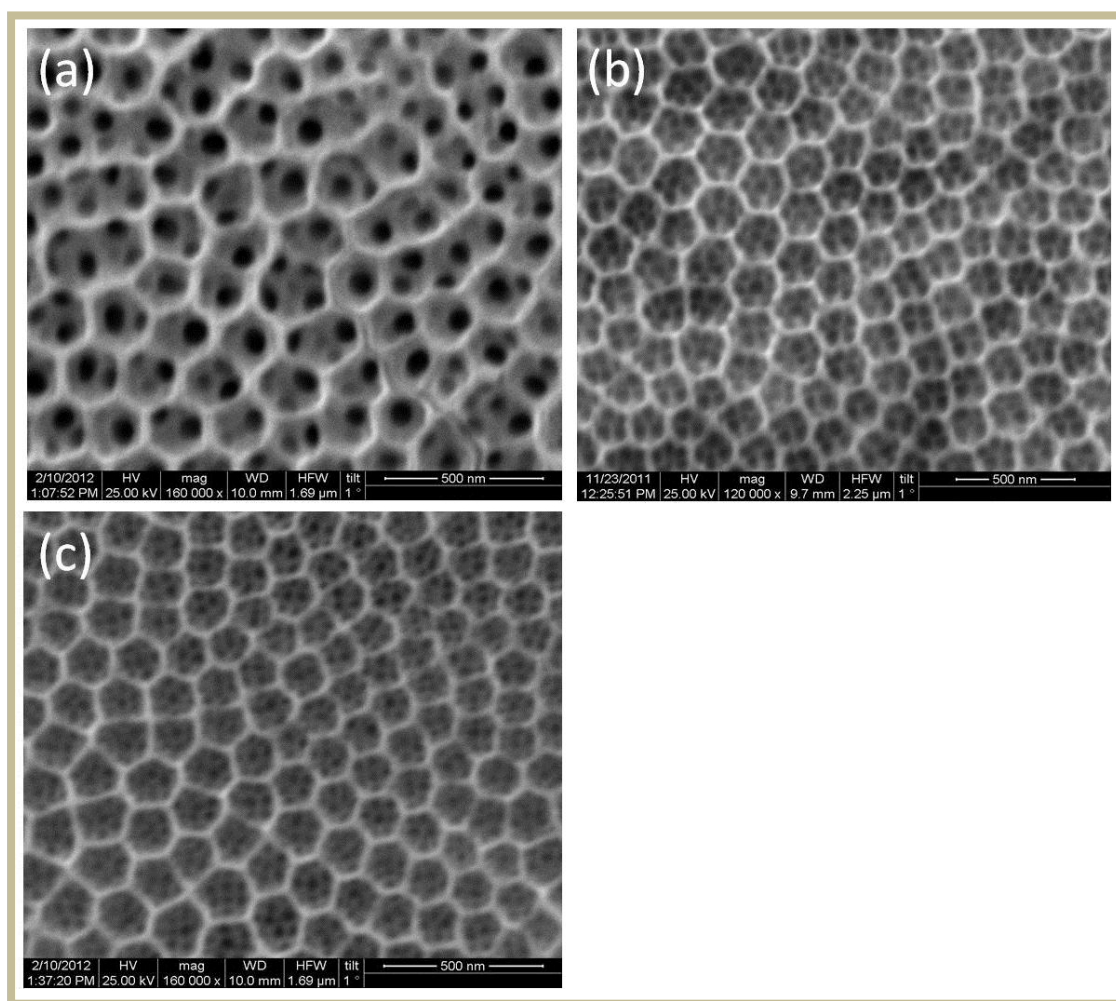


Figure A-3. Complex surface morphologies that have been formed onto a patterned Ti foil. The concave parts have internal diameter from 100 to 160 nm and the internal pores can be varied from 15 to 50 nm. 1-3 pores inside the concave parts (a), 4-7 pores inside the concave parts (b), 7> pores inside the concave part (2 μ m length, the nanotubular film is transparent) (c).

The length of the NTs is a function of the electrolyte's composition and the duration of the anodization (**Table 2-1**). With the appropriate handling of both parameters, NTs from some hundreds of nm to some tens of μ m are feasible to be produced **Figure A-4** [7,8].

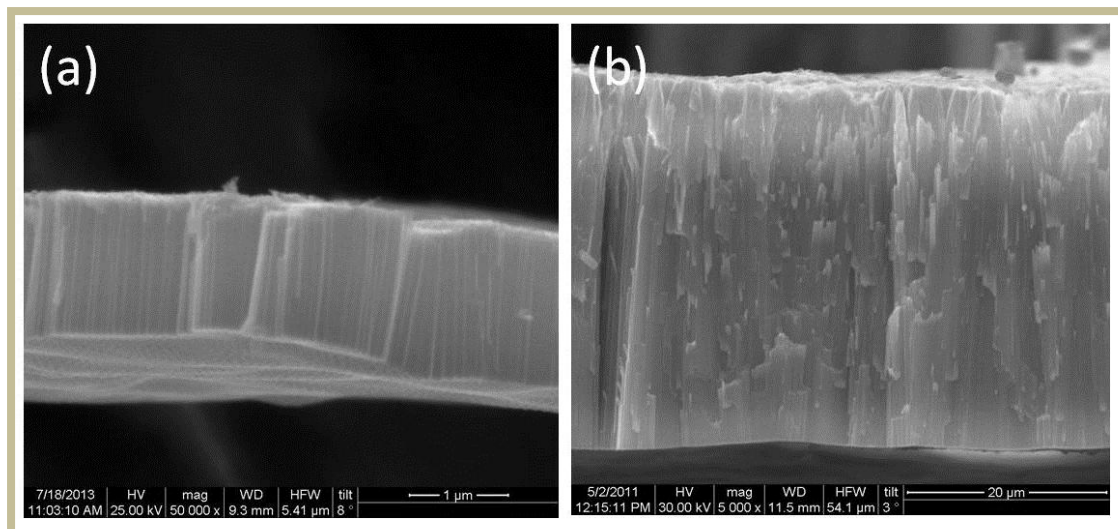


Figure A-4. Nanotubular films in a variety of lengths: total thickness 1200 nm (a), total thickness ~40 μm (b).

Another way to design innovative nanotubes is the wall decoration by ribs, **Figure A-5**. This can happen depending, once more, on the electrolyte composition. Smooth walls come from electrolytes poor in water (1 % vol) **Figure A-5** (a). On the contrary the distribution of random ribs comes off from electrolytes rich in water (10 % vol) **Figure A-5** (b). The synthesis of periodically structured titania nanotubes **Figure A-5** (c), can be achieved by altering voltage conditions (periodic voltage-pulse sequences) [9] and allows the precise control of the distance between the ribs. In this way the NTs are transformed into photonic crystals [10].

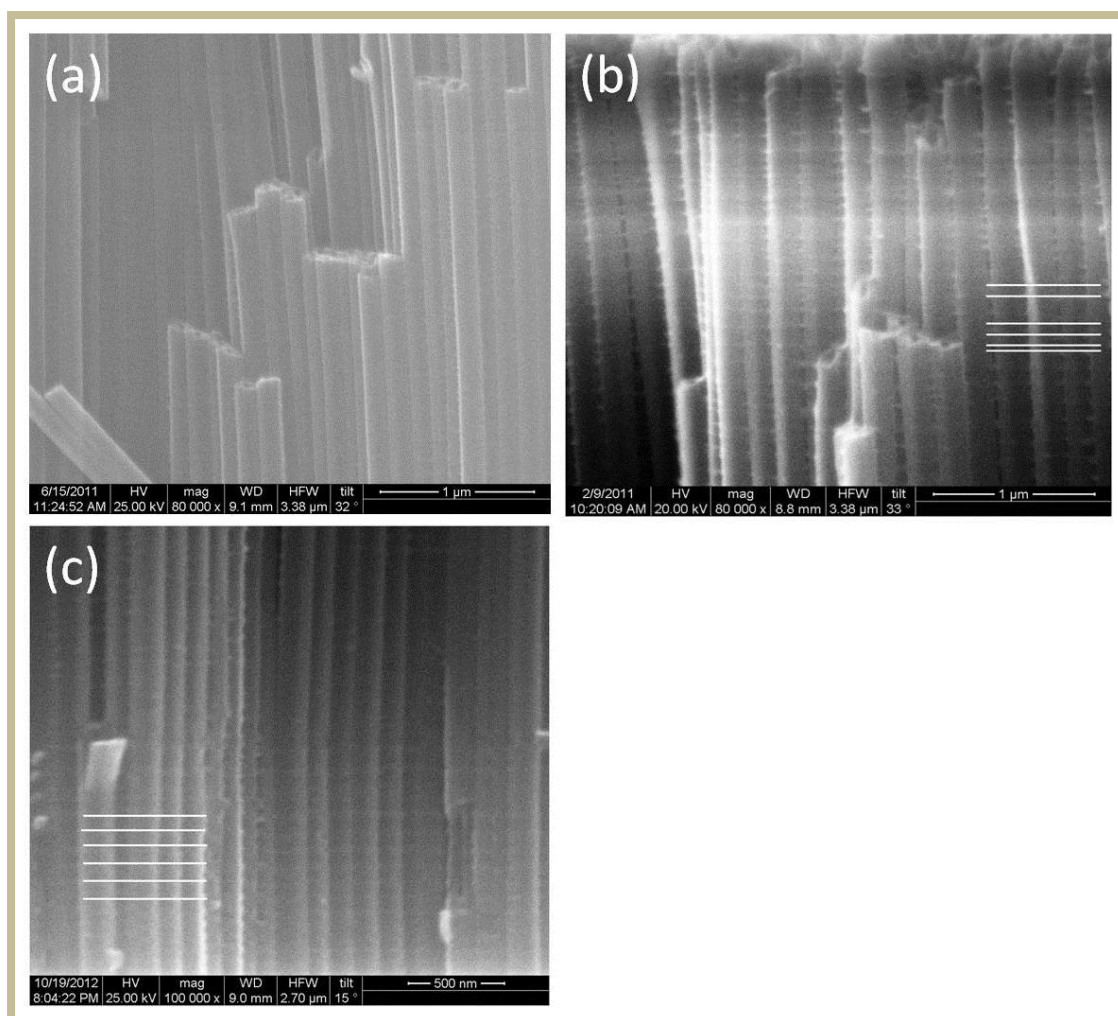


Figure A-5. NTs with walls decorated by ribs: smooth walls without ribs (a), random ribs distribution (white lines) (b), controlled ribs distribution at distances of 100 nm (white lines) (c).

The best example of the NTs' adaptability is being presented in **Figure A-6**. NTs can be tailored during the anodization in order to form either multi-layered films **Figure A-6** (a,b), or branched NTs **Figure A-6** (c,d) [11,12]. The key point is that the procedure can be controlled by the choice of the current density: if the current drops to zero, (e.g. by an abrupt lowering of the potential), then a multi-layered nanotubular film is formed; but if the current gradually decreases to a smaller value without zeroing, (e.g. by a reducing voltage ramp), then branched NTs are formed.

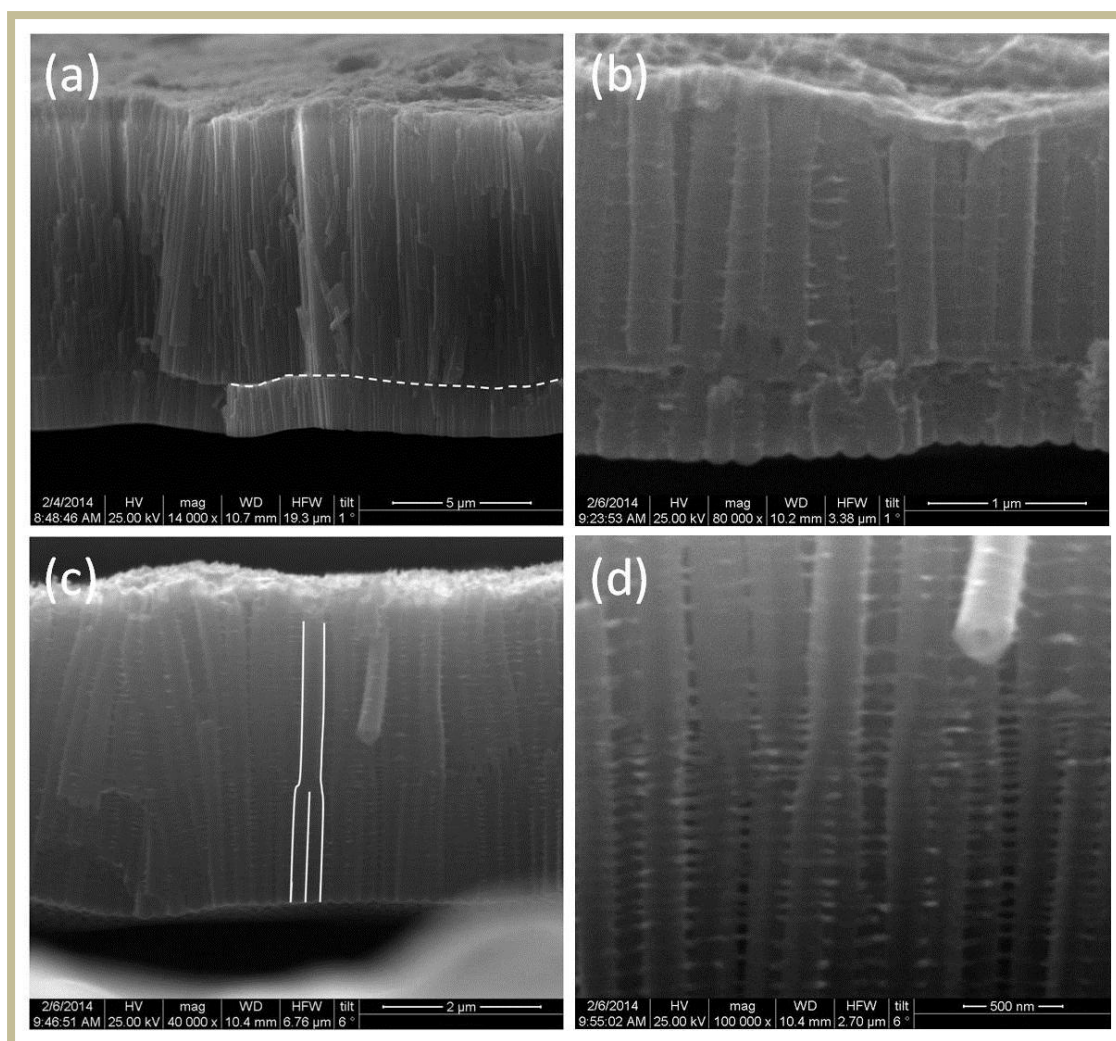


Figure A-6. Double layer tubes, each layer has different morphological characteristics (a, b). Branched nanotubes, from the initial NT two new NTs can be formed (c, d).

Nanotubular membranes (detached from the Ti foil) comprise one more options that anodic oxidation of Ti offers, in the frame of materials growth, **Figures A-8** and **A-7**. Membranes up to 0.1 mm are easily prepared by extended oxidation in electrolytes with a low dissolution rate [13,14].

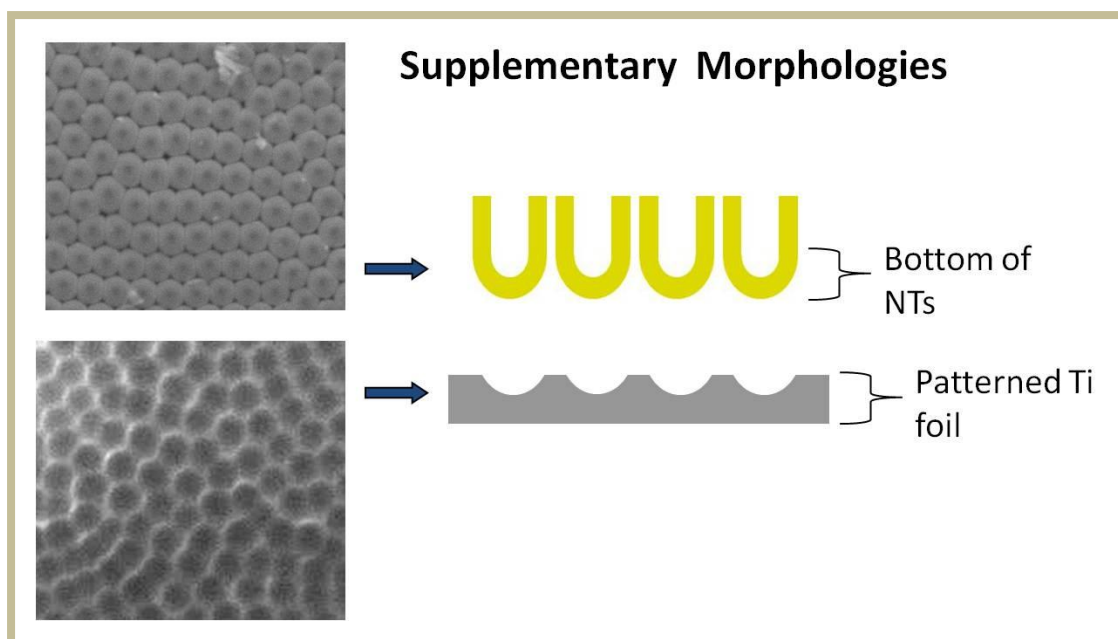


Figure A-7. Close bottom TiO_2 nanotubes, as detached from the titanium foil (with ultrasonic treatment) and forming supplementary morphologies.

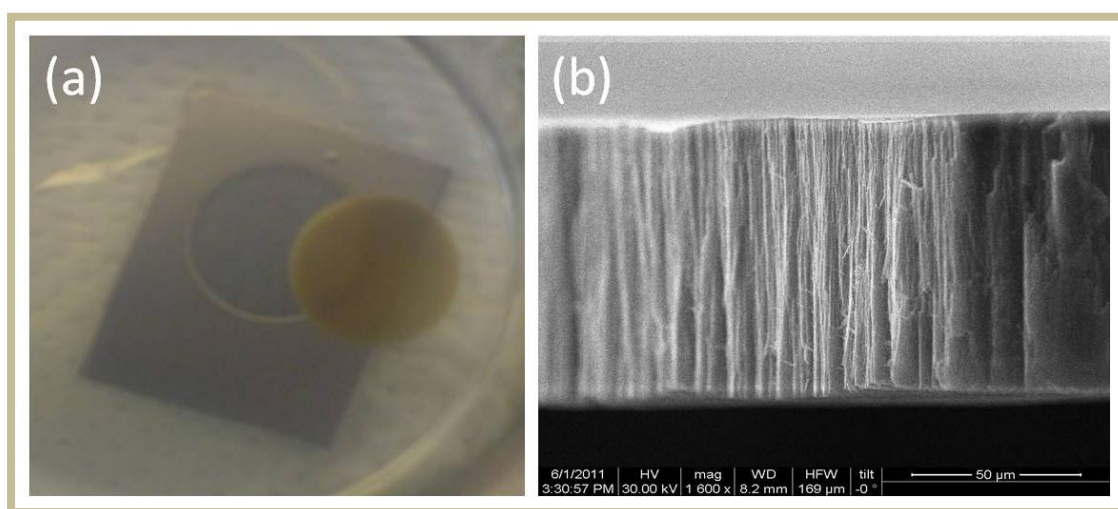


Figure A-8. Pure TiO_2 membranes up to (or $>$) 0.1 mm can possibly develop: photograph of the membrane (a) and the corresponding SEM image (b).

Last but not least, colorful barrier-type titania films can be formed onto the surface of the Ti substrate by anodization in sulfuric acid electrolytes. The impressive colors are a result of the interference of the reflected light on both the metallic substrate and the oxide layer. The thickness of the oxide layer is of the order of the visible light's wavelengths [15].

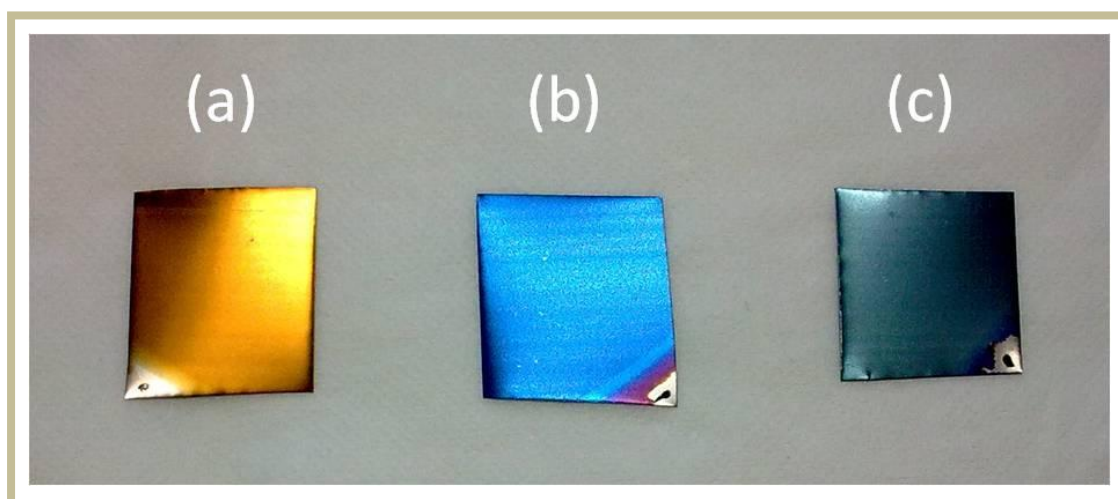


Figure A-9. Impressive colorful oxide coatings, that have been formed by anodization of titanium in sulfuric acid electrolytes (for 1 min): potential 10 V, thickness of the coating 25 nm, color gold (a); potential 20 V, thickness of the coating 50 nm, color turquoise blue (b); potential 30 V, thickness of the coating 100 nm, color raf-blue (c).

References

1. Z. Su, W. Zhou "Pore diameter control in anodic titanium and aluminium oxides" *J. Mater. Chem.* 21 (2011) 357.
2. H. Yin, H. Liu, W. Z. Shen "The large diameter and fast growth of self-organized TiO₂ nanotube arrays achieved via electrochemical anodization" *Nanotechnology* 21 (2010) 035601.
3. K. Shankar, G. K. Mor, A. Fitzgerald, C. A. Grimes "Cation Effect on the Electrochemical Formation of Very High Aspect Ratio TiO₂ Nanotube Arrays in Formamide-Water Mixtures" *J. Phys. Chem. C* 111 (2007) 21.
4. Z.B. Xie, D.J. Blackwood "Effects of anodization parameters on the formation of titania nanotubes in ethylene glycol" *Electrochimica Acta* 56 (2010) 905.
5. S. Li, G. Zhang, D. Guo, L. Yu, W. Zhang "Anodization Fabrication of Highly Ordered TiO₂ Nanotubes" *J. Phys. Chem. C* 113 (2009) 12759.

6. Z. Zhang, L. Zhang, M. N. Hedhili, H. Zhang, P. Wang "Plasmonic Gold Nanocrystals Coupled with Photonic Crystal Seamlessly on TiO₂ Nanotube Photoelectrodes for Efficient Visible Light Photoelectrochemical Water Splitting" *Nano Lett.* 13 (2013) 14.
7. P. Zhong, W. Que, Y. Liao, J. Zhang, X. Huc "Improved performance in dye-sensitized solar cells by rationally tailoring anodic TiO₂ nanotube length" *J. Alloys Compd.* 540 (2012) 159.
8. Y. Liu, B. Zhou, J. Li, X. Gan, J. Bai, W. Cai "Preparation of short, robust and highly ordered TiO₂ nanotube arrays and their applications as electrode" *Appl. Catal. B- Environ.* 92 (2009) 326.
9. C. T. Yip, H. Huang, L. Zhou, K. Xie, Y. Wang, T. Feng, J. Li, W. Y. Tam Direct and Seamless Coupling of TiO₂ Nanotube Photonic Crystal to Dye-Sensitized Solar Cell: A Single-Step Approach *Adv. Mater.* 23 (2011) 5624.
10. M. Guo, K. Xie, J. Lin, Z. Yong, C. T. Yip, L. Zhou, Y. Wang, H. Huang "Design and coupling of multifunctional TiO₂ nanotube photonic crystal to nanocrystalline titania layer as semi-transparent photoanode for dye sensitized solar cell" *Energy Environ. Sci.* 5 (2012) 9881.
11. Y-Y. Song, F. Schmidt-Stein, S. Bauer, P. Schmuki "Amphiphilic TiO₂ Nanotube Arrays: An Actively Controllable Drug Delivery System" *J. Am. Chem. Soc.* 131 (2009) 4230.
12. B. Chen. K. Lu "Hierarchically Branched Titania Nanotubes with Tailored Diameters and Branch Numbers" *Langmuir* 28 (2012) 2937.
13. M. Paulosea, L. Pengc, K. C. Popatb, O. K. Varghese, T. J. LaTempaa, N. Baoa, T. A. Desai, C. A. Grimes "Fabrication of mechanically robust, large area, polycrystalline nanotubular/porous TiO₂ membranes" *J. Membrane Sci.* 319 (2008) 199.
14. K-l. Li, Z-B. Xie, S. Adams "A reliable TiO₂ nanotube membrane transfer method and its application in photovoltaic devices" *Electrochim. Acta* 62 (2012) 116.
15. S. V. Gilsa, P. Masta, E. Stijnsb, H. Terryna "Colour properties of barrier anodic oxide films on aluminium and titanium studied with

total reflectance and spectroscopic ellipsometry” *Surf. Coat. Tech.* 185 (2004) 303.

Sketch

